Journal of *Marine Science and Engineering*

MDPI

Article

Prediction-Driven Assessment of Multi-Ship Traffic Pressure and Maritime Traffic Situation

Ruizhi Zhang, Qiang Li * and Binjie Zhou

Navigation College, Dalian Maritime University, Dalian 116026, China; runti61@163.com (R.Z.); zbj32900@dlmu.edu.cn (B.Z.)

* Correspondence: manumail@dlmu.edu.cn

Abstract

In increasingly complex navigation environments, maritime traffic supervision needs to look beyond the instantaneous collision risk of individual-ship pairs. A multi-ship scene may become difficult to monitor because of vessel aggregation, spatial compression, encounter urgency, and inconsistent motion states. To support proactive Vessel Traffic Services (VTS), this study proposes a prediction-driven framework for assessing multi-ship traffic pressure by combining AIS-based short-term motion prediction with a Spatio-Temporal Encounter Traffic Pressure Index (ST-TPI). In the proposed framework, cleaned and resampled AIS trajectories are used to train an LSTM model for short-term vessel motion prediction. The predicted vessel states are then synchronized into future multi-ship traffic snapshots over a 30 min horizon, and ST-TPI is used to evaluate traffic pressure at the ship-pair, individual-ship, regional, and scene levels. Different from conventional collision-risk or traffic-complexity methods, the proposed framework focuses on how future traffic pressure forms, changes, and is transferred among vessels and vessel pairs. The method was tested using five typical multi-ship scenarios and a real-waterway case in the western precautionary area of the Laotieshan Channel. The prediction results showed stable short-term forecasting performance with low meter-level position errors under the observation-updated rolling evaluation, providing a basis for future multi-ship snapshot generation. The typical scenarios revealed different pressure-evolution patterns, including low-pressure persistence, temporary compression and release, delayed crossing pressure, complex interaction release, and High-level pressure formation. The real-waterway case further showed low and Low-medium pressure fluctuations, local pressure peaks, pressure release, and pressure-source transfer under practical AIS conditions. Prediction-error perturbation analysis indicated that the main high-pressure vessel pairs and pressure-level interpretations remained stable under tested position perturbations. Consistency analysis further showed that ST-TPI scene pressure was significantly correlated with conventional CRI-based encounter-risk indicators. These results indicate that the proposed framework can provide interpretable information on future pressure-evolution and dominant pressure sources, supporting proactive monitoring, early warning, and traffic organization in complex waterways, and contributing to a safer maritime traffic environment.

Keywords: maritime traffic safety; AIS; ship trajectory prediction; multi-ship traffic pressure; Spatio-Temporal Encounter Traffic Pressure Index; LSTM; maritime traffic supervision

Check for updates

Academic Editor: Jinfen Zhang

Received: 3 June 2026
Revised: 26 June 2026
Accepted: 29 June 2026
Published: 2 July 2026

Copyright: © 2026 by the authors. Licensee MDPI, Basel, Switzerland. This article is an open access article distributed under the terms and conditions of the Creative Commons Attribution (CC BY) license.

1. Introduction

The safety of navigation in port approach and departure areas, narrow channels, precautionary zones, and waters where two or more traffic flows intersect is often affected by the cumulative interactions of multiple ships. As the number of vessels in a given water area increases, inter-ship distances, crossing course relationships, speed differences, and encounter sequences may change rapidly within a short period. As a result, the traffic situation becomes highly dynamic and complex. According to the International Maritime Organization guidelines on Vessel Traffic Services (VTS), an important objective of VTS is to improve navigational safety and traffic efficiency and to support maritime traffic management by mitigating the development of unsafe situations in a timely manner [1]. Meanwhile, the Automatic Identification System (AIS) continuously provides dynamic information, such as vessel identity, position, speed, and course, and has become a significant data source for shore-based authorities to perceive maritime traffic situations. Existing studies have demonstrated that, in complex waters, VTS operators are required to focus not only on individual high-risk ships but also on several potential encounter relationships, which greatly increases their situation awareness and decision-making workload [2]. Therefore, safety supervision in complex waters should not be confined to the instantaneous collision risk of a specific ship pair. Instead, greater attention should be paid to traffic pressure induced by vessel aggregation, compression of navigable space, encounter urgency, and inconsistency in motion states.

In this study, multi-ship traffic pressure is defined as the supervisory load generated by the combined effects of vessel aggregation, spatial compression, encounter urgency, and motion-state inconsistency within a short-term traffic scene. It is different from collision risk, which mainly describes the danger of a specific vessel pair; from traffic density, which mainly measures the number or concentration of vessels; and from traffic complexity, which mainly characterizes the structural disorder or navigational difficulty of a traffic system. Traffic pressure emphasizes whether a future multi-ship scene becomes more difficult for VTS operators to monitor, interpret, and manage.

1.1. Related Work

In traditional maritime traffic safety studies, indicators such as DCPA, TCPA, ship domain, and collision-risk index have long been used to represent the spatial proximity and temporal urgency between two ships. Recently, adaptive safety domains, collision-risk indices, velocity obstacles, dynamic ship domains, and ship intrusion risk models have been continuously developed, enabling ship-pair risk assessment to consider vessel dimensions, relative motion, domain intrusion, and encounter geometry more comprehensively [3–7]. These methods are useful for single-ship collision avoidance and local ship-pair danger detection. However, their evaluation is usually based on the present instant or local ship-pair interactions. When multiple encounter relationships coexist and vessel density changes continuously, a single ship-pair risk value cannot adequately describe the overall situation load faced by maritime traffic supervisors.

From the perspective of regional safety management, near-miss detection and regional collision-risk assessment provide a more macroscopic approach to multi-ship traffic safety analysis. AIS-based near-miss detection methods can identify potential traffic conflicts by considering distance, relative speed, and course phase [8]. Improved near-miss detection frameworks have also been used to identify maritime traffic hotspots and support preventive management [9]. In regional collision-risk assessment, clustering, game-allocation principles, RNN, fuzzy inference, and LSTM algorithms have been applied to assist VTS operators in making timely decisions [10,11]. Regional near-miss risk models for open waters further reveal that regional risk cannot remain at the microscopic ship-pair level but

should be comprehensively represented by integrating density complexity and multi-ship risk operators [12]. These studies have promoted the extension of risk assessment from individual-ship pairs to regional levels. Nevertheless, most of them still focus mainly on current conditions, historical statistics, or risk levels at specific moments.

As a complement to regional collision-risk assessment, traffic-complexity research attempts to characterize multi-ship situations in terms of system structure and traffic state. Geng et al. pointed out that risk models mainly based on DCPA and TCPA cannot completely characterize complex maritime traffic situations under increasing traffic density and therefore developed a maritime traffic situation complexity model based on traffic density and traffic conflict [13]. Sui et al. abstracted ships as nodes in a complex network and defined inter-ship relationships as network edges. They used topological indicators such as node degree, node strength, clustering coefficient, and network structure entropy to characterize the evolution of maritime traffic situations [14]. Liu et al. applied a molecular dynamics approach to identify waterway traffic complexity by analyzing ship spatial distribution and motion-parameter distribution, noting that speed and course variations can reflect motion disorder, while spatial distribution can represent the busyness, congestion, and compactness of a water area [15]. Recent studies on multi-ship maritime traffic situation identification and rule-based complex networks have further incorporated density, proximity factors, mitigation difficulty, and COLREG-based collision avoidance relationships into complexity representation, thereby improving VTS operators' situation awareness in complex traffic situations [16,17]. However, most of these studies focus on present or historical traffic conditions, while proactive identification of short-term future pressure evolution remains insufficient.

In addition to spatial structure and motion state, the temporal continuity of traffic risk is also a crucial factor in the supervision of complex waters. Many regional risk assessment approaches focus on the total risk within a statistical period or the risk level at discrete moments. This makes it difficult to reveal the formation, persistence, and migration of risk in the time dimension. Liu and Yu proposed a time-frame regional collision-risk model that builds vessel risk time series from geometric encounters and traffic situation pressure, and then extracts regional risk features using dynamic time warping [18]. This concept indicates that traffic risk and traffic pressure should not be quantified only at a single point in time but should be regarded as temporal processes that develop continuously with multi-ship motion and encounter interactions. For maritime supervision, early identification of future pressure-increasing stages, peak-pressure moments, and dominant pressure sources can provide additional response time for targeted monitoring and traffic management.

In addition to risk assessment and trajectory prediction, AIS data have also been increasingly used for higher-level interpretation of maritime traffic states. Wang et al. used AIS data to identify ship-behavior patterns in port waters, showing that historical vessel motion records can support the recognition of traffic-state changes and ship-behavior characteristics rather than only trajectory reconstruction [19]. From a broader transportation-system perspective, Luo et al. applied machine-learning analysis to transport infrastructure connectivity and conflict resolution, indicating that traffic interactions can be understood as structured multi-agent processes rather than isolated pairwise events [20]. Meanwhile, recent spatiotemporal prediction studies have further shown that spatial and temporal dependencies can be jointly modeled to improve traffic-state forecasting. For example, Chen et al. proposed a bilinear spatiotemporal fusion network for traffic-flow prediction, providing a useful reference for positioning short-term vessel motion prediction within the wider spatiotemporal forecasting literature [21]. These studies support the need to connect AIS-based motion prediction, multi-agent interaction understanding, and interpretable traffic-state assessment in complex multi-ship scenes.

AIS trajectory prediction provides the motion-state basis for looking ahead in maritime traffic supervision. In recent years, LSTM, Bi-LSTM, GRU, attention-based models, and graph neural networks have been used for short-term ship trajectory prediction and have shown good performance in complex waterways and multi-ship traffic scenes [22–26]. These studies have improved the ability to estimate where a vessel may move in the near future. However, from a supervisory perspective, the predicted position itself is only an intermediate result. What matters more is whether the predicted positions of multiple vessels will form a compressed traffic structure, whether encounter urgency will increase, and which vessels may become the main sources of future traffic pressure. Therefore, trajectory prediction needs to be further connected with an interpretable multi-ship traffic-state assessment.

Graph-learning methods have also provided a useful direction for multi-ship collision-risk prediction [27]. By representing vessels as nodes and inter-ship relations as edges, graph-based models can describe the interaction topology of a traffic scene and predict near-future scene-level collision-risk categories. This type of work is valuable because it shifts attention from isolated ship pairs to the whole traffic scene. Nevertheless, its output is usually still a discrete risk category, and the analysis mainly answers whether a scene is likely to become risky. For maritime supervision, this is not always enough. Operators also need to understand how future traffic pressure develops, when the pressure may peak, whether the pressure is caused by local vessel pairs or by wider traffic compression, and which vessels deserve closer attention. Therefore, the focus of this study is further extended from future collision-risk classification to the predictive assessment of multi-ship traffic pressure.

Overall, previous studies have provided important tools for understanding maritime traffic safety from different perspectives. Ship-pair risk models capture the danger in local encounters, regional risk models extend the scope to a larger water area, traffic-complexity studies describe the structure of multi-ship situations, trajectory prediction methods estimate future vessel motion, and graph-learning models start representing the interaction pattern at the scene level.

As shown in Table 1, the proposed ST-TPI framework differs from existing approaches in its prediction-driven and hierarchical assessment structure. It not only evaluates present ship-pair risk or regional traffic complexity, but further converts predicted multi-ship snapshots into ship-pair, individual-ship, regional, and scene-level pressure outputs. This structure allows future pressure evolution, peak-pressure moments, and dominant pressure-contributing vessels or vessel pairs to be identified, which is more directly aligned with proactive VTS supervision.

1.2. Research Gap and Contributions

The study proposes a prediction methodology to analyze traffic pressure in multi-ship traffic scenarios. Based on the AIS trajectory data, the proposed framework first cleans the data, resamples it temporally and reconstructs the continuous trajectories to generate standardized ship motion sequences for model training and scene analysis. Next, an LSTM-based short-term ship motion prediction model is created for predicting the future local-plane displacement of each vessel. Based on this, the single-vessel prediction findings are extended to multi-ship scenarios and the future multi-ship traffic snapshots are recursively generated. Finally, the ST-TPI model is utilized to estimate the current and prospective traffic pressure, including ship-pair pressure, individual-ship pressure, regional pressure, and overall scene pressure.

Table 1. Comparison between existing maritime traffic assessment approaches and the proposed prediction-driven ST-TPI framework.

Method Category	Main Input	Main Output	Temporal Capability	Interpretability	Supervisory Utility
Ship-pair collision-risk assessment	DCPA, TCPA, ship domain, and relative motion	Pairwise risk value or risk level	Mainly current-state assessment	High at the ship-pair level	Identifies dangerous vessel pairs
Regional collision-risk/near-miss assessment	Vessel density, near-miss indicators, and regional risk statistics	Regional risk level or hotspot distribution	Mainly historical or current-state analysis	Moderate	Identifies high-risk water areas
Maritime traffic-complexity assessment	Density, speed/course variation, spatial distribution, and topology	Complexity index or complexity level	Mainly current or historical description	Moderate	Describes traffic busyness, disorder, and structural complexity
Graph-based maritime scene assessment	Vessel nodes, interaction edges, and relative-motion features	Scene-level risk category or interaction pattern	Can support short-term category prediction	Model-dependent	Identifies whether a scene may become risky
Proposed prediction-driven ST-TPI framework	Predicted multi-ship snapshots, DCPA/TCPA, density, proximity, encounter conflict, and motion disorder	Ship-pair, individual-ship, regional, and scene pressure; dominant pressure source; pressure-evolution curve	Predictive pressure evolution over a 30 min horizon	High: Scene pressure can be traced to vessels and vessel pairs	Supports proactive monitoring, peak-pressure identification, and pressure-source tracing

Following this definition, the proposed framework treats traffic pressure as an interpretable supervisory indicator rather than as a direct substitute for collision probability. A scene may generate noticeable pressure even when no single ship pair has reached an extreme collision-risk state, because several neighboring vessels, crossing tendencies, and changing encounter relations may need to be monitored simultaneously.

To address this problem, this paper proposes a predictive assessment method for multi-ship traffic pressure oriented to maritime supervision. The method first converts raw AIS trajectories into continuous motion sequences through data cleaning, temporal resampling, and trajectory reconstruction. A long short-term memory network is then trained to predict short-term vessel motion using local-plane displacement as the output. The predicted states of multiple vessels are synchronized to form future traffic snapshots, in which inter-ship distance, DCPA, TCPA, relative motion, and heading relations are recalculated. On this basis, the Spatio-Temporal Encounter Traffic Pressure Index (ST-TPI) is constructed to evaluate traffic pressure from local density, spatial proximity, encounter conflict, and motion disorder. The pressure results are organized at ship-pair, individual-ship, regional, and scene levels, so that the future pressure process can be described in terms of pressure level, peak moment, dominant vessels, and dominant vessel pairs. A 30 min prediction horizon was selected to match the short-term response needs of VTS-oriented traffic supervision. In practical supervisory waters, operators need sufficient lead time to identify pressure-increasing stages, monitor dominant vessels or vessel pairs, issue early warnings, and organize traffic before local encounter pressure develops into a more difficult scene-level situation. At the same time, ship-motion uncertainty generally increases as the prediction horizon becomes longer, especially when vessels turn, accelerate, decelerate, or maneuver under traffic-control constraints. Therefore, the 30 min

horizon in this study is not intended for long-term route forecasting, but for short-term traffic-pressure trend assessment and proactive supervisory support. The main contributions of this work are listed as follows:

1. A prediction-driven framework for multi-ship traffic-pressure assessment is proposed. Instead of using trajectory prediction only to estimate future positions, the proposed framework further uses predicted vessel states to reconstruct future multi-ship traffic snapshots and to analyze the evolution of traffic pressure within a 30 min horizon.
2. A hierarchical ST-TPI pressure model is developed for maritime supervision. The model evaluates pressure from ship-pair, individual-ship, regional, and overall scene levels, linking local encounter relations with scene-level pressure variation. This structure allows pressure sources to be traced from the overall scene back to dominant vessels and vessel pairs.
3. The proposed framework is validated using five typical multi-ship scenarios and a real-waterway case in the western precautionary area of the Laotieshan Channel. The results show that the method can describe different pressure-evolution processes, including low-pressure persistence, temporary compression and release, delayed crossing pressure, complex interaction release, and pressure growth toward the High level. The real-waterway case further examines its applicability under practical AIS conditions.

The remainder of this paper is organized as follows. Section 2 describes the proposed methodology, including AIS preprocessing, LSTM-based short-term motion prediction, future multi-ship snapshot generation, pairwise encounter-relation extraction, ST-TPI pressure modeling, and temporal scene-pressure assessment. Section 3 presents the prediction performance of the LSTM model, the predictive ST-TPI results in five typical multi-ship scenarios, and the real-waterway case study in the western precautionary area of the Laotieshan Channel. Section 4 discusses the supervisory meaning of predictive traffic pressure assessment, the difference between traffic pressure and conventional collision risk, the interpretability of the proposed indicators, and the limitations of the current work. Section 5 summarizes the main findings and outlines future research directions.

2. Materials and Methods

2.1. Overall Framework

This study develops a predictive traffic pressure assessment framework for multi-ship traffic scenarios. Based on AIS trajectory data, the proposed framework first performs data cleaning, temporal resampling, and continuous trajectory reconstruction to obtain standardized ship motion sequences for model training and scene analysis. Then, an LSTM-based short-term ship motion prediction model is constructed to predict the future local-plane displacement of individual vessels. On this basis, the single-vessel prediction results are extended to multi-ship scenarios, and future multi-ship traffic snapshots are recursively generated. Finally, the ST-TPI model is used to evaluate current and future traffic pressure at multiple levels, including ship-pair pressure, individual-ship pressure, regional pressure, and overall scene pressure.

The overall research procedure consists of five main steps. First, the raw AIS data are preprocessed through field extraction, abnormal-value removal, sine–cosine encoding of angular variables, uniform temporal resampling, and continuous trajectory segmentation, so as to ensure the continuity and consistency of subsequent model inputs. Second, LSTM training samples are constructed from continuous trajectory segments. Historical motion-state sequences are used as model inputs, while the next-step local-plane displacement is used as the prediction target, forming a single-step short-term motion prediction model. Third, the trained LSTM model is recursively applied to each vessel to generate multi-step future predictions, and the predicted states of all vessels at the same future time step are combined

to form a sequence of future multi-ship traffic snapshots. Fourth, pairwise kinematic relations are extracted from each current or future snapshot, and the ST-TPI model is used to calculate ship-pair pressure, individual-ship pressure, regional pressure, and overall scene pressure. Fifth, the prediction performance and traffic pressure assessment results are analyzed using error metrics, pressure time series, and representative pressure snapshots.

The core idea of the proposed framework is to integrate short-term ship motion prediction with traffic pressure evaluation. The LSTM model provides future multi-ship traffic states, while the ST-TPI model quantifies spatial proximity, encounter conflict, local density, and motion disorder in future scenarios. In this way, the proposed framework can evaluate not only the current traffic pressure but also the evolution of multi-ship traffic pressure over a future prediction horizon, providing methodological support for traffic risk identification and situational warning in complex waterways. The overall framework of the proposed method is illustrated in Figure 1. Figure 1 provides a single integrated diagram of the complete procedure from AIS data input to scene-level pressure output. The diagram shows how raw AIS data are first preprocessed and converted into standardized motion sequences, how the LSTM model predicts future vessel states, how future multi-ship traffic snapshots are generated, and how the ST-TPI model further evaluates traffic pressure at ship-pair, individual-ship, regional, and scene levels.

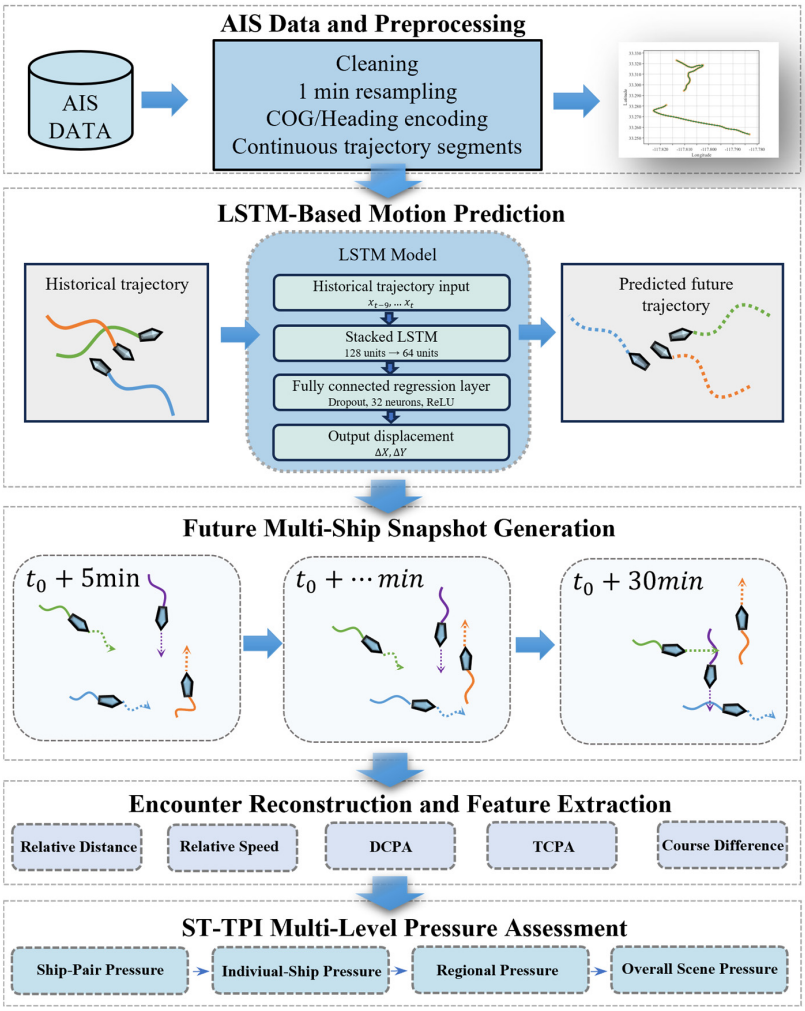


Figure 1. Overall workflow of the proposed prediction-driven LSTM–ST-TPI framework from AIS data input to scene-level pressure output.

The proposed framework is intended for both offline traffic-situation analysis and potential near-real-time VTS decision support. In this study, the framework is mainly validated in an offline manner using historical AIS data, typical multi-ship scenarios, and a real-waterway case. In practical VTS applications, the same computational procedure can be executed in a rolling manner when new AIS observations are received. The updated AIS window can be used to predict short-term vessel states, reconstruct future multi-ship traffic snapshots, and estimate the evolution of traffic pressure. Therefore, the framework should be regarded as an offline-validated predictive assessment method with the potential to support near-real-time traffic monitoring, early warning, and traffic-organization assistance.

2.2. AIS Data Preprocessing and Continuous Trajectory Reconstruction

The AIS data used in this study serve three different purposes. The first type is open-source historical AIS trajectory data obtained from the public Maritime-Monitoring repository [28]. These data are mainly used for training, validation, and testing of the LSTM-based short-term vessel motion prediction model. The second type consists of typical multi-ship traffic segments separately extracted from the same open-source AIS dataset. These segments were selected before pressure calculation based on observable traffic characteristics, including vessel number, spatial distribution, heading consistency, local proximity, crossing tendency, and short-term convergence, rather than on the final ST-TPI values alone. They were used to construct five representative scenarios, including low-density traffic, dense but ordered traffic, crossing encounters, complex multi-ship interactions, and pressure-rising situations, so as to examine the pressure response of the ST-TPI model under different traffic structures. The third type is real-world AIS scenario data from the western precautionary area of the Laotieshan Channel, which is used to examine the engineering applicability of the proposed method in an actual supervisory water area. It should be noted that the 60 vessel trajectory files used for LSTM model training, validation, and testing are not the direct source of the five typical multi-ship scenarios. The former are mainly used to learn short-term vessel motion patterns, whereas the latter are separately selected from multi-ship traffic segments in the open-source AIS dataset to validate the pressure response characteristics of the ST-TPI model under different traffic structures.

To further clarify the data basis of the LSTM-based short-term motion prediction model, the AIS trajectories used for model training, validation, and testing were summarized in Table 2, and their geographical coverage is shown in Figure 2. The dataset contains 60 cargo-vessel trajectory files with 60 unique MMSI and 590,236 original AIS records before 1 min resampling. The records cover the period from 2021 to 2022 and mainly represent underway cargo-vessel cruising trajectories in multiple water areas, including the US West Coast/Northeast Pacific, US East Coast/Northwest Atlantic, Gulf of Mexico/Caribbean, Great Lakes/Inland North America, Hawaii/Central Pacific, and other waters. These trajectories were used to learn general short-term cargo-vessel motion patterns for the LSTM predictor. They were not the direct source of the five typical multi-ship traffic scenarios or the Laotieshan Channel case; the latter datasets were used separately for pressure-response analysis and real-waterway applicability examination.

Table 2. Summary of the AIS dataset used for LSTM model training.

Item	Description/Statistic
Data source	Public AIS cargo-vessel trajectory files from the Maritime-Monitoring repository
Vessel category	Cargo vessels
Number of trajectory files	60
Number of unique MMSI	60
Original AIS records	590,236
Data collection period	1 January 2021 to 31 August 2022
Latitude range	10.39435–55.23470°
Longitude range	−168.45958° to −60.01221°
Main geographical coverage	US West Coast/NE Pacific, US East Coast/NW Atlantic, Gulf of Mexico/Caribbean, Great Lakes/Inland North America, Hawaii/Central Pacific, and other waters
Mean/median SOG	11.52 kn/12.00 kn
SOG range	1.00–24.40 kn
Navigation status	99.59% underway using engine
Role in this study	Used to construct single-vessel motion sequences and train, validate, and test the LSTM short-term motion prediction model

Note: The statistics were calculated from the 60 cargo-vessel AIS trajectory files used for LSTM model training, validation, and testing. The 590,236 records refer to the original AIS records before 1 min resampling. These records were subsequently cleaned, interpolated, and resampled at a 1 min interval; therefore, this number is different from the number of valid resampled trajectory points and sliding-window samples reported insubsequent sample-construction statistics.

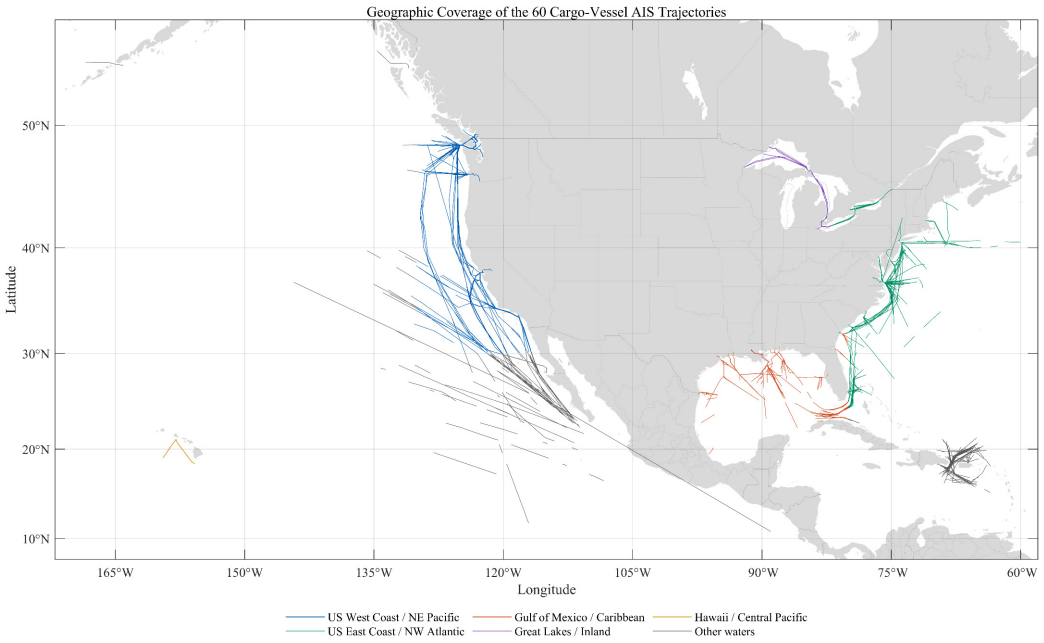


Figure 2. Geographic coverage of the AIS trajectories used for LSTM model training, validation, and testing.

Raw AIS data often contain problems such as irregular time intervals, duplicated reports, local missing records, abnormal longitude or latitude values, abrupt changes in speed or course, and short-term position jumps during data acquisition, transmission, and storage [29,30]. If such data are directly used for trajectory prediction model training, the temporal

scale of input sequences may become inconsistent, and abnormal motion states may be incorrectly learned as real navigation patterns. This may further affect the reliability of future multi-ship traffic-state reconstruction and pressure assessment. Therefore, before constructing LSTM prediction samples, systematic preprocessing of raw AIS trajectories is required to improve the temporal consistency and motion continuity of trajectory sequences [30].

In the basic cleaning stage, the completeness of key AIS fields is first checked, and records with missing ship identifier, track identifier, update time, longitude, latitude, speed, course, or heading are removed. Then, validity constraints are applied to longitude, latitude, speed, course, and heading. Records with unreasonable geographic coordinates, obviously abnormal speeds, or course and heading values outside the valid angular range are deleted. For duplicate records with the same timestamp under the same ship and track identifier, the data are sorted in ascending order of update time, and duplicated records are removed. To further reduce the influence of AIS reporting errors and short-term positioning drift, the instantaneous speed between adjacent trajectory points is estimated based on the time interval and spatial displacement, and abnormal position jumps were identified using an empirical speed-jump threshold of 30 kn, determined according to the cargo-vessel type and the speed distribution of the training dataset, and the corresponding abnormal points were removed [30,31].

After basic cleaning, AIS records were grouped by MMSI and TrackID, and the records within each trajectory were sorted in ascending order of BaseDateTime. Since the original AIS reporting interval is not completely uniform, direct use of the raw time series may lead to inconsistent time spans between adjacent samples in the LSTM input window. Therefore, each trajectory is temporally regularized and resampled with a fixed time step. Specifically, a regular time axis was established for each trajectory using 1 min as the uniform sampling interval, and short missing intervals were filled by interpolation. The 5 min gap threshold was used to distinguish short-term missing reports from long discontinuities in AIS trajectories. If the time interval between two adjacent original AIS observations was no greater than 5 min, missing records were interpolated at a 1 min interval. In contrast, when the interval exceeded 5 min, the trajectory was split rather than interpolated across the gap, because long-gap interpolation may generate artificial motion patterns and introduce unreliable training samples. This setting therefore balances trajectory continuity and data reliability and is consistent with the principle that trajectory repair should be applied conditionally according to data continuity and gap length [31,32]. During resampling, validity labels were used to distinguish trajectory points that could be used for subsequent sample construction from invalid points that were excluded due to excessively long missing intervals.

During resampling, angular variables require special treatment. Both COG and Heading are periodic angular variables. If direct linear interpolation is applied, numerical discontinuities may occur near 0°/360°. For example, 359° and 1° are very close in actual direction, but they appear to be greatly different when represented directly by angular values. To avoid this problem, COG and Heading (HDG) are transformed into sine and cosine components. Specifically, the angular variables COG and HDG were encoded into sine and cosine components to avoid numerical discontinuities near 0°/360°, as follows:

$$\begin{cases} COG_s = sin(COG \cdot \pi/180) \\ COG_c = cos(COG \cdot \pi/180) \\ HDG_s = sin(HDG \cdot \pi/180) \\ HDG_c = cos(HDG \cdot \pi/180) \end{cases} \quad (1)$$

This treatment preserves the continuity of angular variables in circular space and provides more stable input features for the subsequent LSTM model.

After resampling, the temporal continuity of each trajectory was further examined according to the validity labels generated during resampling and the time gaps between adjacent original observations. When the interval between two adjacent original AIS observations exceeded 5 min, the trajectory was split at that point, forming several continuous trajectory segments. This segmentation avoids treating long-term missing intervals as continuous vessel motion and helps preserve the reliability of subsequent prediction samples [32,33]. Each continuous segment had a uniform time step and relatively good motion continuity and was therefore used for subsequent short-term trajectory prediction sample construction. Segments shorter than the sum of the historical input length and the prediction output length were removed to ensure that each sample contained a complete input window and the corresponding prediction label.

To illustrate the AIS preprocessing procedure, the overall workflow is summarized in Figure 3. After raw AIS data are input, field completeness checking and abnormal-record removal are first performed. The records are then grouped by MMSI and TrackID and sorted by BaseDateTime, followed by resampling at a uniform interval of 1 min. For angular variables, COG and Heading are transformed into sine and cosine forms. Finally, the resampled trajectories are divided into continuous trajectory segments according to temporal continuity, and historical input windows and prediction labels required by the LSTM model are constructed.

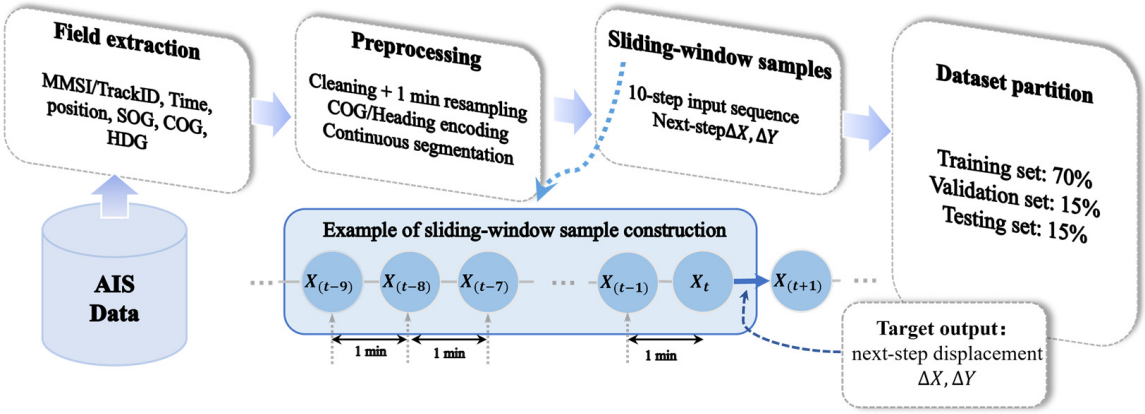


Figure 3. Workflow of AIS data preprocessing and continuous trajectory sample construction.

In addition to the workflow diagram, a typical segment of ship trajectory is picked, and the raw trajectory, cleaned trajectory, and trajectory after resampling and continuous reconstruction are compared, as shown in Figure 4. This picture is used to show the potential difficulties in raw AIS trajectories, such as unequal distribution of points, local anomalous jumps, and time gaps. It also shows that after cleaning, resampling and continuous trajectory segmentation, the trajectory data are transformed into regular sequences with uniform time intervals and reasonably continuous motion states.

Through the above processing, the raw AIS trajectories are converted into continuous trajectory samples suitable for training the LSTM-based short-term motion prediction model. For model training, validation, and testing, 60 single-vessel trajectory files are used to construct sliding-window samples, so as to learn short-term local displacement patterns of vessels at a 1 min time interval. For typical scenario validation, multi-ship traffic segments are separately extracted from the open-source AIS dataset to construct five representative scenarios with different vessel densities, encounter structures, and pressure-evolution characteristics. For real-waterway validation, AIS data from the western precautionary area of the Laotieshan Channel are used to extract historical motion windows of multiple vessels at specified snapshot times. These three types of data respectively

support motion prediction model training, typical-scenario pressure response analysis, and real-waterway engineering validation, jointly providing the data basis for recursive prediction, future multi-ship traffic snapshot generation, encounter relationship calculation, and ST-TPI-based multi-level pressure assessment.

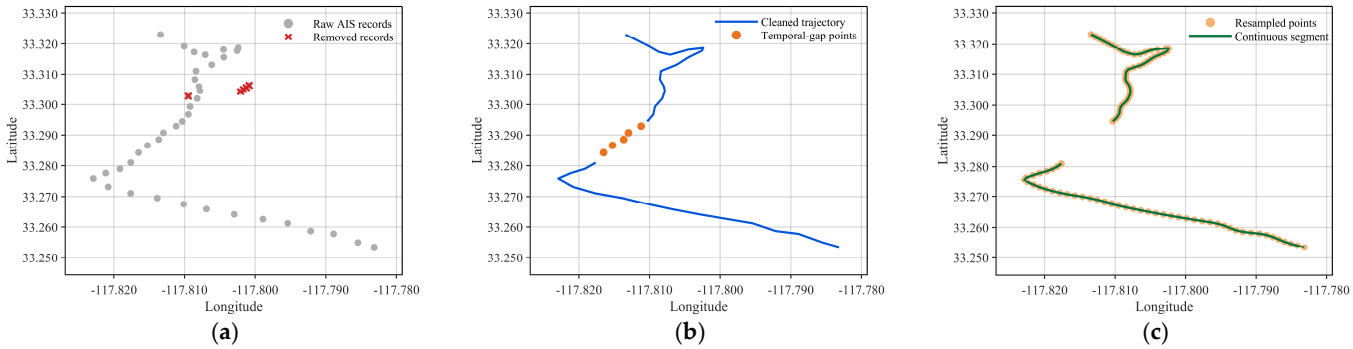


Figure 4. Example of AIS trajectory cleaning, resampling, and continuous trajectory reconstruction. (**a**) Raw AIS trajectory records. (**b**) Cleaned trajectory after abnormal-point removal and temporal-gap identification. (**c**) Resampled continuous trajectory segments.

2.3. Construction of the LSTM-Based Short-Term Ship Motion Prediction Model

A stacked LSTM network was used to develop the short-term ship motion forecast model. Similar recurrent and deep learning models have been widely employed in AIS-based short-term vessel trajectory prediction and have been shown to be able to learn temporal motion patterns from past ship states [34,35]. The model takes the historical motion-state sequence as input and outputs the next-step local-plane displacement in the east–west and north–south directions. The network is composed of the sequence input layer, two LSTM layers, a dropout layer, a fully connected layer with ReLU activation function and a fully connected regression layer. The first LSTM layer has 128 hidden units and returns the whole sequence of hidden states. The second LSTM layer has 64 hidden units and delivers only the last hidden state. A dropout layer with a dropout rate of 0.1 was used to reduce overfitting. The recovered temporal representation is then fed into a fully connected layer with 32 neurons and a ReLU activation function. The output of this layer is sent into a final fully connected layer, which produces the two-dimensional displacement vector. The following subsections discuss how to build input features, output representation, partition the dataset, and evaluate the prediction error based on this architecture.

After AIS data cleaning, resampling, and continuous trajectory reconstruction, the continuous trajectory segments were used to construct input samples for the LSTM-based short-term ship motion prediction model. Since the original longitude and latitude are geographic coordinates, directly using them as model inputs may lead to inconsistent spatial scales in different directions. Therefore, each continuous trajectory segment was first converted into a local planar coordinate system.

2.3.1. Input Feature Construction and Normalization

The approximate metric conversion was used to convert the longitude and latitude into local planar coordinates for a short-term forecast in the local water region. Specifically, one degree of latitude was approximated as 111,320 m, and the scale of longitude was corrected by the cosine of the reference latitude. For each continuous segment, the first trajectory point was chosen as the local reference point, and its longitude and latitude were

labeled by Lon_0 and Lat_0 accordingly. The local flat coordinates of the t-th trajectory point were determined as

$$\begin{cases} X_t = (Lon_t - Lon_0) \times 111320 \times \cos\left(\frac{Lat_0 \times \pi}{180}\right) \\ Y_t = (Lat_t - Lat_0) \times 111320 \end{cases} \quad (2)$$

where X_t and Y_t denote the east–west and north–south positions of the vessel in the local planar coordinate system, respectively, with the unit of meters. This transformation converts the ship position from geographic coordinates into metric spatial coordinates, which are more suitable for local-plane displacement prediction and position-error calculation. Since this study focuses on short-term motion prediction and traffic-state evolution within local waters, the above approximation is sufficient for model input construction and prediction-error evaluation.

To further represent the short-term motion tendency of the vessel, the displacement increments between adjacent trajectory points were introduced as motion variation features. The historical displacement increments at time step t were defined as

$$\begin{cases} dX_t^{prev} = X_t - X_{t-1} \\ dY_t^{prev} = Y_t - Y_{t-1} \end{cases} \quad (3)$$

where dX_t^{prev} and dY_t^{prev} represent the east–west and north–south motion changes during the previous time interval, respectively. For the first point of each continuous trajectory segment, the previous displacement increments were set to zero because no preceding point was available.

The position state, speed state, historical displacement state, and angular state were fused into a nine-dimensional motion-state feature vector for each time step. The input feature vector for the t-th time step was defined as:

$$\mathbf{x}_t = \left[X_t, Y_t, SOG_t, dX_t^{prev}, dY_t^{prev}, COG_{s,t}, COG_{c,t}, HDG_{s,t}, HDG_{c,t}\right]^T \quad (4)$$

where SOG_t denotes the speed over ground, COGt denotes the course over ground, and HDGt denotes the heading. Since COG and HDG are periodic angular variables, their sine and cosine components were used to represent the angular states, thereby avoiding numerical discontinuities near $0^\circ/360^\circ$. In this way, the model can learn not only the current spatial position of the vessel but also its speed, previous displacement variation, and directional motion characteristics. Similar position-, speed-, and course-related motion features have also been commonly used in AIS-based trajectory prediction studies [33,34]. The detailed description of the input features is summarized in Table 3.

Table 3. Motion-state input features for the LSTM-based short-term ship motion prediction model.

Feature	Description	Unit/Range
X	Local east–west position	m
Y	Local north–south position	m
SOG	Speed over ground	kn
dX^{prev}	Previous east–west displacement increment	m
dY^{prev}	Previous north–south displacement increment	m
COG_s	Sine component of course over ground	$[-1, 1]$
COG_c	Cosine component of course over ground	$[-1, 1]$
HDG_s	Sine component of heading	$[-1, 1]$
HDG_c	Cosine component of heading	$[-1, 1]$

A sliding-window strategy was then used to extract historical input sequences from each continuous trajectory segment. Let L_{in} denote the historical input length. In this study, $L_{in} = 10$, meaning that each input sample contains the motion states of ten consecutive historical time steps. The i-th input sample can be expressed as

$$\boldsymbol{X_i} = \left[x_i, x_{i+1}, \ldots, x_{i+L_{in}-1}\right] \tag{5}$$

Therefore, each LSTM input sample has a dimension of $9 \times L_{in}$. Before model training, the position, speed, and displacement-related features were normalized using min–max normalization based only on the statistics of the training subset, so as to reduce the influence of different numerical scales and avoid information leakage from the validation and testing subsets. The normalization process can be expressed as

$$\tilde{z} = \frac{z - z_{min}^{train}}{z_{max}^{train} - z_{min}^{train}} \tag{6}$$

where z denotes the feature to be normalized, and z_{min}^{train} and z_{max}^{train} denote the minimum and maximum values of the corresponding feature in the training subset, respectively. The angular variables were already represented by sine and cosine components within the range of $[-1, 1]$, and were therefore directly used as input features. Through the above processing, continuous AIS trajectories were transformed into standardized motion-state sequences suitable for LSTM learning, providing the input basis for subsequent local-plane displacement prediction.

2.3.2. Local-Plane Displacement Output Representation

Based on the input sequence constructed in Section 2.3.1, the prediction target of the LSTM model was defined as the next-step displacement increment in the local planar coordinate system, rather than the absolute longitude and latitude of the next position. This design was adopted because longitude and latitude are geographic coordinates, whereas local planar displacement is expressed in meters and can directly describe the actual short-term motion change in a vessel. In addition, displacement increments are more suitable for representing local motion tendencies than absolute positions.

For each input sample, the displacement from the last historical point to the next time step was used as the prediction label. The target displacement was defined as

$$\begin{cases} \Delta X_{i+L_{in}} = X_{i+L_{in}} - X_{i+L_{in}-1} \\ \Delta Y_{i+L_{in}} = Y_{i+L_{in}} - Y_{i+L_{in}-1} \end{cases} \tag{7}$$

Thus, the output label of the i-th sample can be expressed as

$$\mathbf{y}_i = \left[\Delta X_{i+L_{in}}, \Delta Y_{i+L_{in}}\right]^T \tag{8}$$

where ΔX and ΔY denote the east–west and north–south displacement increments during the next sampling interval, respectively. Since the AIS trajectories were uniformly resampled at a 1 min interval, the output label represents the local planar displacement of the vessel in the next minute.

The LSTM model can therefore be regarded as a nonlinear mapping from the historical motion-state sequence to the next-step displacement increment:

$$\hat{\mathbf{y}}_i = f_\theta(\mathbf{X}_i) \tag{9}$$

where $f_\theta(\cdot)$ denotes the mapping function learned by the LSTM network, and θ represents the trainable model parameters. The predicted output can be written as

$$\hat{\mathbf{y}}_i = \left[\Delta\hat{X}_{i+L_{in}}, \Delta\hat{Y}_{i+L_{in}}\right]^T \tag{10}$$

After obtaining the predicted displacement, the predicted local planar position at the next time step was reconstructed by adding the predicted displacement to the last historical position in the input window:

$$\begin{cases} \hat{X}_{i+L_{in}} = X_{i+L_{in}-1} + \Delta\hat{X}_{i+L_{in}} \\ \hat{Y}_{i+L_{in}} = Y_{i+L_{in}-1} + \Delta\hat{Y}_{i+L_{in}} \end{cases} \tag{11}$$

Furthermore, the next-step predicted geographic position can be recovered from the predicted local planar displacement and the current longitude and latitude:

$$\begin{cases} \widehat{Lon}_{i+L_{in}} = Lon_{i+L_{in}-1} + \dfrac{\Delta\hat{X}_{i+L_{in}}}{111320\cos\left(Lat_{i+L_{in}-1}\pi/180\right)} \\ \widehat{Lat}_{i+L_{in}} = Lat_{i+L_{in}-1} + \dfrac{\Delta\hat{Y}_{i+L_{in}}}{111320} \end{cases} \tag{12}$$

This output representation allows the model to maintain a concise two-dimensional output structure while still reconstructing the future vessel position. Although the LSTM model outputs only two displacement components, these two components directly determine the predicted position at the next time step. Therefore, this output design is consistent with the subsequent recursive prediction, future multi-ship traffic snapshot generation, and encounter-structure reconstruction.

During model training, the output displacement labels were normalized using min–max normalization based only on the training subset:

$$\begin{cases} \widetilde{\Delta X} = \dfrac{\Delta X - \Delta X_{min}^{train}}{\Delta X_{max}^{train} - \Delta X_{min}^{train}} \\ \widetilde{\Delta Y} = \dfrac{\Delta Y - \Delta Y_{min}^{train}}{\Delta Y_{max}^{train} - \Delta Y_{min}^{train}} \end{cases} \tag{13}$$

After prediction, inverse normalization was performed to recover the displacement values in meters, which were then used for position reconstruction and prediction-error evaluation.

2.3.3. Training, Validation, and Testing Dataset Partitioning

After constructing the input features and output labels, the LSTM samples were further divided into training, validation, and testing subsets. Since AIS trajectories have strong temporal continuity, adjacent sliding-window samples are highly correlated. If all samples were randomly divided, adjacent time windows could appear simultaneously in the training and testing subsets, resulting in information leakage and an overestimation of the model's generalization performance. Therefore, in this study, the dataset was partitioned according to the temporal order within each continuous trajectory segment rather than by random sample shuffling. This segment-wise temporal partitioning was applied independently to each continuous trajectory segment.

For a continuous trajectory segment containing N valid resampled trajectory points, the proportions of the training, validation, and testing subsets were set to 70%, 15%, and 15%, respectively. The endpoint of the training part and the endpoint of the validation part were defined as

$$\begin{cases} N_{train} = \lfloor 0.70N \rfloor \\ N_{val} = \lfloor 0.85N \rfloor \end{cases} \tag{14}$$

where N_{train} denotes the endpoint of the training part, N_{val} denotes the endpoint of the validation part, and the floor operator is used to obtain integer indices. The first 70% of the trajectory points were used to construct training samples, the following 15% were used to construct validation samples, and the remaining 15% were used to construct testing samples.

To ensure that both the input window and the corresponding prediction label of each sample belonged to the same subset, the sample start indices were further selected according to the sliding-window position. Let L_{in} denote the input window length. The input window of the i-th sample covers the historical time steps from i to $i + L_{in} - 1$, and its prediction label corresponds to the time step $i + L_{in}$. The index sets of training, validation, and testing samples were therefore defined as

$$\begin{cases} \mathcal{I}_{train} & = \{i \mid i + L_{in} \leq N_{train}\} \\ \mathcal{I}_{val} & = \{i \mid i \geq N_{train} + 1, i + L_{in} \leq N_{val}\} \\ \mathcal{I}_{test} & = \{i \mid i \geq N_{val} + 1, i + L_{in} \leq N\} \end{cases} \tag{15}$$

With this partitioning strategy, the training, validation, and testing samples were temporally separated, and overlapping sliding windows across different subsets were avoided. Continuous trajectory segments that were too short to provide non-empty training, validation, and testing samples were excluded from model training, ensuring that each retained segment contributed complete samples for the three subsets.

To further clarify the data scale used for model training, the numbers of valid resampled AIS trajectory points, continuous trajectory segments, and sliding-window samples were summarized, as shown in Table 4. Although the data used for LSTM model training were derived from 60 vessel trajectory files, the preprocessing and segmentation procedure transformed them into 4667 continuous motion segments and further generated 615,635 sliding-window samples. This strategy makes full use of the short-term motion information embedded in continuous AIS trajectories and supports the LSTM model in learning local short-term vessel displacement patterns. Meanwhile, to avoid information leakage caused by overlapping adjacent sliding windows appearing across different subsets, the training, validation, and testing subsets were divided according to the temporal order within each continuous trajectory segment rather than by random shuffling of all samples.

Table 4. Statistics of AIS trajectory sample construction for the LSTM motion prediction model.

Item	Number
Original vessel trajectory files	60
Valid resampled trajectory points	714,378
Continuous trajectory segments	4667
Available sliding-window samples	615,635
Training samples	446,337
Validation samples	84,305
Testing samples	84,993

It should be noted that the present dataset partitioning was conducted in a segment-wise temporal manner rather than in a vessel-disjoint manner. In other words, samples from the same vessel trajectory could appear in different subsets, but their temporal order was preserved, and overlapping sliding-window samples across the training, validation, and testing subsets were avoided. This design was adopted because the main objective of the prediction module in this study is to learn short-term cargo-vessel motion patterns from continuous AIS trajectories and to provide stable motion-state inputs for subsequent ST-TPI pressure assessment. Therefore, the reported prediction errors mainly reflect the temporal

generalization ability within cargo-vessel trajectory segments under non-overlapping time partitions. A fully vessel-disjoint evaluation, in which vessels appearing in the training subset are completely excluded from the testing subset, would provide a stricter assessment of cross-vessel generalization and will be considered in future work.

The training subset was used to learn the LSTM network parameters. The validation subset was used to monitor model performance during training, select the network with the minimum validation loss, and reduce the risk of overfitting. The testing subset was not involved in model training or parameter selection and was used only for final prediction accuracy evaluation. In the model training process, the Adam optimizer was adopted, the maximum number of epochs was set to 60, the mini-batch size was set to 64, and the initial learning rate was set to 0.001. The validation subset was used for performance monitoring during training, and the network with the best validation loss was retained as the final prediction model. This setting allowed the model to learn short-term ship motion patterns from the training samples while evaluating its generalization ability using independent validation and testing subsets. The main dataset partitioning and model training settings are summarized in Table 5.

Table 5. Dataset partitioning and model training settings.

Item	Setting
Resampling interval	1 min
Input sequence length	10 steps
Training subset	70%
Validation subset	15%
Testing subset	15%
Optimizer	Adam
Maximum epochs	60
Mini-batch size	64
Initial learning rate	0.001
Model selection criterion	Best validation loss

A preliminary hyperparameter tuning process was conducted using the validation subset to determine the final LSTM network configuration. Several candidate settings were compared, including one-layer and two-layer LSTM structures, hidden-unit sizes ranging from 64 to 128, dropout rates from 0 to 0.2, mini-batch sizes from 32 to 128, and initial learning rates from 0.0005 to 0.001. The validation loss and testing stability were jointly considered during model selection. The final configuration, consisting of two LSTM layers with 128 and 64 hidden units, a dropout rate of 0.1, a fully connected layer with 32 neurons, a mini-batch size of 64, and an initial learning rate of 0.001, was selected because it achieved relatively low validation loss while maintaining stable testing performance and moderate computational cost. This configuration provides a balance between prediction accuracy, model complexity, and computational efficiency for subsequent future multi-ship snapshot generation.

2.3.4. Prediction-Error Evaluation Metrics

To quantitatively evaluate the accuracy of the LSTM-based short-term ship motion prediction model, prediction errors were calculated in the local planar coordinate system. Since the local planar coordinates are expressed in meters, the error values directly represent the spatial deviation between the predicted and actual ship positions. This avoids the scale inconsistency that may occur when longitude and latitude differences are directly used.

For the i-th prediction sample, let (X_i, Y_i) denote the actual position and $(\hat{X}_i, \hat{Y}_i)$ denote the predicted position. The two-dimensional Euclidean position error was calculated as

$$e_i = \sqrt{(\hat{X}_i - X_i)^2 + (\hat{Y}_i - Y_i)^2} \tag{16}$$

where e_i denotes the planar position error of the i-th sample, with the unit of meters.

Based on the Euclidean position error, the mean position error (MPE) was calculated as

$$MPE = \frac{1}{N}\sum_{i=1}^{N} e_i \tag{17}$$

where N denotes the number of prediction samples, and MPE represents the average planar position deviation between the predicted and actual positions.

The mean absolute error (MAE) was used to evaluate the average absolute deviation in the east–west and north–south coordinate directions:

$$MAE = \frac{1}{2N}\sum_{i=1}^{N}(|\ \hat{X}_i - X_i\ | + |\ \hat{Y}_i - Y_i\ |) \tag{18}$$

where N denotes the number of prediction samples. MAE reflects the coordinate-level absolute error averaged over the east–west and north–south directions, whereas MPE reflects the mean Euclidean position error.

The root mean square error (RMSE) was used to measure the overall magnitude of the position prediction error based on the Euclidean position error:

$$RMSE = \sqrt{\frac{1}{N}\sum_{i=1}^{N} e_i^2} \tag{19}$$

Compared with MAE, RMSE is more sensitive to large local deviations and can therefore indicate whether obvious large-error samples exist in the prediction results.

For horizon-based multi-step prediction sequences, the average displacement error (ADE) and final displacement error (FDE) were further used to evaluate trajectory-level prediction performance. Suppose that there are M predicted trajectories, each containing H prediction steps, and $e_{m,h}$ denotes the Euclidean position error of the m-th trajectory at the h-th prediction step. ADE and FDE were defined as

$$\begin{cases} ADE &= \dfrac{1}{MH}\displaystyle\sum_{m=1}^{M}\sum_{h=1}^{H} e_{m,h} \\ FDE &= \dfrac{1}{M}\displaystyle\sum_{m=1}^{M} e_{m,H} \end{cases} \tag{20}$$

where ADE represents the average position deviation over the whole prediction horizon, while FDE represents the terminal-position error at the final prediction step. In this study, MAE, MPE, and RMSE were mainly used to evaluate one-step prediction accuracy, whereas ADE and FDE were used to describe the error accumulation characteristics of horizon-based rolling prediction and future multi-step trajectory generation.

Overall, MAE describes the average coordinate-level deviation, MPE measures the mean Euclidean position deviation, RMSE evaluates the overall position error with sensitivity to large deviations, ADE measures the average trajectory deviation over a prediction horizon, and FDE reflects the terminal-position error. These metrics provide the accuracy evaluation basis for the LSTM-based short-term motion prediction model and support

the reliability analysis of subsequent future multi-ship traffic snapshot generation and ST-TPI-based traffic pressure assessment.

2.4. Future Multi-Ship Traffic Snapshot Generation and Pairwise Relation Extraction

2.4.1. Historical Window Extraction and Prediction Input Construction

After constructing the LSTM-based short-term motion prediction model, the single-vessel prediction model was further applied to multi-ship traffic scenes. AIS-based multi-ship encounter studies commonly reconstruct traffic situations by organizing vessel states at the same time and extracting inter-ship relations, which provides a basis for subsequent encounter analysis and risk assessment [36]. For a given scene snapshot time t_0, vessel states located within the study area were first extracted from the valid resampled AIS trajectories. To ensure that each vessel contained sufficient historical motion information, only vessels with L_{in} consecutive valid historical trajectory points before t_0 were retained for subsequent prediction. Thus, each vessel corresponded to a fixed-length historical motion window.

For the j-th vessel, the historical window can be expressed as

$$\begin{cases} \mathcal{W}_j(t_0) & = \left[\mathbf{s}_j(t_0 - L_{in} + 1), \mathbf{s}_j(t_0 - L_{in} + 2), \ldots, \mathbf{s}_j(t_0)\right] \\ \mathbf{s}_j(t) & = \left[Lon_j(t), Lat_j(t), SOG_j(t), COG_j(t), HDG_j(t)\right]^T \end{cases} \tag{21}$$

where $\mathcal{W}_j(t_0)$ denotes the historical motion window of the j-th vessel before the snapshot time t_0, $L_{in} = 10$, and $\mathbf{s}_j(t)$ represents the basic motion state of the vessel at time t. The trajectory points in the historical window were required to have a uniform time interval, namely $\Delta t = 1$ min.

The historical window was then transformed into the same nine-dimensional input feature sequence as used in the model training stage in Section 2.3, including local planar position, speed over ground, previous displacement increments, and the sine and cosine components of COG and Heading. The position-, speed-, and displacement-related features were normalized using the normalization parameters saved during model training, while the angular variables were kept in their sine and cosine forms. This ensured that the input format during multi-ship prediction was consistent with that used during LSTM model training.

2.4.2. Recursive Multi-Step Prediction for Individual Vessels

Since the LSTM model constructed in this study is a single-step displacement prediction model, its outputs are the local planar displacement increments $\Delta\hat{X}$ and $\Delta\hat{Y}$ at the next time step. To obtain vessel motion states over a future time horizon, a recursive strategy was adopted to extend single-step prediction to multi-step prediction. For each vessel, at the h-th prediction step, the LSTM input was first constructed from the current rolling historical window. The model then predicted the next-step displacement increment, which was added to the current vessel position to reconstruct the predicted position at the next time step.

The recursive prediction process can be expressed as

$$\begin{cases} \left[\Delta\hat{X}_{j,h}, \Delta\hat{Y}_{j,h}\right]^T & = f_\theta\left(\mathcal{W}_j^{(h-1)}\right) \\ \hat{X}_{j,h} & = \hat{X}_{j,h-1} + \Delta\hat{X}_{j,h} \\ \hat{Y}_{j,h} & = \hat{Y}_{j,h-1} + \Delta\hat{Y}_{j,h} \end{cases} \tag{22}$$

where $f_\theta(\cdot)$ denotes the trained LSTM model, $\mathcal{W}_j^{(h-1)}$ denotes the rolling historical window of the j-th vessel at prediction step $h-1$, and $\left(\hat{X}_{j,h}, \hat{Y}_{j,h}\right)$ denotes the predicted local planar position at the h-th prediction step.

The predicted position was further converted back into geographic coordinates using the predicted displacement and the previous predicted longitude and latitude:

$$\begin{cases} \widehat{Lon}_{j,h} & = \widehat{Lon}_{j,h-1} + \frac{\Delta\hat{X}_{j,h}}{111320\cos\left(\widehat{Lat}_{j,h-1}\pi/180\right)} \\ \widehat{Lat}_{j,h} & = \widehat{Lat}_{j,h-1} + \frac{\Delta\hat{Y}_{j,h}}{111320} \end{cases} \tag{23}$$

where $\widehat{Lon}_{j,0} = Lon_j(t_0)$ and $\widehat{Lat}_{j,0} = Lat_j(t_0)$, indicating that the recursive prediction starts from the observed vessel position at the current snapshot time.

When the predicted state was used to update the rolling window, the complete motion-state variables required by the next LSTM input were reconstructed from the predicted displacement. The predicted SOG was calculated from the magnitude of the predicted displacement and converted from m/min to knots:

$$\widehat{SOG}_{j,h} = \frac{\sqrt{\left(\Delta\hat{X}_{j,h}\right)^2 + \left(\Delta\hat{Y}_{j,h}\right)^2}}{\Delta t} \times \frac{60}{1852} \tag{24}$$

where $\Delta t = 1$ min in this study. The predicted COG was calculated from the east–west and north–south displacement components:

$$\widehat{COG}_{j,h} = \mathrm{mod}\left[\mathrm{atan}\,2\left(\Delta\hat{X}_{j,h}, \Delta\hat{Y}_{j,h}\right)\frac{180}{\pi}, 360\right] \tag{25}$$

The predicted heading was set equal to the predicted COG in the current implementation. This approximation is acceptable for ordinary underway cargo-vessel motion because the difference between heading and COG is usually small when vessels sail steadily at normal speed. In such cases, COG can provide a reasonable directional representation for short-term encounter reconstruction and ST-TPI pressure calculation.

However, this assumption may introduce uncertainty during sharp maneuvers, low-speed movement, berthing or unberthing operations, or strong current and wind conditions. In these situations, the vessel heading may differ noticeably from the actual course over ground, and using COG as a proxy for heading may affect heading-difference calculation, encounter-angle classification, motion-disorder estimation, and the reconstructed pressure contribution of local vessel pairs. Therefore, the predicted heading in this study should be interpreted as an approximate directional state for short-term traffic-pressure assessment rather than as an exact maneuvering-state prediction. Future work may further incorporate direct heading prediction or maneuvering-aware models to improve the representation of vessel attitude under complex motion conditions.

Then, the predicted longitude, latitude, SOG, COG, and heading were combined with the reconstructed local planar position and previous displacement increments to form a complete predicted motion state. This predicted state was appended to the rolling window, while the earliest historical state was removed, so that the next-step LSTM input could be constructed recursively. This recursive updating process was repeated until the entire prediction horizon was completed. In the predictive ST-TPI assessment, the rolling window was updated recursively using the predicted states, so that the future traffic snapshots were generated in a prediction-driven manner.

2.4.3. Future Multi-Ship Traffic Snapshot Generation

After recursive multi-step prediction was completed for each vessel, the prediction results of all vessels were organized according to the same future time steps to generate future multi-ship traffic snapshots. In this study, recursive prediction was performed at a 1 min time step, consistent with the resampled AIS interval. The intermediate one-minute predicted states were used for recursive trajectory propagation. For pressure assessment and visualization, future snapshots at 5 min intervals within the 30 min prediction horizon were selected, namely 5, 10, 15, 20, 25, and 30 min. These selected snapshots were then used for predictive ST-TPI assessment and visualization. Each future snapshot represents the predicted state set of all vessels in the scene at a specific prediction time. For prediction step h, the future snapshot can be expressed as

$$\mathcal{S}_{t_0+h\Delta t} = \left\{\hat{\mathbf{s}}_1(t_0+h\Delta t), \hat{\mathbf{s}}_2(t_0+h\Delta t), \ldots, \hat{\mathbf{s}}_{n_h}(t_0+h\Delta t)\right\} \tag{26}$$

where $\mathcal{S}_{t_0+h\Delta t}$ denotes the future multi-ship traffic snapshot at prediction time $t_0+h\Delta t$, n_h denotes the number of vessels in the snapshot, and $\hat{\mathbf{s}}_j(t)$ represents the predicted motion state of the j-th vessel at time t. Each snapshot contains vessel identifiers and predicted motion-state variables, including ShipID, TrackID, predicted longitude, predicted latitude, SOG, COG, and heading.

In the implementation, the current snapshot was constructed from the last state in the historical window of each vessel, while each future snapshot was constructed by combining the predicted states of all vessels at the same prediction step. For each future prediction step, the predicted longitude, latitude, speed, course, and heading information of all vessels were extracted and organized into a snapshot table with a consistent structure. The resulting future snapshot sequence describes the temporal evolution of the predicted multi-ship traffic state and provides a unified input for the subsequent ST-TPI pressure evaluation.

2.4.4. Pairwise Relation Extraction for ST-TPI Evaluation

After future multi-ship traffic snapshots were generated, pairwise vessel relations were further constructed within each snapshot to provide the basis for the subsequent ST-TPI-based multi-level pressure evaluation. Similar pairwise-relation extraction has been widely used in AIS-based encounter analysis, where relative distance, relative speed, course difference, DCPA, and TCPA are important variables for describing ship interactions [36]. For a given future snapshot $\mathcal{S}_{t_0+h\Delta t}$, all vessels in the snapshot were paired to form a candidate vessel-pair set:

$$\mathcal{P}_{t_0+h\Delta t} = \left\{(i,j) \mid 1 \le i < j \le n_h, i, j \in \mathcal{S}_{t_0+h\Delta t}\right\} \tag{27}$$

where $\mathcal{P}_{t_0+h\Delta t}$ denotes the candidate vessel-pair set at prediction time $t_0+h\Delta t$. For each vessel pair, pairwise kinematic quantities such as relative distance, relative speed, DCPA, and TCPA can be further extracted. These pairwise kinematic relations are not expanded as independent pressure formulas in this section; instead, they are used as inputs for the ST-TPI ship-pair pressure calculation in Section 2.5.

2.5. ST-TPI-Based Multi-Level Traffic Pressure Evaluation

After obtaining the current and future multi-ship traffic snapshots, an ST-TPI-based multi-level traffic pressure evaluation model was further constructed to quantitatively characterize local ship-pair conflicts, individual-ship pressure, regional traffic pressure, overall scene pressure, and their temporal evolution. This hierarchical design follows the idea that multi-ship traffic safety should be interpreted not only from local ship-pair relations, but also from regional and scene-level traffic states [37]. Unlike risk assessment

methods based only on a single distance or encounter indicator, the ST-TPI framework evaluates traffic pressure progressively from the ship-pair level to the individual-ship, regional, and overall scene levels.

Specifically, for each current or future multi-ship snapshot, all vessels were first paired to calculate pairwise kinematic variables, including relative position, relative velocity, DCPA, TCPA, closing speed, and heading difference. These variables were then used to calculate pairwise spatial pressure and encounter-conflict pressure. Based on these pairwise relations, four pressure components were calculated for each vessel, including local density pressure, spatial proximity pressure, encounter-conflict pressure, and motion-disorder pressure. These components were then combined to obtain the individual-ship ST-TPI pressure. Subsequently, individual-ship pressures were aggregated into regional pressure, and the overall scene-pressure index was finally calculated by integrating the ship-pressure distribution, regional pressure, maximum pair pressure, ship-number pressure, and high-pressure pair ratio.

Therefore, the ST-TPI evaluation process can be summarized in Figure 5:

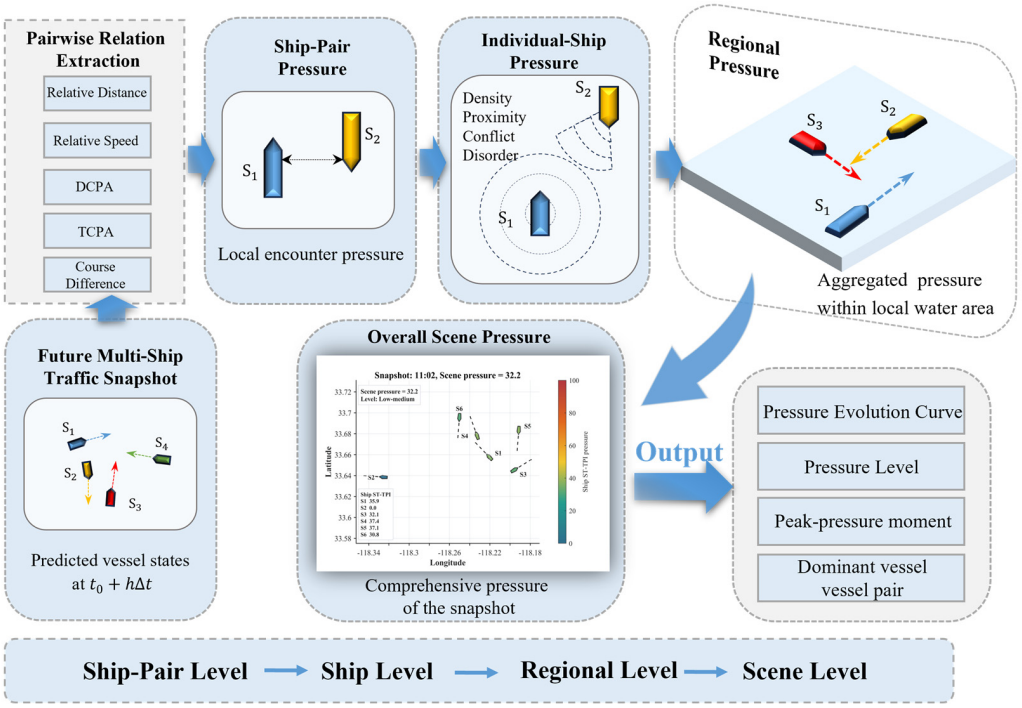


Figure 5. ST-TPI-based multi-level traffic pressure evaluation framework.

This multi-level structure can reflect both local ship-pair conflicts and the overall traffic pressure of the scene, providing the computational basis for the future pressure snapshots and pressure-evolution curves presented in Section 3. The detailed parameter settings and justification of the ST-TPI model are provided in Appendix A.

To improve the readability of the ST-TPI formulation, the key symbols, hierarchical outputs, and pressure-level definitions used in the proposed framework are summarized in Table 6. In this study, P denotes a normalized pressure value on a 0–100 scale, and the pressure-level intervals are mainly used for scene-level interpretation.

Table 6. Consolidated summary of ST-TPI symbols, hierarchical pressure outputs, and vessel/scene-level measures.

Level/Quantity	Symbol	Meaning and Interpretation
Pairwise kinematic input	D_{ij}, DCPA_{ij}, TCPA_{ij}	Inter-vessel distance, distance at closest point of approach, and time to closest point of approach; used to describe proximity and encounter urgency.
Pairwise pressure components	${Q_{ij}}^{spa}$, ${C_{ij}}^{conf}$	Spatial-proximity pressure and encounter-conflict pressure between vessels i and j; used to describe local compression and pairwise urgency.
Ship-pair pressure	${P_{ij}}^{pair}$	ST-TPI pressure of vessel pair ij; used to identify high-pressure vessel pairs.
Individual-ship components	${P_i}^{den}$, ${P_i}^{spa}$, ${P_i}^{conf}$, ${P_i}^{mot}$	Density, spatial-proximity, encounter-conflict, and motion-disorder pressure components of vessel i.
Individual-ship pressure	${P_i}^{ship}$	Comprehensive ST-TPI pressure of vessel i; used to identify dominant pressure vessels.
Regional pressure	${P_{mean}}^{reg}$, ${P_{95}}^{reg}$, ${P_{STTPI}}^{reg}$	Mean ship pressure, 95th-percentile ship pressure, and regional ST-TPI pressure.
Scene pressure and dominant objects	P_{scene}; $\arg\max_i {P_i}^{ship}$; $\arg\max_{i,j} {P_{ij}}^{pair}$	Overall scene pressure, dominant vessel, and dominant vessel pair; used to summarize scene state and trace main pressure sources.
Pressure levels	P_{scene} in [0, 100]	Low: $0 \leq$ P < 20; Low-medium: 20 <= P < 40; Medium-high: 40 <= P < 60; High: 60 <= P < 80; Very high: 80 <= P <= 100.

2.5.1. Ship-Pair Kinematic Variables and Pairwise Pressure

Ship-pair pressure is the basis of the ST-TPI-based multi-level traffic pressure evaluation. For each multi-ship traffic snapshot, all vessels in the snapshot were first paired to form candidate vessel pairs. For vessels i and j, their geographic positions were converted into a local planar coordinate system and expressed in nautical miles. Let $\mathbf{p}_i = [x_i, y_i]^T$ and $\mathbf{v}_i = [v_{x,i}, v_{y,i}]^T$ denote the local planar position and velocity vector of vessel i, respectively, where the velocity direction is determined by COG. The velocity vector was converted from knots to nautical miles per minute for TCPA and DCPA calculation, so that TCPA was obtained in minutes. The closing speed was further converted back to knots for calculating the closing-speed factor. The relative position, relative velocity, and current distance of the vessel pair i, j were defined as

$$\begin{cases} \mathbf{r}_{ij} & = \mathbf{p}_j - \mathbf{p}_i \\ \mathbf{v}_{ij} & = \mathbf{v}_j - \mathbf{v}_i \\ D_{ij} & = \| \mathbf{r}_{ij} \| \end{cases} \tag{28}$$

where $\mathbf{r}_{ij}$ denotes the relative position vector from vessel i to vessel j, $\mathbf{v}_{ij}$ denotes the relative velocity vector, and D_{ij} denotes the current distance between the two vessels.

Based on the relative motion relationship, the distance at the closest point of approach (DCPA) and the time to the closest point of approach (TCPA) were further calculated. When the relative velocity was nonzero, TCPA and DCPA were calculated as

$$\begin{cases} TCPA_{ij} & = -\frac{\mathbf{r}_{ij} \cdot \mathbf{v}_{ij}}{\|\mathbf{v}_{ij}\|^2} \\ DCPA_{ij} & = \| \mathbf{r}_{ij} + \mathbf{v}_{ij} \max\left(TCPA_{ij}, 0\right) \| \\ V_{c,ij} & = 60 \max\left(0, -\frac{\mathbf{r}_{ij} \cdot \mathbf{v}_{ij}}{D_{ij}}\right) \end{cases} \tag{29}$$

where $TCPA_{ij}$ denotes the time to the closest encounter state, $DCPA_{ij}$ denotes the minimum distance at the closest encounter state, and $V_{c,ij}$ denotes the closing speed in knots.

The pairwise spatial proximity pressure describes the pressure caused by the current spatial proximity between two vessels. If the inter-vessel distance is within the perception radius R_p, the spatial pressure decays exponentially with distance; otherwise, it is set to zero:

$$Q_{ij}^{spa} = \begin{cases} \exp\left[-\left(\frac{D_{ij}}{D_s}\right)^2\right], & D_{ij} \le R_p \\ 0, & D_{ij} > R_p \end{cases} \tag{30}$$

where D_s is the spatial safety scale and R_p is the vessel perception radius.

Furthermore, the pairwise encounter-conflict pressure jointly considers DCPA, TCPA, heading difference, and closing speed. It is defined as

$$C_{ij}^{conf} = \exp\left(-\frac{DCPA_{ij}}{D_0}\right)\exp\left(-\frac{TCPA_{ij}}{T_0}\right)F_{\theta,ij}F_{c,ij} \tag{31}$$

where D_0 is the DCPA decay scale, T_0 is the TCPA decay scale, $F_{\theta,ij}$ is the heading-angle pressure factor, and $F_{c,ij}$ is the closing-speed factor. The approaching condition is defined as $0 < TCPA_{ij} \le T_{max}$ and $D_{ij} \le R_p$. If the vessel pair does not satisfy this condition, $C_{ij}^{conf} = 0$. The closing-speed factor is defined as

$$F_{c,ij} = \min\left(1, \frac{V_{c,ij}}{C_0}\right) \tag{32}$$

where C_0 is the reference closing speed.

Finally, the pairwise spatial pressure and encounter-conflict pressure were combined to obtain the ship-pair pressure:

$$P_{ij}^{pair} = C_{max}\sqrt{w_{pair,spa}\left(Q_{ij}^{spa}\right)^2 + w_{pair,conf}\left(C_{ij}^{conf}\right)^2} \tag{33}$$

where $C_{max} = 100$ is the upper bound of the pressure index, and $w_{pair,spa}$ and $w_{pair,conf}$ are the weights of spatial pressure and conflict pressure, respectively. In this study, they were set to 0.35 and 0.65. A higher ship-pair pressure indicates that the vessel pair contributes more strongly to the local traffic pressure in the current or future snapshot.

2.5.2. Individual-Ship ST-TPI Pressure

After obtaining ship-pair pressures and pairwise kinematic relations, the traffic pressure experienced by each individual vessel was further evaluated. The individual-ship ST-TPI pressure consists of four components: local density pressure, spatial proximity pressure, encounter-conflict pressure, and motion-disorder pressure. These components are consistent with previous traffic-complexity and regional-risk studies, in which vessel density, proximity, encounter conflict, speed variation, and course variation are regarded as important descriptors of complex maritime traffic situations [38]. These components reflect the local traffic density around a vessel, the spatial proximity of neighboring vessels, the potential encounter conflict, and the inconsistency of local motion states, respectively.

For vessel i, its neighboring-vessel set within the perception radius is defined as

$$\mathcal{N}_i = \{j \mid D_{ij} \le R_p, j \ne i\} \tag{34}$$

where $\mathcal{N}_i$ denotes the set of neighboring vessels located within the perception radius R_p of vessel i. To avoid describing local traffic density only by the number of vessels, a distance-

weighted effective number of neighboring vessels was calculated, and the local density pressure was then defined as

$$\begin{cases} N_i^{eff} & = \sum_{j \in \mathcal{N}_i} \exp\left[-\left(\frac{D_{ij}}{R_p}\right)^2\right] \\ P_i^{den} & = 1 - \exp\left(-\frac{N_i^{eff}}{N_{ref}}\right) \end{cases} \tag{35}$$

where N_i^{eff} is the distance-weighted effective number of neighboring vessels, and N_{ref} is the reference effective vessel number. This component increases with the number of nearby vessels and is constrained within the range of $[0, 1]$ by the exponential form.

Based on the pairwise spatial pressure Q_{ij}^{spa} and encounter-conflict pressure C_{ij}^{conf} defined at the ship-pair level, the individual spatial proximity pressure and encounter-conflict pressure of vessel i were calculated as

$$\begin{cases} P_i^{spa} & = 1 - \prod_{j \in \mathcal{N}_i} \left(1 - Q_{ij}^{spa}\right) \\ P_i^{conf} & = 1 - \prod_{j \in \mathcal{N}_i} \left(1 - C_{ij}^{conf}\right) \end{cases} \tag{36}$$

The spatial proximity pressure P_i^{spa} increases when vessel i is involved in one or more high spatial-proximity pairs, while the encounter-conflict pressure P_i^{conf} reflects the potential encounter conflict caused by DCPA, TCPA, closing speed, and heading relations.

In addition to spatial proximity and encounter conflict, the local consistency of traffic motion was also considered. Course and speed variations have been used to describe maneuvering complexity and motion disorder in traffic-complexity assessment, especially in crossing or nonlinear waterways [15,38]. For vessel i and its neighboring vessels, the distance weight used for calculating motion disorder was defined as

$$w_{ij} = \begin{cases} 1, & j = i \\ \exp\left[-\left(\frac{D_{ij}}{R_p}\right)^2\right], & j \in \mathcal{N}_i \end{cases} \tag{37}$$

To avoid ambiguity in trigonometric expressions, the course angle was converted into radians as $\theta_j = COG_j \pi / 180$. The course-disorder pressure was then calculated according to the resultant length of the weighted course unit vectors within the neighborhood:

$$P_i^{course} = 1 - \frac{\sqrt{\left(\sum_{j \in \{i\} \cup \mathcal{N}_i} w_{ij} \sin\theta_j\right)^2 + \left(\sum_{j \in \{i\} \cup \mathcal{N}_i} w_{ij} \cos\theta_j\right)^2}}{\sum_{j \in \{i\} \cup \mathcal{N}_i} w_{ij}} \tag{38}$$

When vessels in the neighborhood have similar courses, the resultant vector length approaches the total weight, and P_i^{course} is small. When the courses are dispersed or crossing, P_i^{course} increases. The speed-disorder pressure was calculated using the weighted standard deviation of SOG within the neighborhood, and the motion-disorder pressure was then obtained by combining course disorder and speed disorder:

$$\begin{cases} P_i^{speed} & = \min\left(1, \frac{\sigma_{v,i}^w}{V_{std}}\right) \\ P_i^{mot} & = w_{course} P_i^{course} + w_{speed} P_i^{speed} \end{cases} \tag{39}$$

where $\sigma_{v,i}^{w}$ denotes the weighted standard deviation of SOG within the neighborhood of vessel i, and w_{course} and w_{speed} are the weights of course disorder and speed disorder, respectively. In this study, they were set to 0.70 and 0.30.

Finally, the four components were integrated to obtain the individual-ship ST-TPI pressure of vessel i:

$$P_i^{ship} = C_{max}\sqrt{w_{den}\left(P_i^{den}\right)^2 + w_{spa}\left(P_i^{spa}\right)^2 + w_{conf}\left(P_i^{conf}\right)^2 + w_{mot}\left(P_i^{mot}\right)^2} \tag{40}$$

where $C_{max} = 100$ is the upper bound of the pressure index, and w_{den}, w_{spa}, w_{conf}, and w_{mot} are the weights of the local density, spatial proximity, encounter-conflict, and motion-disorder pressure components, respectively. In this study, these four weights were set to 0.25, 0.20, 0.40, and 0.15. A higher individual-ship ST-TPI pressure indicates that the vessel is subject to greater comprehensive traffic pressure in the current or future snapshot.

2.5.3. Regional Traffic Pressure

After obtaining the individual-ship ST-TPI pressure, the traffic pressure was further aggregated at the regional level. Regional traffic pressure characterizes the overall pressure state of the water area in a current or future traffic snapshot. It reflects not only the average pressure experienced by all vessels but also the influence of high-pressure vessels and local extreme pressure on the regional traffic situation.

Assume that there are N vessels in a snapshot, and the individual-ship pressure of vessel i is denoted as P_i^{ship}. The basic regional pressure statistics were defined as

$$\begin{cases} P_{mean}^{reg} & = \frac{1}{N}\sum_{i=1}^{N} P_i^{ship} \\ P_{max}^{reg} & = \max_{1\le i\le N} P_i^{ship} \\ P_{95}^{reg} & = Q_{0.95}\left(P_1^{ship}, P_2^{ship}, \ldots, P_N^{ship}\right) \\ P_{sum}^{reg} & = \sum_{i=1}^{N} P_i^{ship} \\ P_{STTPI}^{reg} & = 0.6P_{mean}^{reg} + 0.4P_{95}^{reg} \end{cases} \tag{41}$$

where P_{mean}^{reg} denotes the mean individual-ship pressure in the region, representing the overall average pressure level; P_{max}^{reg} denotes the maximum individual-ship pressure; P_{95}^{reg} denotes the 95th percentile of individual-ship pressure, representing the upper pressure level in the region; P_{sum}^{reg} denotes the total individual-ship pressure; and P_{STTPI}^{reg} denotes the regional ST-TPI pressure index. In this study, the regional ST-TPI was calculated as a weighted combination of the mean pressure and the 95th percentile pressure, with weights of 0.6 and 0.4, respectively. This formulation reflects the overall average pressure while retaining the influence of high-pressure vessels that may otherwise be smoothed by the mean value.

In addition to the regional pressure statistics, the number of high-pressure vessels, the number of high-pressure vessel pairs, and the maximum pairwise pressure were also calculated to identify whether the regional traffic pressure was dominated by local high-risk objects. Let P_{ij}^{pair} denote the pairwise pressure of vessel pair i, j, $\mathcal{P}$ denote the candidate

vessel-pair set in the snapshot, and T_{high} denote the high-pressure threshold. The auxiliary regional indicators were defined as

$$\begin{cases} N_{ship}^{high} & = \sum_{i=1}^{N} \mathbf{1}\left(P_i^{ship} \geq T_{high}\right) \\ N_{pair}^{high} & = \sum_{(i,j)\in\mathcal{P}} \mathbf{1}\left(P_{ij}^{pair} \geq T_{high}\right) \\ P_{pair}^{max} & = \max_{(i,j)\in\mathcal{P}} P_{ij}^{pair} \end{cases} \tag{42}$$

where $\mathbf{1}(\cdot)$ is an indicator function that equals 1 when the condition is satisfied and 0 otherwise. N_{ship}^{high} denotes the number of high-pressure vessels, N_{pair}^{high} denotes the number of high-pressure vessel pairs, and P_{pair}^{max} denotes the maximum pairwise pressure in the region. In this study, the high-pressure threshold T_{high} was set to 60. These indicators help determine whether the regional pressure is caused by the overall dense traffic situation or is dominated by a few high-risk vessels and vessel pairs.

Regional traffic pressure serves as an intermediate level between individual-ship pressure and the overall scene pressure. It preserves the distribution characteristics of ship pressure within the region and provides regional-scale input for the subsequent calculation of the overall scene-pressure index. Through this level, local ship-pair conflicts and individual-ship pressure states can be further elevated to the regional traffic situation level for evaluation.

2.5.4. Overall Scene-Pressure Index

After obtaining ship-pair pressure, individual-ship pressure, and regional pressure, an overall scene-pressure index was further constructed to represent the comprehensive traffic pressure level of a current or future multi-ship traffic snapshot. Unlike regional pressure, which mainly reflects the distribution of individual-ship pressure, the overall scene pressure simultaneously considers the mean individual-ship pressure, the high-percentile individual-ship pressure, the regional ST-TPI, the maximum pairwise pressure, the ship-number pressure, and the high-pressure pair ratio. Therefore, it can reflect both the global traffic congestion level and local high-risk encounter relationships.

Assume that a snapshot contains N vessels and M candidate vessel pairs. The individual-ship pressure is denoted as P_i^{ship}, and the pairwise pressure is denoted as P_{ij}^{pair}. The mean individual-ship pressure, the 95th percentile individual-ship pressure, and the regional ST-TPI have been defined in Section 2.5.3. To further describe the pressure associated with the number of vessels and high-pressure vessel pairs, the following auxiliary terms were defined:

$$\begin{cases} R_{pair}^{high} & = \frac{1}{M} \sum_{(i,j)\in\mathcal{P}} \mathbf{1}\left(P_{ij}^{pair} \geq T_{high}\right) \\ P_{num} & = C_{max} \min\left(\frac{N}{N_0} \middle| 1\right) \\ P_{high} & = C_{max} R_{pair}^{high} \\ P_{pair}^{max} & = \max_{(i,j)\in\mathcal{P}} P_{ij}^{pair} \end{cases} \tag{43}$$

where R_{pair}^{high} denotes the ratio of high-pressure vessel pairs, T_{high} is the high-pressure threshold, and $\mathbf{1}(\cdot)$ is an indicator function. P_{num} denotes the ship-number pressure, N_0 is the reference number of vessels, P_{high} denotes the pressure term caused by the high-pressure pair ratio, and P_{pair}^{max} denotes the maximum pairwise pressure in the snapshot. If no valid vessel pair exists in the snapshot, both the high-pressure pair ratio and the maximum pairwise pressure are set to zero.

Based on these terms, the overall scene-pressure index was defined as

$$\begin{cases} P_{scene} \\ P_{scene}^{01} \end{cases} = \min\left\{C_{max}, \max\left[0, w_{mean}P_{mean}^{ship} + w_{95}P_{95}^{ship} + w_{reg}P_{STTPI}^{reg} + w_{pair,max}P_{pair}^{max} + w_{num}P_{num} + w_{high}P_{high}\right]\right\} \\ = \frac{P_{scene}}{C_{max}} \quad (44)$$

where P_{scene} denotes the overall scene pressure, and P_{scene}^{01} denotes the normalized scene pressure. P_{mean}^{ship} and P_{95}^{ship} are the mean and 95th percentile of individual-ship pressure, respectively; P_{STTPI}^{reg} is the regional ST-TPI pressure; P_{pair}^{max} is the maximum pairwise pressure; P_{num} is the ship-number pressure; and P_{high} is the pressure associated with the high-pressure pair ratio. w_{mean}, w_{95}, w_{reg}, $w_{pair,max}$, w_{num}, and w_{high} are the weights of the corresponding components. To ensure that the overall scene pressure remains within $[0, C_{max}]$, the weighted result was constrained by lower and upper bounds. In the implementation, these scene-pressure weights were normalized before aggregation to keep the overall scene pressure within a consistent scale.

To facilitate the interpretation and visualization of the overall scene pressure, the scene pressure was further divided into five pressure levels according to four thresholds, namely 20, 40, 60, and 80. The pressure-level classification used in this study is summarized in Table 7.

Table 7. Classification of overall scene-pressure levels.

Scene-Pressure Range	Pressure Level	Interpretation
$P_{scene} < 20$	Low	The traffic situation is generally safe, with weak interaction pressure.
$20 \leq P_{scene} < 40$	Low-medium	Mild traffic pressure exists, but no obvious high-risk interaction dominates.
$40 \leq P_{scene} < 60$	Medium-high	Noticeable traffic pressure exists, and some vessels or pairs require attention.
$60 \leq P_{scene} < 80$	High	Strong traffic pressure exists, usually associated with high-risk vessels or pairs.
$P_{scene} \geq 80$	Very high	The traffic situation is highly compressed or conflict-prone.

Note: Background colors are used to visually distinguish the five scene-pressure levels.

In addition, the dominant pressure vessel and dominant pressure pair were recorded for each snapshot. The dominant vessel was identified as the vessel with the maximum individual-ship pressure, while the dominant pair was identified as the vessel pair with the maximum pairwise pressure. Through the overall scene-pressure index, local ship-pair conflict, individual-ship pressure, regional pressure, and overall traffic congestion can be integrated into a unified pressure scale, providing the basis for the pressure-evolution curves and future pressure snapshot analysis in Section 3.

2.5.5. Temporal Pressure Series for Predictive Assessment

After completing the ST-TPI-based multi-level pressure evaluation for a single multi-ship traffic snapshot, the evaluation process was further extended to the current snapshot and future multi-step prediction snapshots to construct a temporal pressure series for predictive assessment. This time series describes the evolution of multi-ship traffic pressure over the prediction horizon and provides the basis for the pressure-evolution curves and representative pressure snapshot analysis in Section 3.

Let t_0 denote the current snapshot time, Δt denote the prediction time interval, and H denote the number of future prediction steps. Based on the future multi-ship traffic

snapshot sequence generated in Section 2.4, the current and future snapshots can be expressed as

$$\begin{cases} \mathcal{S}^{(0)} & = \mathcal{S}_{t_0} \\ \mathcal{S}^{(h)} & = \mathcal{S}_{t_0+h\Delta t}, h = 1, 2, \ldots, H \end{cases} \tag{45}$$

where $\mathcal{S}^{(0)}$ denotes the current multi-ship traffic snapshot, and $\mathcal{S}^{(h)}$ denotes the multi-ship traffic snapshot at the h-th future prediction step. For each snapshot, ship-pair pressure, individual-ship pressure, regional pressure, and overall scene pressure were calculated sequentially according to the procedures defined in Sections 2.5.1–2.5.4. This process can be uniformly expressed as

$$\begin{cases} \mathcal{P}_h^{pair}, \mathcal{P}_h^{ship}, P_h^{reg} & = \Phi_{STTPI}\left(\mathcal{S}^{(h)}\right) \\ P_h^{scene} & = \Psi\left(\mathcal{P}_h^{pair}, \mathcal{P}_h^{ship}, P_h^{reg}\right) \end{cases} \tag{46}$$

where $\Phi_{STTPI}(\cdot)$ denotes the process of calculating ship-pair, individual-ship, and regional pressure for a snapshot; $\Psi(\cdot)$ denotes the overall scene-pressure aggregation function; and $\mathcal{P}_h^{pair}$, $\mathcal{P}_h^{ship}$, P_h^{reg}, and P_h^{scene} denote the ship-pair pressure set, individual-ship pressure set, regional pressure, and overall scene pressure corresponding to the h-th snapshot, respectively.

Accordingly, the overall scene-pressure series and regional pressure series over the prediction horizon can be expressed as

$$\begin{cases} \mathbf{P}^{scene} & = \left[P_0^{scene}, P_1^{scene}, \ldots, P_H^{scene}\right] \\ \mathbf{P}^{reg} & = \left[P_0^{reg}, P_1^{reg}, \ldots, P_H^{reg}\right] \end{cases} \tag{47}$$

where P_0^{scene} and P_0^{reg} represent the overall scene pressure and regional pressure of the current snapshot, respectively, while P_h^{scene} and P_h^{reg} represent the pressure values of the h-th future snapshot. This temporal pressure series can be used to analyze the increasing, decreasing, or fluctuating trend of future multi-ship traffic pressure, and to identify the peak-pressure moment and the dominant pressure stage.

In the implementation, the current snapshot and future snapshots were input into the ST-TPI pressure calculation functions to generate the current pressure result and the pressure results of all future prediction steps. These outputs were further organized into regional pressure and overall scene-pressure time tables. The resulting temporal pressure series directly supports the pressure-evolution curves, pressure-level variation analysis, and pressure snapshot visualization in Section 3. For each selected prediction time, the corresponding ship-level pressure distribution and overall scene pressure were used to generate the pressure snapshots and temporal pressure curves.

2.5.6. Sensitivity Analysis of ST-TPI Parameters and Thresholds

To examine whether the ST-TPI results were overly dependent on a particular parameter setting, a sensitivity analysis was conducted for the main weights, scale parameters, and pressure-level thresholds. The tested parameter groups included the individual-ship component weights, ship-pair pressure weights, motion-disorder weights, scene-pressure aggregation weights, physical scale parameters, and pressure-level thresholds. For most weights and scale parameters, each parameter was perturbed by ±20% while the corresponding weight group was normalized in the same way as in the implementation. For the pressure-level thresholds, the four thresholds were jointly scaled by ±10% and ±20%.

The robustness of ST-TPI was evaluated using four metrics. First, the mean and maximum absolute changes in scene pressure were calculated to measure the numerical sensitivity of the overall scene-pressure value. Second, Spearman's rank correlation coef-

ficient was used to compare the ship-pair pressure rankings before and after parameter perturbation. Third, the overlap ratio of the top-5 high-pressure vessel pairs was calculated to examine whether the main warning targets remained stable. Finally, the scene-level change rate was used to evaluate whether the categorical pressure level was affected by parameter perturbation.

2.5.7. Design of Prediction-Error Perturbation Analysis

To further examine how trajectory prediction uncertainty may affect the subsequent ST-TPI pressure assessment, a prediction-error perturbation analysis was designed. The original predicted multi-ship traffic snapshots were used as the baseline. Artificial position perturbations with different magnitudes were added only to the predicted vessel positions, while the historical AIS observations, model parameters, ST-TPI weights, physical scale parameters, and pressure-level thresholds were kept unchanged.

For each perturbation magnitude, the perturbed vessel positions were used to reconstruct the future multi-ship traffic snapshots. Pairwise kinematic relations, including inter-vessel distance, DCPA, TCPA, encounter relations, ship-pair pressure, individual-ship pressure, regional pressure, and overall scene pressure, were then recalculated according to the same ST-TPI procedure. The perturbed results were compared with the baseline results to quantify the propagation of position uncertainty into pressure-evaluation uncertainty.

The tested position perturbation magnitudes were 0 m, 25 m, 50 m, 100 m, and 150 m, where 0 m represents the baseline without position perturbation. For each perturbation magnitude, 50 Monte Carlo realizations were generated for each future multi-ship snapshot, and the ST-TPI results were recalculated after perturbing only the predicted vessel positions. The stability of the ST-TPI outputs was evaluated at the ship-pair, individual-ship, regional, and scene levels. The selected metrics included pair-ranking Spearman correlation, top-5 high-pressure pair overlap ratio, dominant vessel consistency, mean absolute change in regional pressure, mean absolute change in scene pressure, and pressure-level change rate. These metrics were used to examine whether prediction-position uncertainty affected the ranking of high-pressure vessel pairs, the identification of dominant pressure-contributing vessels, regional pressure magnitude, scene-pressure magnitude, and pressure-level classification.

3. Results

This section presents the experimental validation of the proposed LSTM–ST-TPI predictive traffic pressure assessment framework. First, the prediction performance of the LSTM-based short-term motion model is evaluated to verify the reliability of future ship-position estimation and subsequent multi-ship snapshot generation. Then, the proposed predictive ST-TPI assessment method is applied to five typical multi-ship traffic scenarios, including low-density traffic, dense but ordered traffic, crossing encounter, complex multi-ship interaction, and pressure-rising traffic scenarios. For each scenario, future traffic states are generated over a 30 min prediction horizon, and the evolution of scene pressure, mean ship pressure, maximum ship pressure, and representative pressure snapshots is analyzed. Finally, a real-world case study in the Laotieshan Channel is conducted to further examine the applicability of the proposed framework in a complex practical waterway. In addition, parameter sensitivity, prediction-error perturbation, and consistency analyses are conducted to examine the robustness and practical validity of the proposed ST-TPI results.

To make the validation logic of the proposed framework clearer, the experimental validation was organized into five aspects. First, the competitiveness and stability of the LSTM-based prediction module were examined using one-step prediction errors, multi-horizon rolling prediction errors, and comparison with representative baseline methods. Second, a preprocessing ablation study was conducted to quantify the effect of AIS cleaning, temporal resampling,

and continuous trajectory reconstruction on prediction performance. Third, the predictive ST-TPI framework was evaluated in five typical multi-ship scenarios and one real-waterway case to examine whether different pressure-evolution patterns could be identified. Fourth, the robustness of the ST-TPI model was tested through parameter sensitivity analysis and prediction-error perturbation analysis. Finally, the practical validity and statistical reliability of the ST-TPI results were further examined through consistency analysis with conventional DCPA/TCPA/CRI-based encounter-risk indicators. These validation steps jointly assess prediction accuracy, preprocessing necessity, parameter robustness, uncertainty propagation, and agreement with established maritime encounter-risk interpretation.

All experiments were implemented in MATLAB R2024a on a Lenovo laptop equipped with an Intel Core i9-12900H CPU, 16 GB RAM, and an NVIDIA GeForce RTX 3060 Laptop GPU with 6 GB dedicated video memory. The LSTM model was trained using the MATLAB Deep Learning Toolbox, with GPU acceleration enabled during neural network training. The same computational workflow was used for AIS data preprocessing, LSTM-based recursive prediction, future multi-ship traffic snapshot generation, and ST-TPI-based pressure calculation, ensuring consistency between the method implementation and the result analysis.

From the computational perspective, the LSTM model training is performed offline and is not required during real-time operation. During online or near-real-time use, the main computational tasks include AIS preprocessing, LSTM inference for each vessel, future multi-ship snapshot generation, pairwise encounter-relation extraction, and ST-TPI pressure calculation. For a traffic snapshot containing n vessels and a prediction horizon of H time steps, the recursive LSTM prediction cost increases approximately linearly with nH, whereas the pairwise encounter-relation extraction and ship-pair pressure calculation increase approximately with $Hn(n-1)/2$. Therefore, the main computational burden comes from pairwise relation calculation when the number of vessels becomes large.

In the present experiments, the typical scenarios contained 3–8 vessels and the Laotieshan Channel case contained 6 vessels. Under these scene sizes, the computational load is relatively small and suitable for offline analysis and near-real-time rolling assessment. For high-density VTS areas involving a much larger number of vessels, computational efficiency can be further improved by restricting pairwise calculations to vessels within the perception radius, dividing the monitored water area into subregions, and updating the pressure assessment only when new AIS observations are received. Therefore, the proposed framework has the potential to support near-real-time VTS applications, although operational deployment still requires further testing with live AIS streams and larger-scale traffic scenes.

3.1. Prediction Performance of the LSTM-Based Motion Model

To verify the reliability of subsequent future multi-ship traffic snapshot generation, the performance of the LSTM-based short-term vessel motion prediction model was first evaluated. The training, validation, and testing of the model were conducted using the AIS sliding-window samples described in Section 2.3.3. The LSTM model takes historical motion-state sequences as input and predicts the local-plane displacement increments at the next time step, which are then reconstructed into predicted geographic positions. The one-step prediction errors were evaluated using MAE, MPE, and RMSE, while the multi-horizon rolling prediction errors were further evaluated using MAE, ADE, FDE, and RMSE, as defined in Section 2.3.4. All position errors were calculated in the local planar coordinate system, with the unit of meters. The purpose of this evaluation is not only to examine the one-step position prediction accuracy, but also to confirm whether the predicted results can provide reliable motion-state inputs for subsequent future multi-ship traffic snapshot generation and ST-TPI-based pressure assessment.

As shown in Table 8, the prediction errors on the validation and testing subsets were relatively close. On the testing subset, the MAE, MPE, and RMSE were 14.812 m, 23.379 m, and 39.039 m, respectively. No obvious discrepancy was observed between the validation and testing results, indicating that the model maintained relatively stable prediction performance on unseen trajectory samples and did not show evident overfitting.

Table 8. One-step prediction accuracy of the LSTM-based short-term motion model.

Dataset	MAE (m)	MPE (m)	RMSE (m)
Validation	12.655	19.934	34.087
Testing	14.812	23.379	39.039

To explicitly quantify the influence of AIS preprocessing on trajectory prediction performance, a preprocessing ablation study was conducted. The complete preprocessing pipeline was compared with a raw-AIS direct-training setting. The complete pipeline includes abnormal-record removal, speed-jump filtering, 1 min temporal resampling, sine–cosine transformation of angular variables, and continuous trajectory reconstruction using the 5 min gap threshold. In contrast, the raw-AIS setting retains only basic field validity checking and duplicate removal. Therefore, this comparison directly evaluates whether the full preprocessing procedure is necessary for reliable short-term trajectory prediction.

As shown in Figure 6, direct training using raw AIS records led to substantially larger prediction errors, whereas the proposed preprocessing pipeline greatly improved prediction accuracy. Compared with the raw-AIS direct-training setting, the complete preprocessing pipeline reduced the test MAE from 344.64 m to 14.02 m, ADE from 568.01 m to 22.08 m, FDE from 302.18 m to 13.00 m, and RMSE from 3394.66 m to 36.05 m. These results indicate that AIS cleaning, temporal regularization, and continuous trajectory reconstruction are necessary for obtaining stable and reliable LSTM-based short-term vessel motion prediction results.

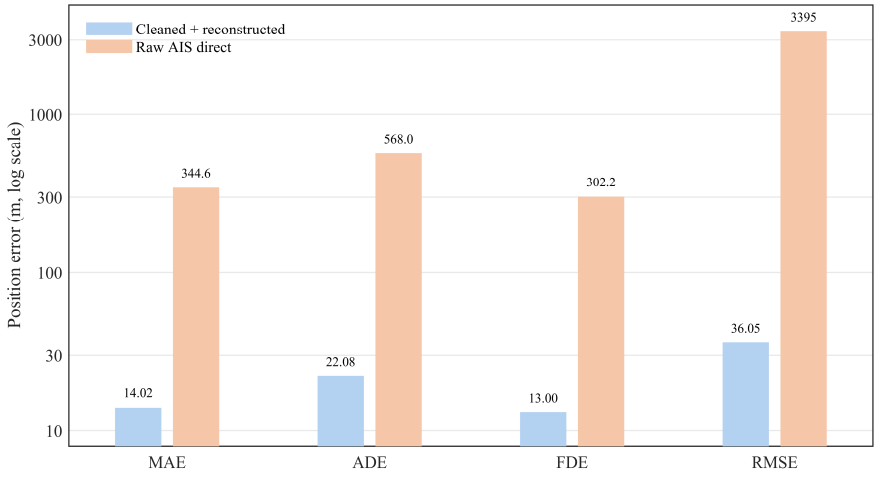


Figure 6. Preprocessing ablation study: comparison between raw-AIS direct training and the complete AIS preprocessing pipeline.

To further evaluate the competitiveness of the LSTM-based prediction module, a baseline comparison was conducted using several representative short-term motion prediction methods. The compared methods included two constant-velocity baselines, a Kalman filtering model, and a GRU network. The constant-velocity baselines were included because many cargo-vessel trajectories in the dataset exhibit nearly steady short-term motion, making them strong references for one-step position prediction. The Kalman filtering

model represents a classical state-estimation approach, while the GRU network was selected as another recurrent neural-network predictor for comparison with the LSTM model. CV-LastDisp used the most recent observed displacement between two consecutive AIS points as the predicted next-step displacement. CV-SOG/COG predicted the next position according to the current speed over ground and course over ground after converting speed from knots to meters per minute. The GRU model used the same input features, training-validation-testing partition, and error metrics as the LSTM model, with the recurrent unit replaced by a GRU unit.

The baseline comparison results are shown in Figure 7. The constant-velocity baselines achieved the lowest FDE values in this observation-updated rolling evaluation, which is reasonable for smooth cargo-vessel cruising trajectories. The GRU and LSTM models showed slightly larger but stable errors, while the Kalman filtering model produced larger errors under the present configuration. The relatively strong performance of the constant-velocity baselines is reasonable because short-term cargo-vessel motion in the training data is often close to uniform motion. This also indicates that simple kinematic assumptions can be effective for stable cargo-vessel trajectories over a short prediction interval.

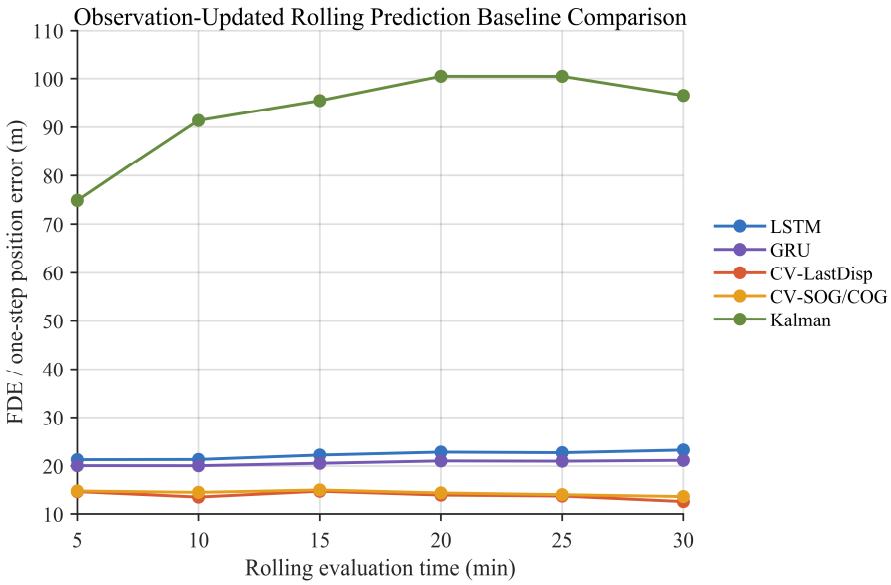


Figure 7. FDE comparison of different short-term prediction methods under observation-updated rolling evaluation.

To make the competitiveness of the prediction module clearer, the comparison in Figure 7 was designed as a baseline and representative prediction-method comparison. The two constant-velocity methods represent simple kinematic baselines, Kalman filtering represents a classical state-estimation baseline, and GRU represents a recurrent neural-network predictor comparable to LSTM. Therefore, the comparison covers both standard motion baselines and a representative learning-based trajectory prediction method. Although the constant-velocity baselines achieved lower FDE values in the observation-updated rolling evaluation, this result is reasonable for smooth cargo-vessel cruising trajectories that are close to uniform motion over short time intervals. In this study, the LSTM model is retained not because it outperforms all possible predictors, but because it provides a stable, reproducible, data-driven, and replaceable prediction module for future multi-ship snapshot generation and ST-TPI pressure assessment. More advanced predictors can be incorporated into the same framework in future applications without changing the subsequent future-snapshot generation and ST-TPI pressure-assessment procedure.

To further investigate the forecasting stability of the LSTM-based motion prediction model over various future horizons, the multi-horizon rolling prediction error evaluation was undertaken. Prediction horizons for this experiment were set at 5, 10, 15, 20, 25 and 30 min, respectively. Errors were evaluated using 3000 trajectory samples for each prediction horizon. In the multi-horizon rolling prediction evaluation, the errors are computed in the local planar coordinate system using MAE, ADE, FDE and RMSE, as shown in Table 9. The variation trends of these four metrics with the prediction horizon are further depicted in Figure 8.

Table 9. LSTM prediction errors under different observation-updated rolling evaluation horizons.

Prediction Horizon (min)	MAE (m)	ADE (m)	FDE (m)	RMSE (m)
5	14.017	21.589	22.060	40.721
10	14.225	21.520	22.327	40.590
15	14.445	21.675	22.702	39.964
20	14.755	21.913	23.286	39.684
25	14.812	22.207	23.435	37.731
30	15.308	22.548	24.130	38.681

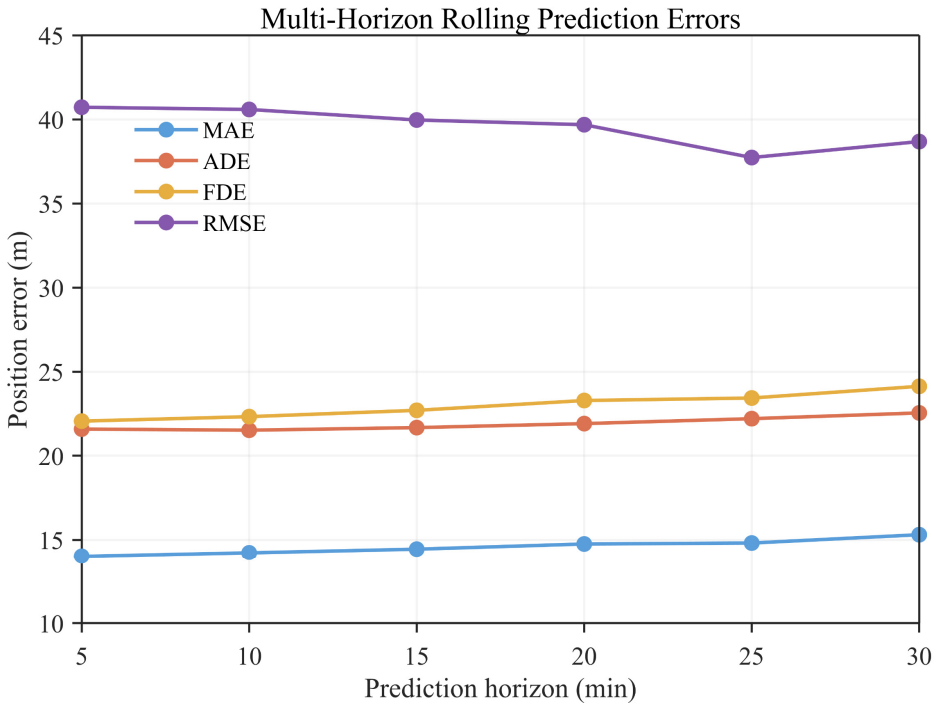


Figure 8. Variation in LSTM prediction errors under different observation-updated rolling evaluation horizons.

It should be noted that this multi-horizon error evaluation was conducted under an observation-updated rolling protocol. For each prediction horizon, the input window was reconstructed using the latest available AIS observations, rather than using a purely open-loop prediction starting only from the initial snapshot.

As shown in Table 9, the LSTM model maintained relatively stable prediction performance under the observation-updated rolling evaluation. The MAE increased slightly from 14.017 m at the 5 min horizon to 15.308 m at the 30 min horizon. Similarly, ADE increased from 21.589 m to 22.548 m, while FDE increased from 22.060 m to 24.130 m. This moderate variation is mainly because the historical input window was updated using the latest available AIS observations at each rolling evaluation horizon. Therefore, the

results in Table 9 should be interpreted as rolling prediction stability under continuous AIS observation updates, rather than as purely open-loop 30 min recursive prediction accuracy.

The RMSE remained within a relatively stable range across different prediction horizons, varying between 37.731 m and 40.721 m. This suggests that large local deviations did not increase substantially under the observation-updated rolling evaluation. The relatively stable RMSE is also consistent with the evaluation protocol described above, in which the historical input window was refreshed using the latest available AIS observations for each rolling assessment horizon.

Overall, the multi-horizon prediction-error evaluation demonstrates that the LSTM model can preserve stable short-term forecasting capability under the observation-updated rolling evaluation within the target 30 min assessment period. This provides an important basis for the subsequent generation of future multi-ship traffic snapshots. Since the ST-TPI assessment relies on the reconstructed future positions, relative distances, DCPA, TCPA, and encounter relationships among vessels, the stability of the prediction results supports the use of predicted vessel states as input data for predictive traffic pressure evaluation.

It should be noted that the rolling prediction evaluation in this section is mainly used to examine the forecasting stability of the LSTM model under different prediction horizons. In the subsequent multi-ship scenario analysis, the predicted states of all vessels at the same future time step are combined to form synchronized future traffic snapshots, and the pairwise encounter relationships are recalculated for ST-TPI-based pressure assessment. Therefore, the trajectory prediction results in this section serve as the motion-state foundation for the following pressure-evolution analysis.

To further examine the distribution characteristics of the prediction errors, a histogram of position prediction errors on the testing subset was plotted, as shown in Figure 9. Most prediction errors were concentrated within a relatively low range, although a small number of large-error samples still existed. This error distribution indicates that the LSTM model can effectively capture the short-term motion tendency of vessels, while relatively large deviations may still occur in some complex motion-changing or locally discontinuous trajectory samples.

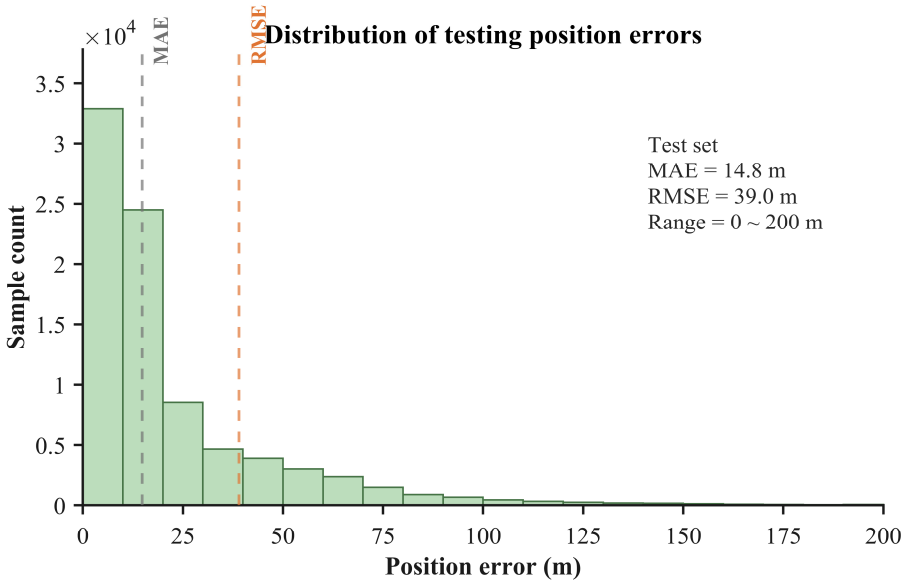


Figure 9. Distribution of position prediction errors on the testing subset.

In addition to the quantitative error evaluation, a representative multi-ship traffic segment was selected to visually examine whether the LSTM prediction results can preserve the basic spatial structure of a future traffic situation. A representative prediction result at the 15 min horizon is shown in Figure 10. The predicted trajectories generally extend

along the historical motion directions of the vessels, without obvious abrupt jumps or unrealistic discontinuities. This indicates that the model can capture the short-term motion inertia of vessels and provide reasonable predicted states for future multi-ship traffic snapshot generation.

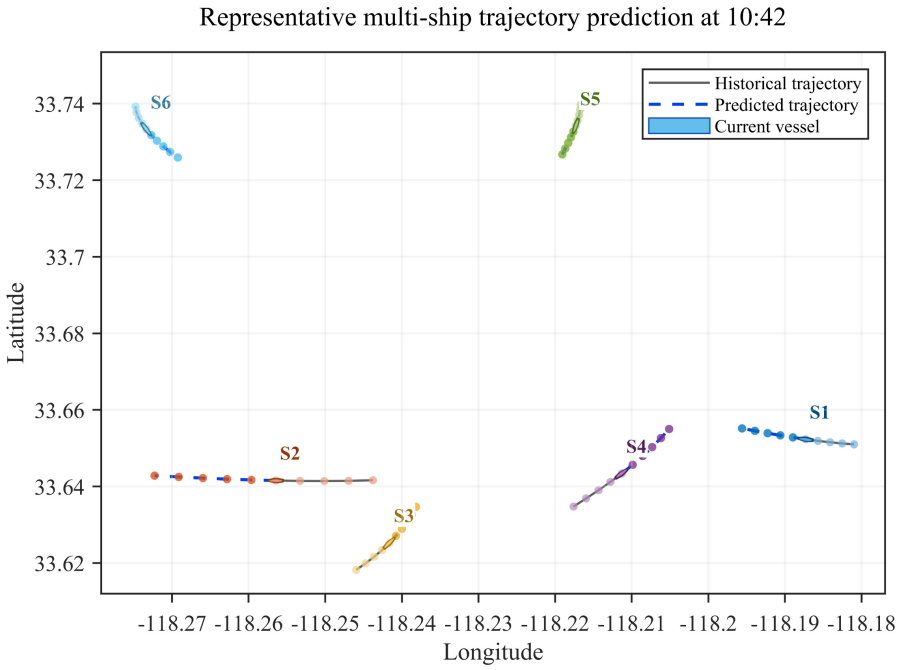


Figure 10. Visualization of representative multi-ship trajectory prediction at the 15 min horizon.

The purpose of this visualization is not to demonstrate exact point-by-point reproduction of future vessel positions, but to verify whether the relative spatial distribution and encounter structure among multiple vessels can be reasonably retained. This is important for the subsequent ST-TPI assessment, because traffic pressure calculation depends on inter-vessel distance, relative motion, DCPA, TCPA, and local spatial compression rather than isolated single-vessel position errors alone. Although prediction uncertainty may still increase when vessels perform turning, speed-changing, or local maneuvering behaviors, the result in Figure 10 suggests that the predicted trajectories preserve the main motion directions and geometric relationships of the multi-ship scene.

Based on these predicted states, future multi-ship traffic snapshots are generated at 5 min intervals within the 30 min prediction horizon. For each snapshot, pairwise encounter relationships are recalculated and then input into the ST-TPI model to obtain ship-level, ship-pair, regional, and overall scene pressure indicators. Therefore, the trajectory prediction results in this section provide the spatiotemporal basis for the subsequent pressure-evolution analysis.

Overall, the results in Section 3.1 indicate that the proposed LSTM model can provide stable short-term prediction results under the target rolling evaluation setting. The quantitative error metrics, rolling prediction analysis, error distribution, and representative multi-ship trajectory visualization jointly support the use of predicted vessel states for future multi-ship traffic snapshot generation. These snapshots provide the basis for pressure-level identification, peak-pressure detection, and dominant vessel and vessel-pair analysis in the following typical traffic scenarios.

3.2. Predictive ST-TPI Assessment in Typical Multi-Ship Scenarios

To evaluate the applicability of the proposed LSTM–ST-TPI framework under different traffic structures, five typical multi-ship scenarios were selected from the AIS dataset. These

cases include low-density traffic, dense but ordered flow, crossing encounter, complex multi-ship interaction, and pressure-rising traffic. They differ in vessel number, spatial distribution, motion consistency, local proximity, and encounter structure, and thus provide a comparative basis for examining the response of the proposed pressure assessment method.

For each scenario, the trained LSTM model was used to predict the future motion states of all vessels within a 30 min prediction horizon. Future multi-ship traffic snapshots were generated at 5 min intervals, and the ST-TPI model was then applied to each snapshot. The scene pressure, mean ship pressure, maximum ship pressure, and ship-level pressure distribution were analyzed to describe the temporal evolution and spatial concentration of traffic pressure.

The basic information of the five selected scenarios is summarized in Table 10. These cases are not intended to cover all possible traffic conditions, but to represent several common multi-ship structures that are relevant to maritime supervision.

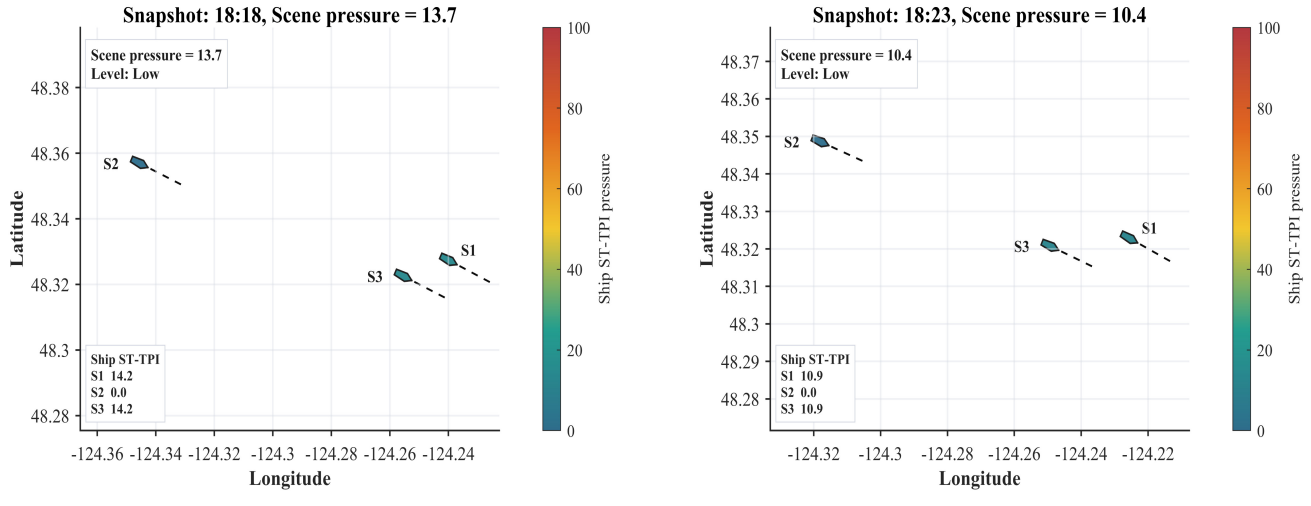
Table 10. Basic information on the five typical multi-ship scenarios.

Case	Traffic Type	Period	Number of Ships	Main Traffic Characteristic
A	Low-density traffic	18:13–18:43	3	Sparse distribution
B	Dense but ordered traffic	21:52–22:22	4	Compact but orderly flow
C	Crossing encounter	10:32–11:02	6	Local crossing interaction
D	Complex multi-ship interaction	06:12–06:42	8	Multiple overlapping interactions
E	Pressure-rising traffic	01:14–01:44	4	Late-stage pressure escalation

3.2.1. Case A: Low-Density Traffic Scenario

Case A was selected as the low-pressure reference case. During 18:13–18:43, only three vessels were involved in the scene, and their spatial separation remained relatively large within the prediction horizon. No clear close-range encounter or local convergence was observed. This case therefore provides a low-pressure reference for interpreting the pressure increases observed in the following scenarios.

As shown in Figure 11a–f, the ship-level ST-TPI values stayed at a low level in all future snapshots. The scene pressure was 13.7 at 5 min, decreased to 10.4 at 10 min, and then increased slightly to 16.4 at 30 min. These changes were small and did not alter the pressure level of the scene. Throughout the 30 min prediction horizon, the overall scene pressure remained below the Low-medium threshold, and no dominant pressure vessel or local pressure concentration appeared.



(**a**) (**b**)

Figure 11. *Cont.*

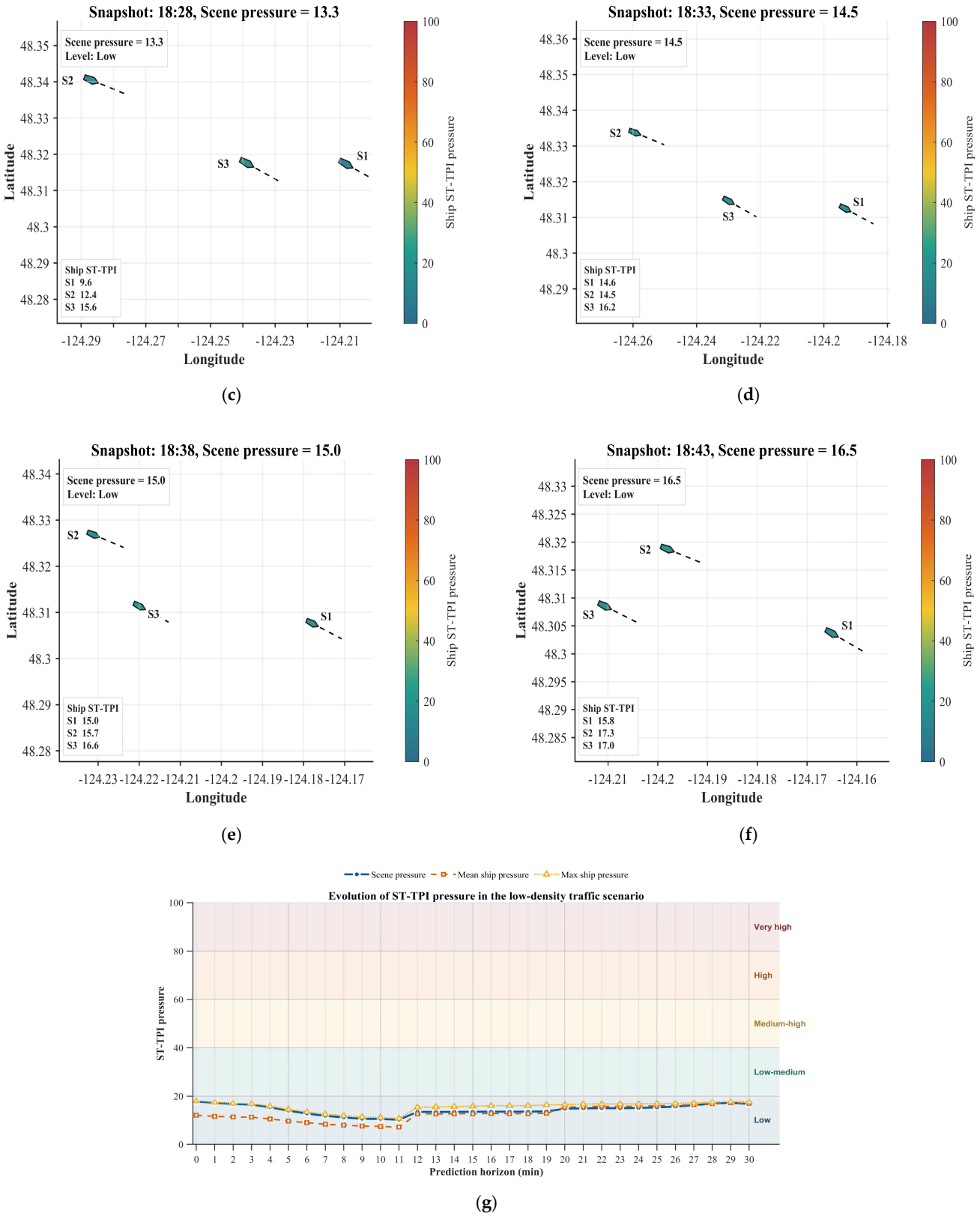


Figure 11. Predictive ST-TPI assessment results in the low-density traffic scenario. (**a**) A 5 min pressure snapshot; (**b**) 10 min pressure snapshot; (**c**) 15 min pressure snapshot; (**d**) 20 min pressure snapshot; (**e**) 25 min pressure snapshot; (**f**) 30 min pressure snapshot; (**g**) pressure-evolution curve.

The pressure curve in Figure 11g is consistent with the snapshot results. Scene pressure, mean ship pressure, and maximum ship pressure all remained within the Low level, with no sharp peak or sustained upward trend. In other words, the low pressure was not caused

only by the small number of vessels, but more importantly by the absence of close-range interaction. This reference case provides a clear contrast for the subsequent dense, crossing, complex, and pressure-rising scenarios.

3.2.2. Case B: Dense but Ordered Traffic Scenario

Case B was selected to represent a compact but relatively orderly traffic flow. During 21:52–22:22, four vessels were present in the scene. Compared with Case A, the vessels were closer to each other, but their motion directions were still relatively consistent. This case is therefore useful for examining a common supervisory situation: traffic may become locally compressed without immediately developing into a strongly disordered encounter.

As shown in Figure 12a–f, the scene pressure increased during the first half of the prediction horizon. It reached 33.5 at 5 min, 41.9 at 10 min, and further increased to 51.0 at 15 min, entering the Medium-high level. During this stage, vessels S2, S3, and S4 showed higher ship-level pressures, indicating that the pressure was mainly associated with a compact local formation rather than a single isolated vessel. The maximum ship pressure was also higher than the mean ship pressure, which suggests that the pressure was concentrated on part of the traffic flow.

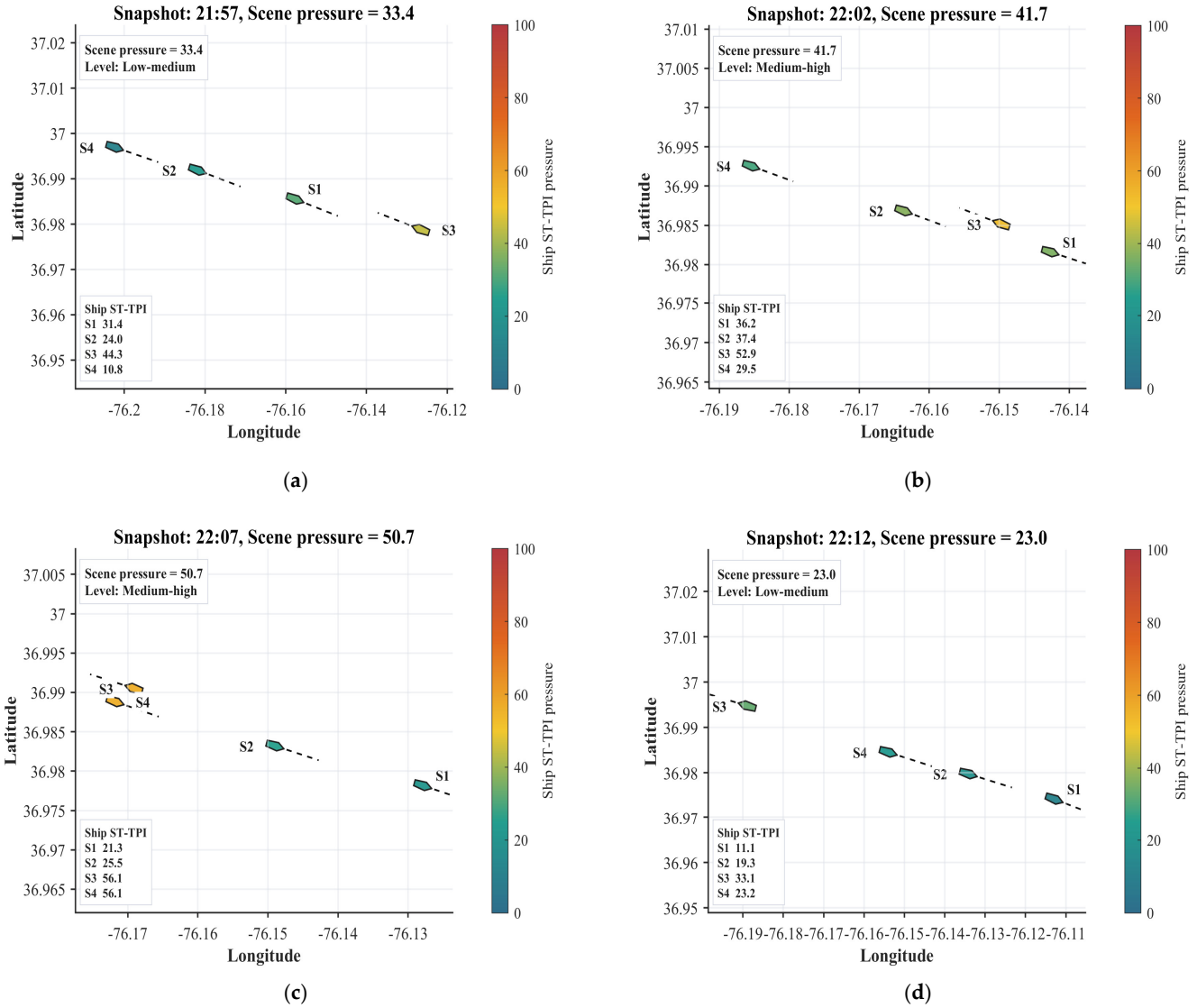


Figure 12. *Cont.*

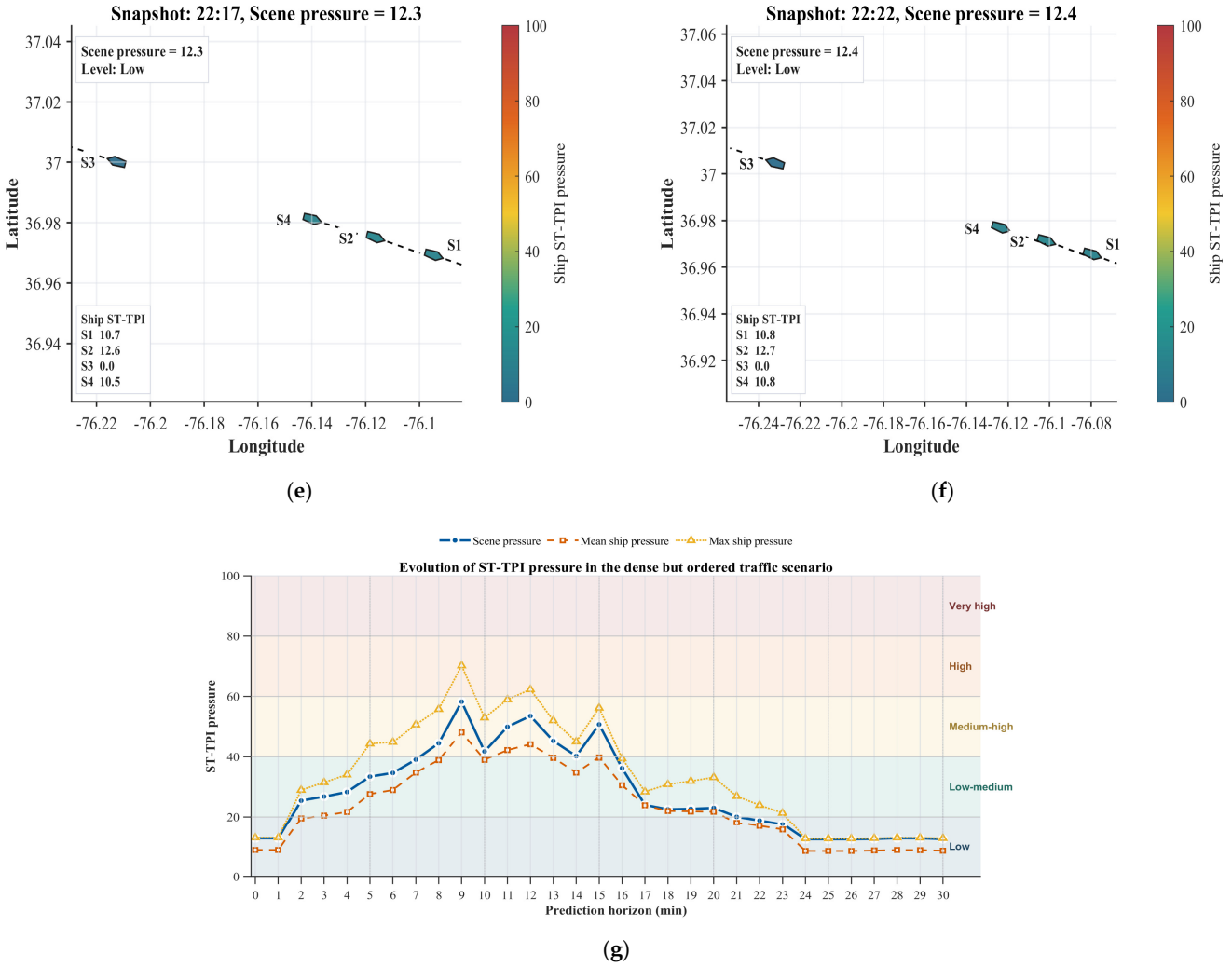


Figure 12. Predictive ST-TPI assessment results in the dense but ordered traffic scenario. (**a**) 5 min pressure snapshot; (**b**) 10 min pressure snapshot; (**c**) 15 min pressure snapshot; (**d**) 20 min pressure snapshot; (**e**) 25 min pressure snapshot; (**f**) 30 min pressure snapshot; (**g**) pressure-evolution curve.

After 15 min, the pressure was released quickly. The scene pressure decreased to 23.0 at 20 min and then returned to the Low level, with values of 12.3 and 12.4 at 25 and 30 min, respectively. The pressure curve in Figure 12g shows the same process of compression and release. The useful point in this case is the contrast between density and order: the compact vessel formation was sufficient to raise the pressure temporarily, but the relatively consistent motion pattern allowed the pressure to dissipate once the vessels passed through the compressed segment. This distinguishes Case B from both the sparse baseline in Case A and the later pressure escalation in Case E.

3.2.3. Case C: Crossing Encounter Scenario

Case C was selected to examine a crossing encounter situation involving six vessels. The prediction period lasted from 10:32 to 11:02. Unlike Case B, where pressure was mainly caused by short-term spatial compression, the main feature of this case is the gradual development of crossing geometry among several vessels. Therefore, this case helps determine whether the ST-TPI model can capture a delayed pressure increase before the scene becomes strongly compressed.

As shown in Figure 13a–f, the scene pressure remained relatively stable during the early and middle stages. The pressure values were 22.0, 22.1, 23.2, and 21.4 at 5, 10,

15, and 20 min, respectively, all within the Low-medium level. At this stage, although crossing tendencies were already present, the vessels had not yet formed a strong close-range interaction. The ship-level pressure distribution was also mild, and no dominant high-pressure vessel appeared.

In the later stage, the crossing structure became more influential. The scene pressure increased to 24.2 at 25 min and further rose to 32.4 at 30 min. This increase was not abrupt, but it showed that the local interaction was gradually becoming more organized around the crossing area. The pressure curve in Figure 13g shows the same delayed-growth pattern: the pressure remained almost unchanged in the first two-thirds of the prediction horizon and then increased near the end.

The value of Case C lies in this delay. A crossing situation does not necessarily produce high traffic pressure immediately; its pressure may become evident only after the relative geometry develops for a period of time. For supervision, this means that a moderate but steadily developing crossing structure should not be ignored simply because its early pressure value is not high. This case therefore differs from the temporary compression in Case B and provides an intermediate pattern between low-pressure interaction and stronger pressure formation.

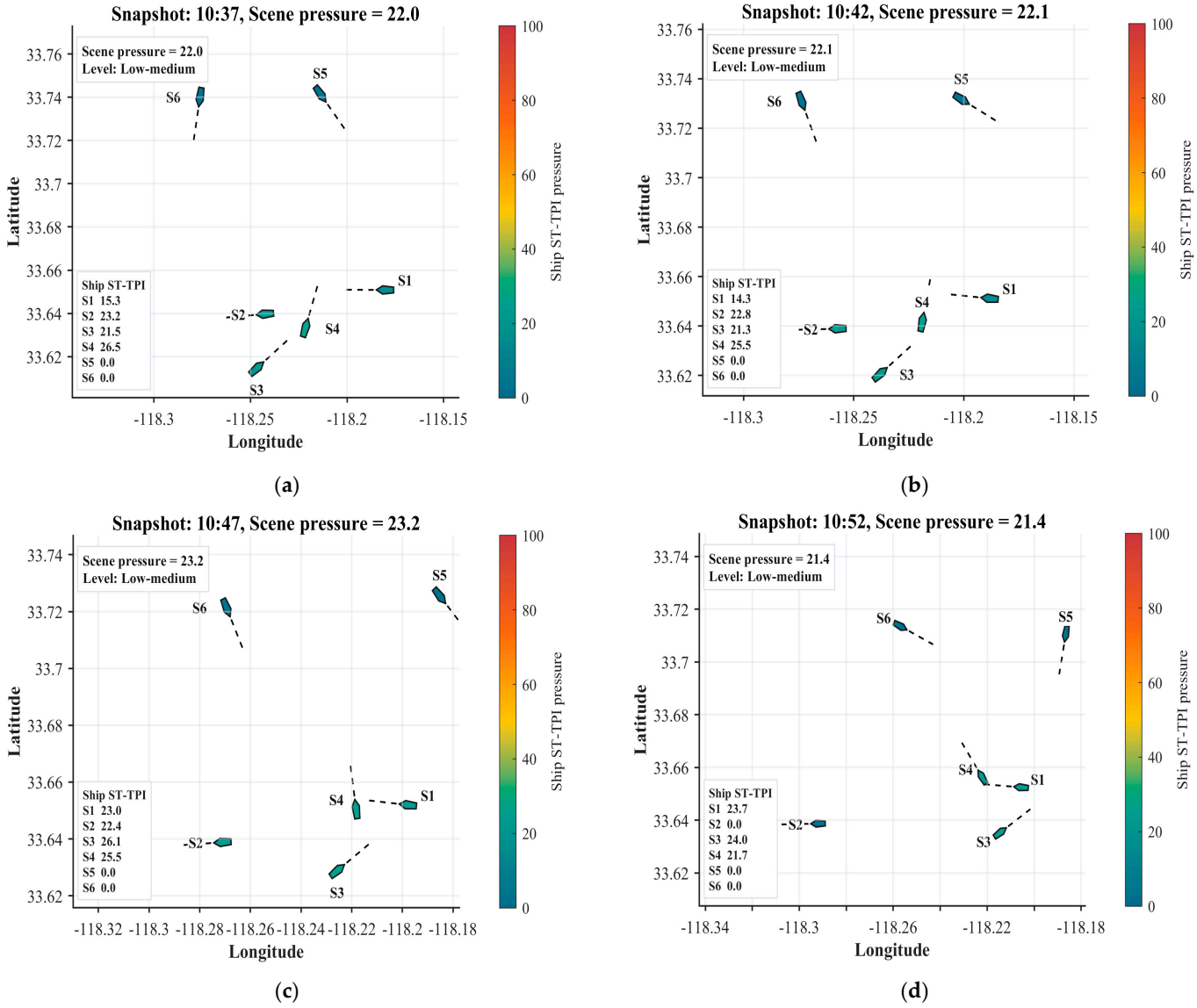
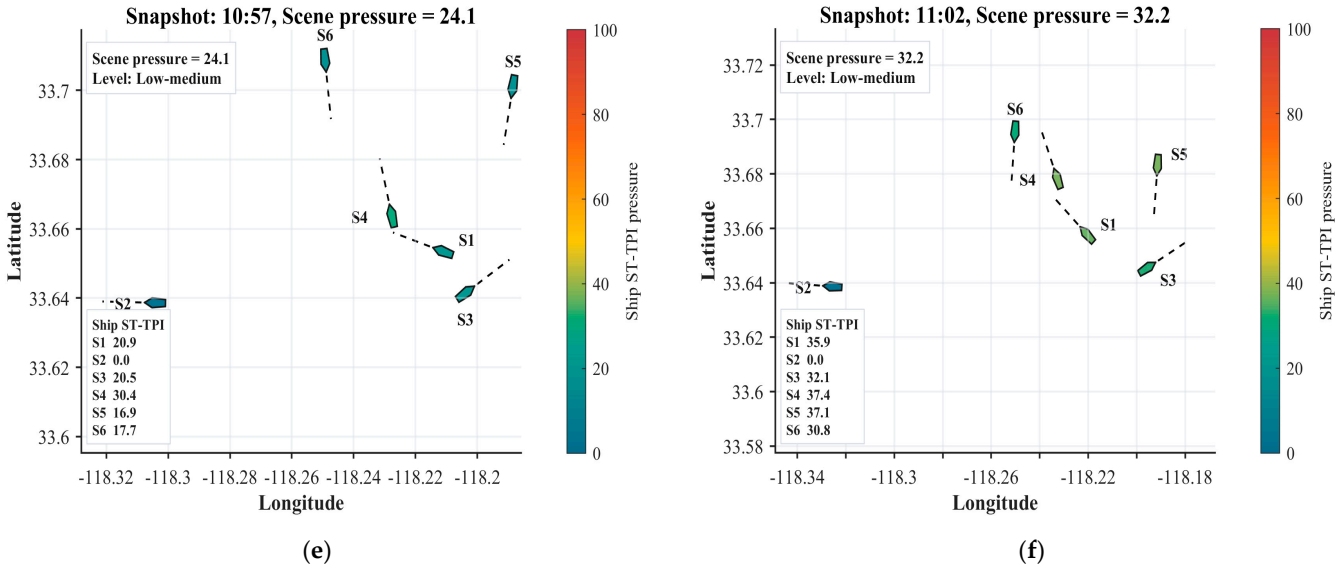
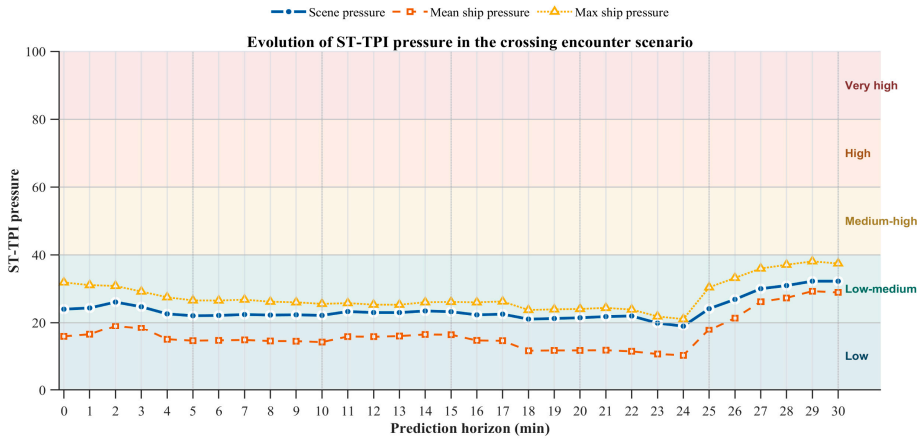


Figure 13. *Cont.*



(e) (f)



(g)

Figure 13. Predictive ST-TPI assessment results in the crossing encounter scenario. (**a**) A 5 min pressure snapshot; (**b**) 10 min pressure snapshot; (**c**) 15 min pressure snapshot; (**d**) 20 min pressure snapshot; (**e**) 25 min pressure snapshot; (**f**) 30 min pressure snapshot; (**g**) pressure-evolution curve.

3.2.4. Case D: Complex Multi-Ship Interaction Scenario

Case D was selected to examine a more complicated multi-ship traffic structure. During 06:12–06:42, eight vessels were involved in the scene, and several neighboring relations existed at the same time. Compared with Cases B and C, the traffic structure in this case was less regular: local proximity, overlapping vessel relations, and different motion directions appeared together. This case was therefore used to test whether the ST-TPI model can describe pressure variation when several local interactions coexist.

As shown in Figure 14a–f, the scene pressure was already at a relatively elevated level in the early stage. The pressure values were 56.1, 52.2, and 54.0 at 5, 10, and 15 min, respectively, all within the Medium-high level. The pressure was not produced by a single isolated vessel. Instead, it appeared along several adjacent vessels within the compact local structure. This suggests that the early pressure was mainly associated with the combined effect of vessel density, spatial proximity, and multiple overlapping encounter relations.

After 15 min, the traffic structure began to loosen, and the pressure decreased rapidly. The scene pressure dropped to 26.1 at 20 min and further decreased to 17.9 and 14.7 at 25 and 30 min, respectively. The pressure curve in Figure 14g shows the same transition from an elevated-pressure state to a low-pressure state. Although the maximum ship pressure remained higher than the mean ship pressure during the early stage, both values declined as the vessels separated.

Therefore, Case D is not a case of sustained pressure accumulation. Its value lies in showing that a complex and compact initial structure does not necessarily lead to persistent pressure. When the local vessel relations are gradually released, both the overall scene pressure and the local pressure concentration decrease. This case helps distinguish temporary traffic complexity from sustained pressure accumulation, and it provides a useful contrast with the pressure-rising process in Case E.

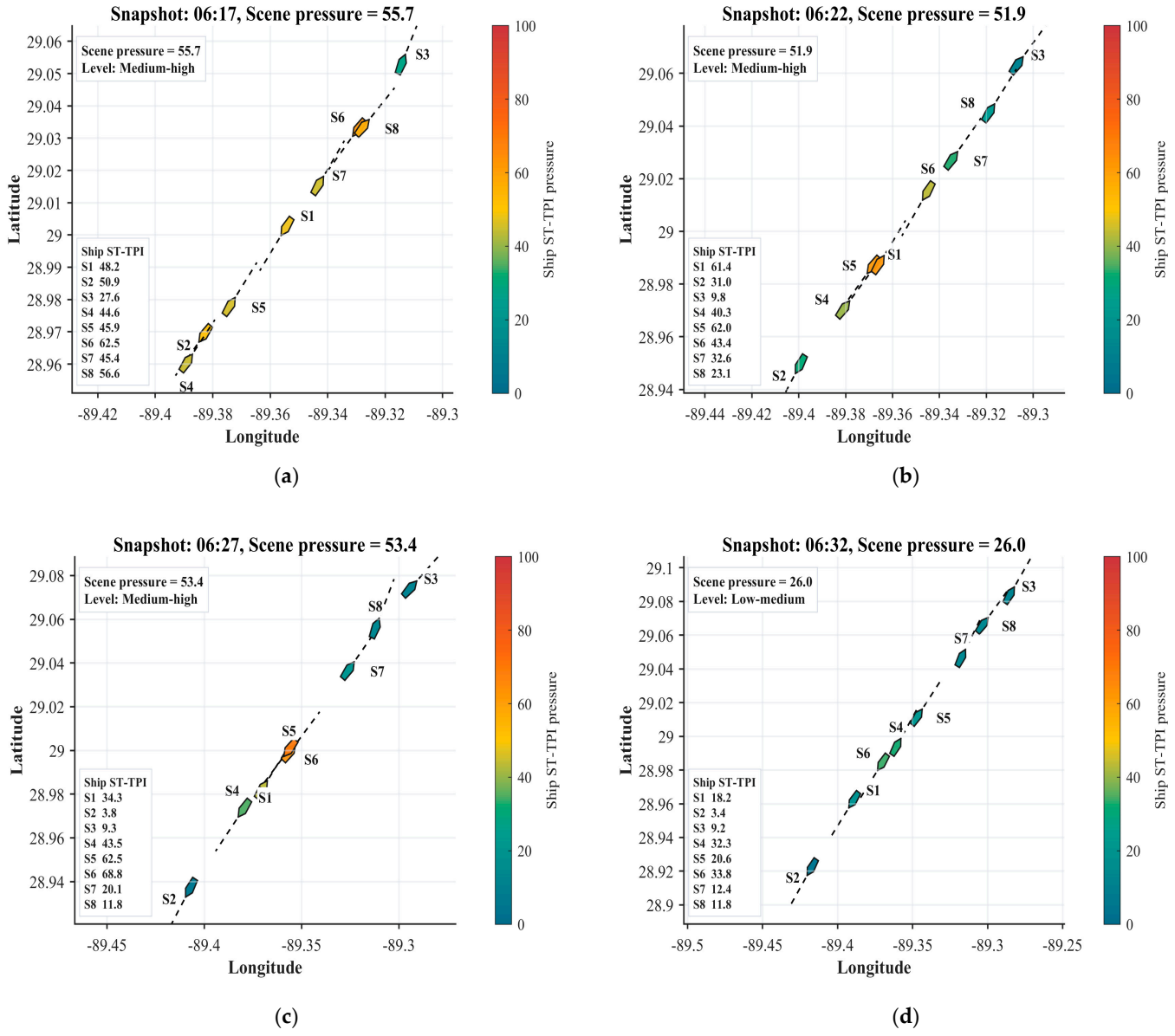


Figure 14. *Cont.*

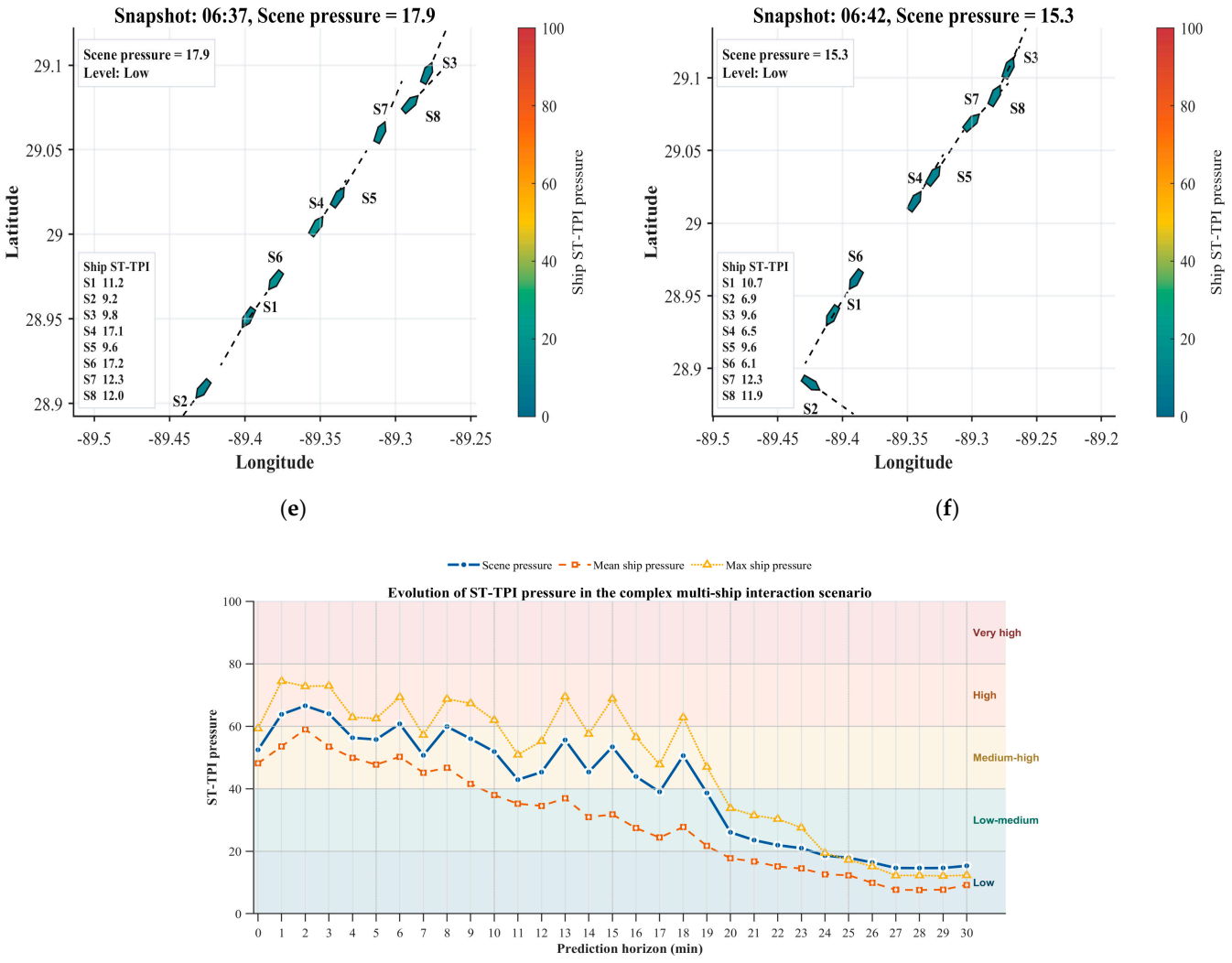


Figure 14. Predictive ST-TPI assessment results in the complex multi-ship interaction scenario. (**a**) A 5 min pressure snapshot; (**b**) 10 min pressure snapshot; (**c**) 15 min pressure snapshot; (**d**) 20 min pressure snapshot; (**e**) 25 min pressure snapshot; (**f**) 30 min pressure snapshot; (**g**) pressure-evolution curve.

3.2.5. Case E: Pressure-Rising Traffic Scenario

Case E was selected to represent a pressure-rising traffic scenario. The prediction period lasted from 01:14 to 01:44, and four vessels were involved in the scene. Unlike Case D, this case did not begin with an already compact and complex structure. At the beginning of the prediction horizon, the vessels were still relatively separated, and the interaction pressure was weak. Its value therefore lies in showing how a low-pressure traffic state can develop into a High-level pressure state within a short prediction horizon.

As shown in Figure 15a–c, the scene pressure remained low during the first 15 min. The pressure values were 9.6, 9.8, and 9.5 at 5, 10, and 15 min, respectively. The ship-level pressures were also low, indicating that no obvious local pressure source had yet formed. In this stage, the model response is consistent with the traffic structure: several vessels were present in the scene, but their relative positions did not yet create a compressed encounter situation.

After 20 min, the pressure began to increase. The scene pressure rose to 25.5, and vessels S2 and S4 showed higher ship-level pressures of 27.9 and 27.5, respectively. This indicates that the pressure increases initially emerged around a local encounter rather than across the whole scene. At 25 min, the scene pressure reached 60.3 and entered the High-level pressure state. The ship-level pressures of S2 and S4 reached 70.8 and 70.5, respectively, making them the main pressure-contributing vessels. At 30 min, the scene pressure further increased to 67.7, and the ship-level pressures of all four vessels exceeded 60. This indicates that the initially local pressure increase developed into a wider high-pressure state.

The pressure curve in Figure 15g makes this process clearer. Scene pressure, mean ship pressure, and maximum ship pressure remained stable in the early stage and then increased rapidly after approximately 20 min. From a supervisory perspective, the interval before 25 min is the most important part of this case. Before the scene pressure crossed the High-level threshold, the upward trend had already become evident. Case E therefore complements the previous scenarios by showing a complete pressure-rising process from a low initial state to a High-level pressure state. It also shows that the proposed framework can provide an advanced attention window before local interaction develops into scene-level pressure escalation.

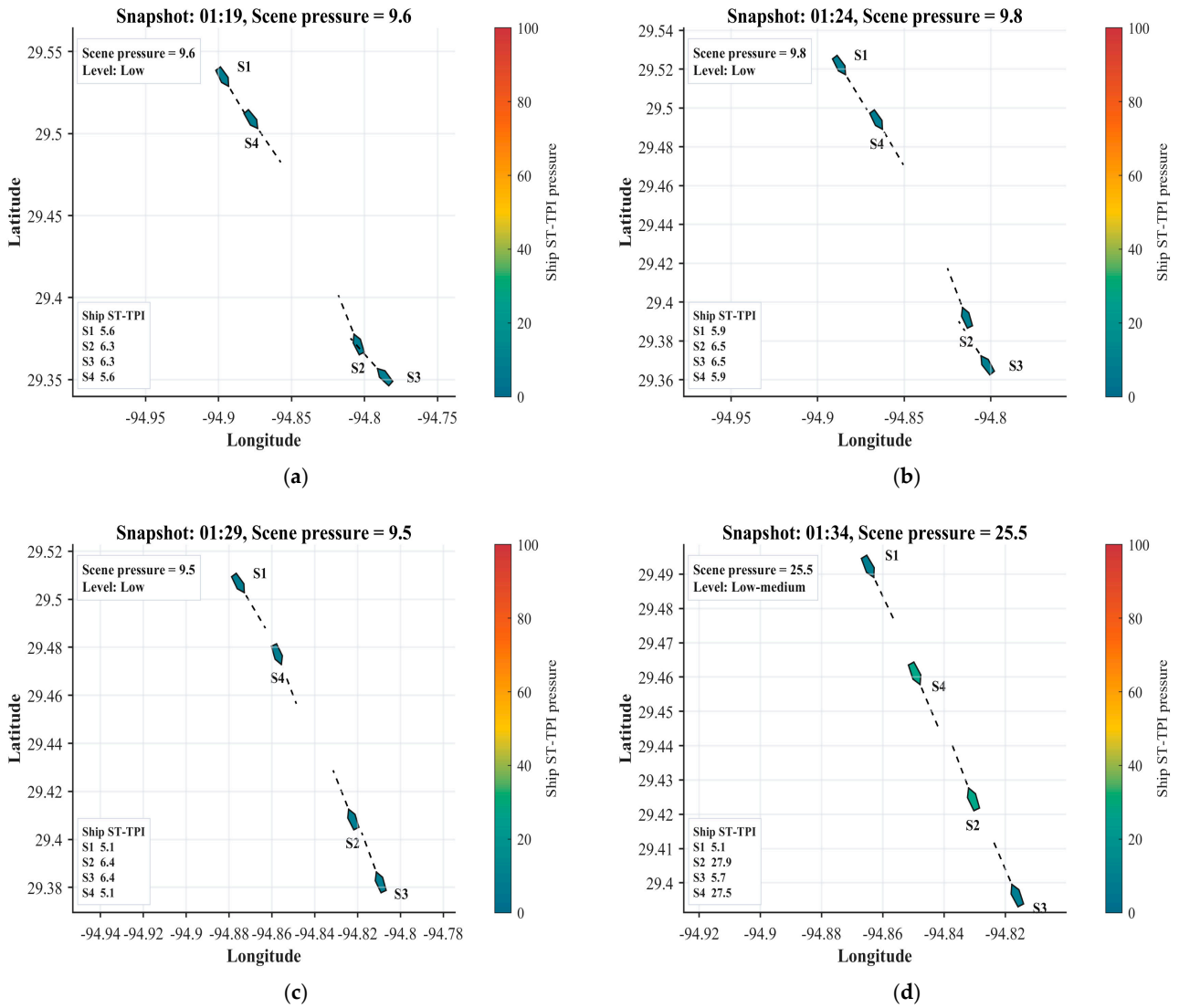


Figure 15. *Cont.*

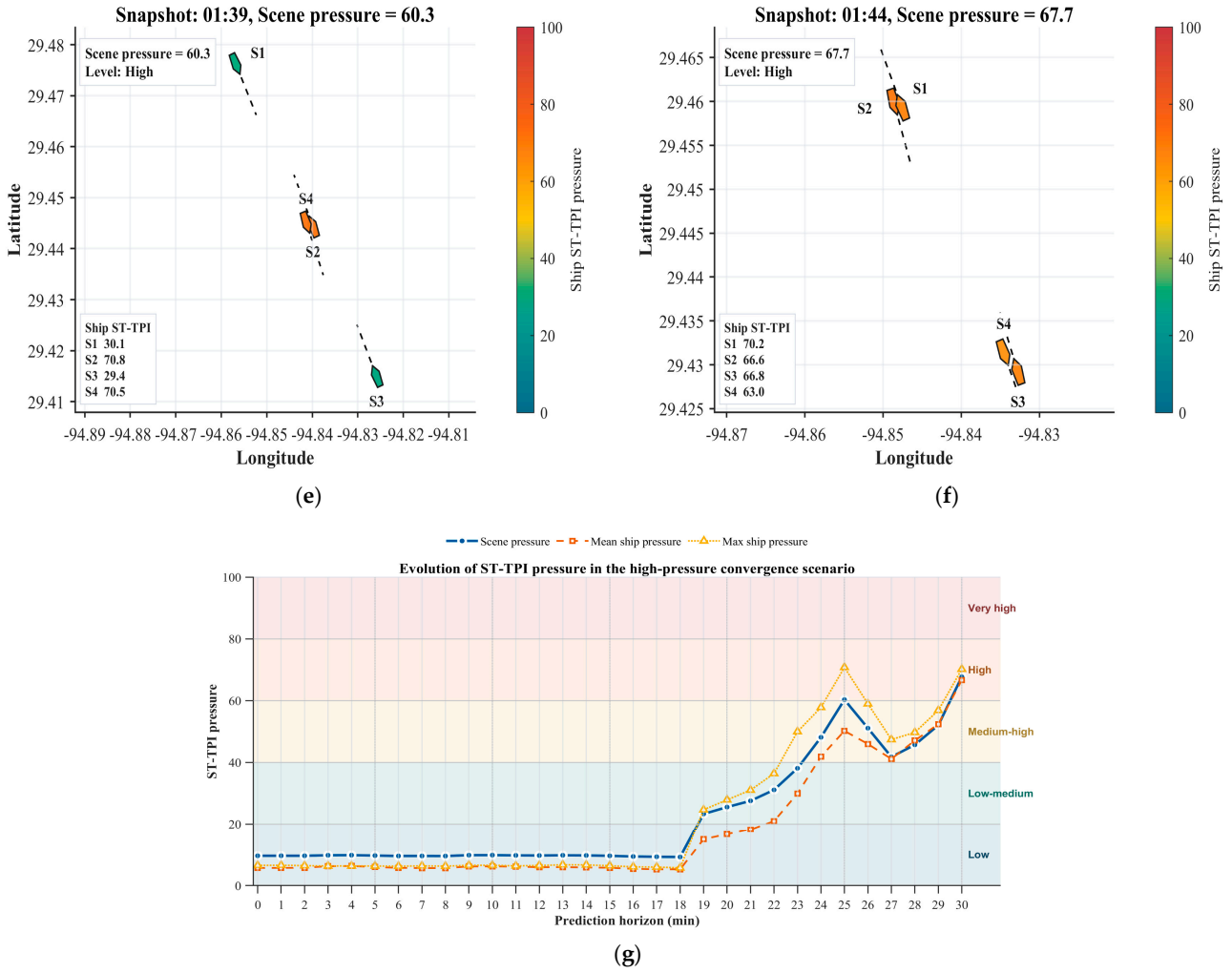


Figure 15. Predictive ST-TPI assessment results in the pressure-rising traffic scenario. (**a**) A 5 min pressure snapshot; (**b**) 10 min pressure snapshot; (**c**) 15 min pressure snapshot; (**d**) 20 min pressure snapshot; (**e**) 25 min pressure snapshot; (**f**) 30 min pressure snapshot; (**g**) pressure-evolution curve.

To further compare the pressure responses of the five scenarios, the main predictive ST-TPI results are summarized in Table 11.

Table 11. Summary of pressure evolution in typical scenarios.

Case	Pressure Pattern	Peak Pressure	Key Finding
A	Low → Low	16.4 at 30 min	Low-pressure baseline
B	Low-medium → Medium-high → Low	51.0 at 15 min	Compression and release
C	Low-medium → Low-medium	32.4 at 30 min	Delayed crossing pressure
D	Medium-high → Low	56.1 at 5 min	Complex interaction release
E	Low → Low-medium → High	67.7 at 30 min	High-level pressure formation

The comparison in Table 11 shows that the five cases do not simply differ in pressure magnitude; they represent different ways in which traffic pressure may appear. Case A remains low and serves as a sparse-traffic reference. Case B reaches a temporary Medium-high level and then releases, while Case C shows a delayed increase associated with crossing geometry. Case D starts from a relatively complex structure but later dissipates. Case E is the only case that develops into the High level, with the scene pressure increasing from a low state to 67.7 at 30 min. Taken together, these cases suggest that the proposed

framework can describe not only whether a future scene is pressured, but also how the pressure is formed, transferred, or released.

3.3. Case Study in the Western Precautionary Area of the Laotieshan Channel

To further examine how the proposed method behaves under practical AIS conditions, a real-waterway case was selected from the western precautionary area of the Laotieshan Channel. This area is a typical supervisory waterway where vessel routes may converge, diverge, or pass through the same local traffic area within a short time. Different from the representative scenarios discussed in Section 3.2, this case was not selected to reproduce a specific pressure pattern. It is used here as a practical case to check whether the predicted multi-ship states can be further converted into interpretable pressure information in an actual navigation environment.

The case involved six vessels observed near the western precautionary area. For each vessel, the historical AIS trajectory before the initial snapshot was first resampled at a 1 min interval and then used to construct the input window for the LSTM model. The vessel states were then recursively predicted over a 30 min horizon. Future multi-ship snapshots were extracted at 5 min intervals and evaluated using the ST-TPI model. The basic information of this real-waterway case is given in Table 12.

Table 12. Basic information of the Laotieshan Channel real-waterway case.

Item	Description
Study area	Western precautionary area of the Laotieshan Channel
Data source	Historical AIS records from a ship-tracking platform
Case period	29 May 2026 12:36–13:06
Prediction horizon	30 min
Snapshot interval	5 min
Number of vessels	6
Main traffic characteristic	Low and Low-medium pressure fluctuations with local pressure transfer
Purpose of the case	Real-waterway applicability validation

To aid the comprehension of the ship-level pressure distribution shown in Figure 16, the six AIS tracks used in this study were labeled S1–S6. The same labels are used for all pressure snapshots. Table 13 summarizes the associated vessel data.

Table 13. Vessel information used in the Laotieshan Channel real-waterway case.

Ship Label	Vessel Name	MMSI	Vessel Type
S1	BRAVEHEART I	636018158	Bulk carrier
S2	HAMIT K	352001306	Bulk carrier
S3	HONG TAI 829	414968000	Unspecified dry cargo ship
S4	QICHENG 6	413388410	Yacht
S5	RUNTONG 6	414301000	Bulk carrier
S6	XIANG MING YANG	412378000	Bulk carrier

Figure 16 shows the predicted pressure snapshots and the corresponding pressure-evolution curve. The scene pressure was 23.5 at 5 min and increased to 30.6 at 10 min, which was the highest value during the prediction horizon. After that, the pressure did not continue to accumulate. It decreased slightly to 28.7 at 15 min and 27.9 at 20 min, and then dropped to 22.2 at 25 min and 19.7 at 30 min. According to the pressure-level thresholds defined in Table 7, the scene mainly remained in the Low-medium level and returned to the Low level at the end of the prediction horizon.

This result is consistent with the visual traffic structure in the snapshots. The selected Laotieshan case did not develop into a high-pressure scene; instead, it showed a moderate pressure fluctuation followed by pressure release. Around the 10 min snapshot, several vessels in the local traffic area contributed more evidently to the pressure level, while the remaining vessels mainly formed the surrounding traffic background. As the relative positions of the vessels changed, the local pressure source also shifted, which can be observed from the variation in ship-level ST-TPI values across the snapshots.

The significance of this case is therefore different from that of the pressure-rising scenario in Section 3.2.5. The value of the Laotieshan case is not that it reaches an extreme pressure level, but that it shows how the framework can be used in a real supervisory waterway. Even under a Low and Low-medium pressure condition, the method still provides useful information, including the pressure peak, pressure release process, and local pressure-contributing vessels. This indicates that the LSTM–ST-TPI framework can support practical traffic monitoring not only by warning against high-pressure situations, but also by describing moderate pressure variation and its temporal migration in real AIS-based traffic scenes.

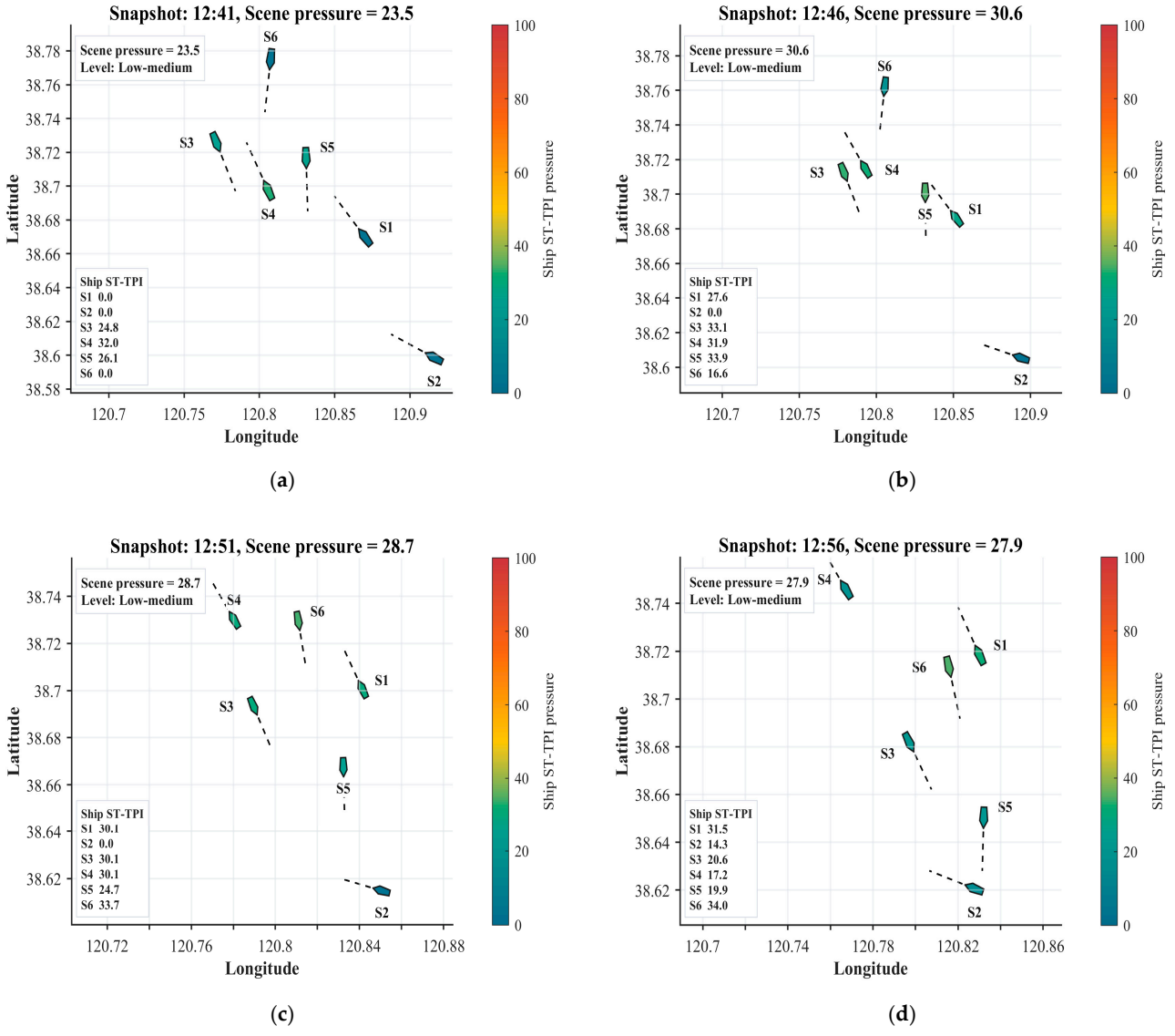


Figure 16. *Cont.*

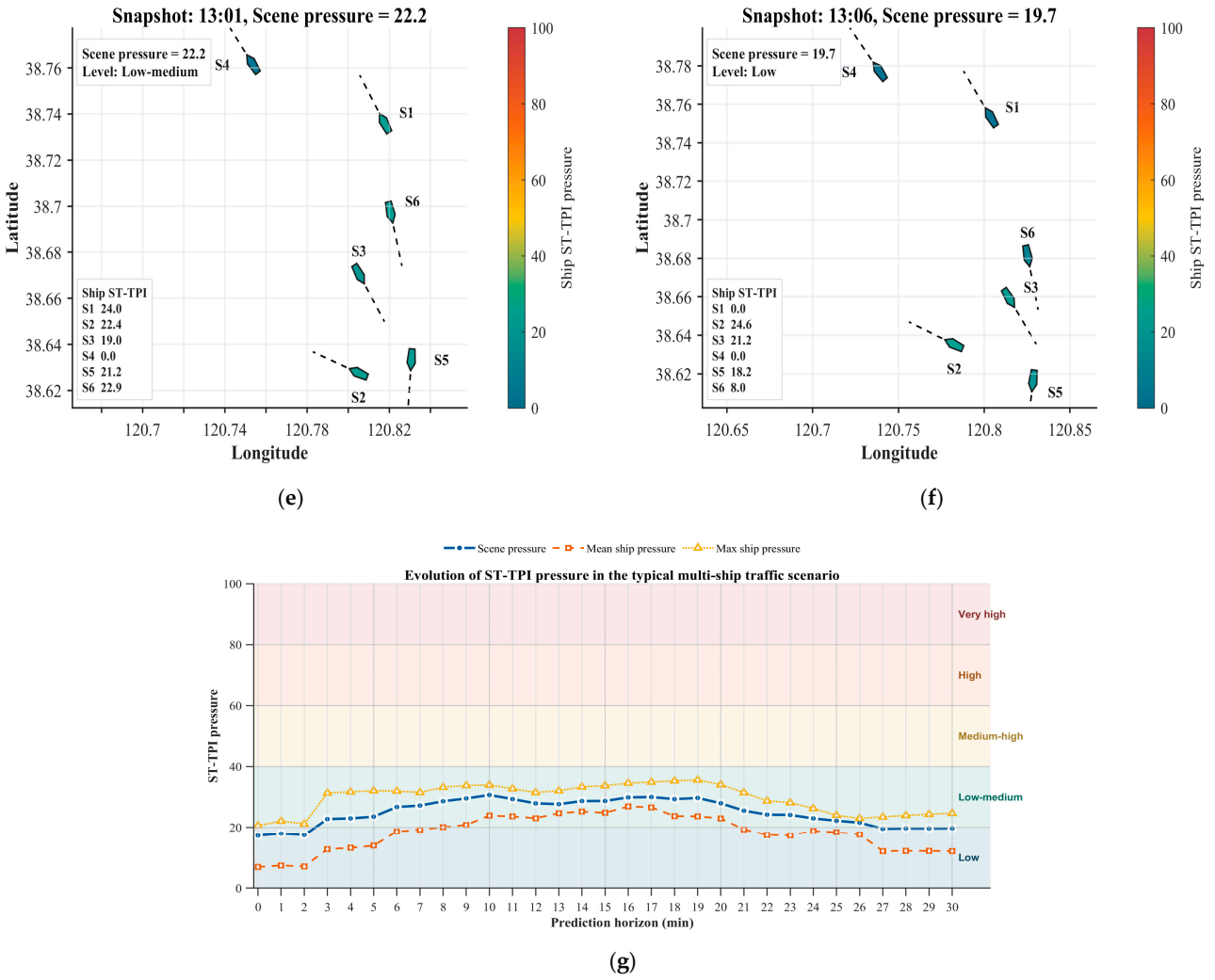


Figure 16. Predictive ST-TPI assessment results in the Laotieshan Channel real-waterway case. (**a**) A 5 min pressure snapshot; (**b**) 10 min pressure snapshot; (**c**) 15 min pressure snapshot; (**d**) 20 min pressure snapshot; (**e**) 25 min pressure snapshot; (**f**) 30 min pressure snapshot; (**g**) pressure-evolution curve.

3.4. Sensitivity Analysis of ST-TPI Weights, Scale Parameters, and Pressure-Level Thresholds

To directly evaluate the robustness of the ST-TPI model with respect to different weights, scale parameters, and pressure-level thresholds, a sensitivity analysis was conducted using the six traffic scenarios considered in this study. A total of 186 snapshots were evaluated, including the five representative multi-ship scenarios and the Laotieshan Channel real-waterway case. This analysis was designed to examine whether the continuous scene-pressure values, ship-pair pressure rankings, top-5 high-pressure vessel-pair identification, and pressure-level classification remained stable under moderate parameter perturbations. The sensitivity results are summarized in Table 14, and the mean absolute scene-pressure changes for different perturbation groups are shown in Figure 17.

Overall, the ST-TPI results remained stable under reasonable parameter perturbations. For the individual-ship component weights, ship-pair pressure weights, motion-disorder weights, and scene-pressure aggregation weights, the mean absolute changes in scene pressure were all below 0.5 on the 0–100 pressure scale. Meanwhile, the ship-pair pressure rankings remained highly consistent, with Spearman rank correlation coefficients close to 1.0. The top-5 high-pressure pair overlap ratios were also close to or equal to 100%,

indicating that the main pressure-contributing vessel pairs were not substantially affected by moderate weight perturbations.

Table 14. Sensitivity analysis of ST-TPI parameters, weights, and pressure-level thresholds.

Perturbation Group	Perturbed Parameters	Range	Mean $\lvert \Delta P_{scene} \rvert$	Max $\lvert \Delta P_{scene} \rvert$	Pair-Ranking ρ	Top-5 Overlap (%)	Scene-Level Change (%)
Individual-ship component weights	w_{den}, w_{spa}, w_{conf}, w_{mot}	±20%	0.267	1.516	1.000	100.00	0.27
Ship-pair pressure weights	$w_{pair,spa}$, $w_{pair,conf}$	±20%	0.069	1.520	1.000	99.95	0.00
Motion-disorder weights	w_{course}, w_{speed}	±20%	0.182	0.996	1.000	100.00	0.00
Scene aggregation weights	w_{mean}, w_{95}, w_{reg}, $w_{pair,max}$, w_{num}, w_{high}	±20%	0.394	1.684	1.000	100.00	0.40
Physical scale parameters	R_p, D_s, D_0, T_0, T_{max}, N_{ref}, C_0, V_{std}, N_0	±20%	0.455	12.805	0.989	99.07	1.14
Pressure-level thresholds	τ_1, τ_2, τ_3, τ_4	±10%, ±20%	0.009	1.515	1.000	100.00	12.90

Note: The results were calculated from 186 snapshots extracted from six traffic scenarios. ρ denotes the mean Spearman rank correlation coefficient of ship-pair pressure rankings before and after perturbation.

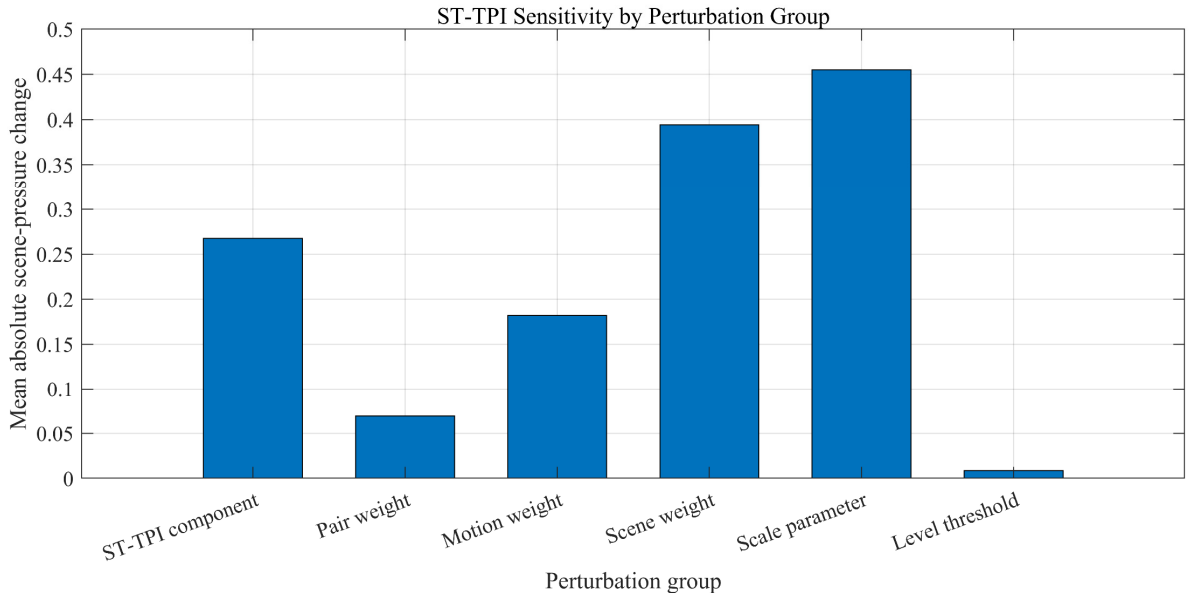


Figure 17. Mean absolute scene-pressure changes under different ST-TPI parameter perturbation groups.

Among all tested groups, the physical scale parameters showed the largest influence, with a mean absolute scene-pressure change of 0.455 and a maximum change of 12.805. This is reasonable because parameters such as the perception radius directly determine the set of neighboring vessels and potential encounter relations. Nevertheless, the mean pair-ranking correlation remained 0.989, and the top-5 high-pressure pair overlap ratio was 99.07%, suggesting that the main warning targets were still largely preserved.

The pressure-level thresholds had little influence on the continuous scene-pressure value and ship-pair ranking. The mean absolute scene-pressure change caused by threshold perturbation was only 0.009, and the top-5 high-pressure pair overlap remained 100%. However, the scene-level change rate reached 12.90%, indicating that threshold perturbation mainly affects categorical pressure labels rather than the continuous ST-TPI value or the ranking of high-pressure vessel pairs.

3.5. Prediction-Error Perturbation Analysis

Since the proposed LSTM–ST-TPI framework uses predicted vessel states as the input for subsequent pressure assessment, trajectory prediction errors may propagate into DCPA, TCPA, encounter relations, and pressure-source identification. To examine this effect, a prediction-error perturbation analysis was conducted. The original predicted multi-ship traffic snapshots were used as the baseline, and artificial position perturbations with magnitudes of 0 m, 25 m, 50 m, 100 m, and 150 m were added to the predicted vessel positions, where 0 m denotes the no-perturbation baseline. For each perturbation level, 50 Monte Carlo realizations were generated, and the pairwise kinematic relations and all hierarchical ST-TPI outputs were recalculated using the same parameter settings.

Figure 18 shows the stability of ST-TPI outputs under different prediction-position perturbation magnitudes. The mean absolute change in scene pressure increased gradually as the perturbation magnitude became larger. However, even under the 150 m perturbation level, the mean absolute scene-pressure change remained below 1.5 on the 0–100 ST-TPI scale. This indicates that prediction-position uncertainty can propagate into the continuous scene-pressure value, but the magnitude of the change remained limited within the tested perturbation range.

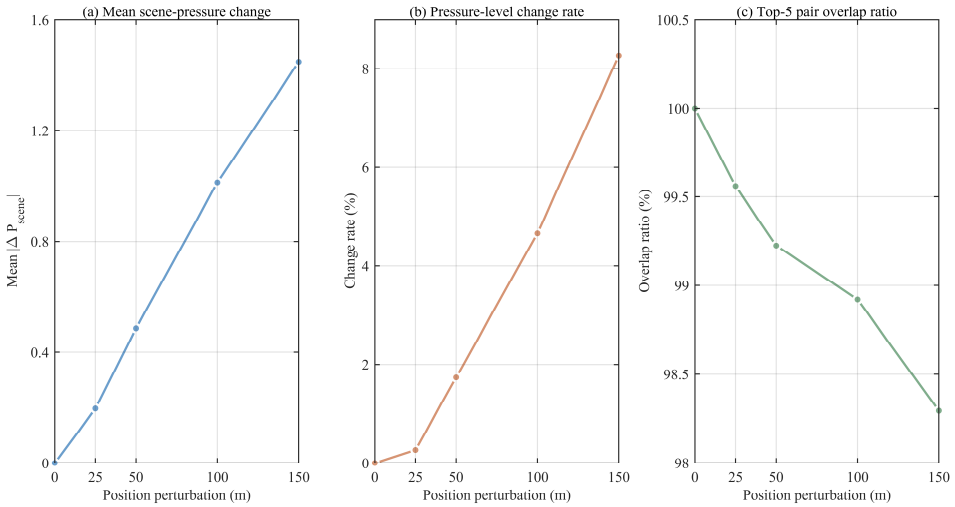


Figure 18. Stability of ST-TPI outputs under different prediction-position perturbation magnitudes. (**a**) Mean absolute change in scene pressure. (**b**) Pressure-level change rate. (**c**) Top-5 high-pressure pair overlap ratio.

Table 15 summarizes the perturbation results at different assessment levels. At the ship-pair level, the pair-pressure rankings changed only slightly, with Spearman correlation coefficients remaining above 0.98. The top-5 high-pressure pair overlap ratios were also higher than 98%, showing that the main high-pressure vessel pairs were largely unchanged. At the individual-ship level, the dominant vessel consistency stayed at approximately 80% or above. At the regional and scene levels, the mean absolute pressure changes increased with perturbation magnitude, but the values remained small on the 0–100 ST-TPI scale. The pressure-level change rate was below 10% in all perturbation cases, indicating that most categorical changes occurred only near pressure-level thresholds. These results indicate that position prediction errors can influence local encounter variables and pressure values, but they do not substantially change the main pressure-contributing pairs or the overall pressure-evolution interpretation in the tested cases.

Table 15. Stability metrics of ST-TPI outputs under prediction-position perturbations.

Assessment Level	Stability Metric	25 m	50 m	100 m	150 m
Ship-pair level	Pair-ranking Spearman ϱ	0.999	0.995	0.987	0.982
Ship-pair level	Top-5 pair overlap (%)	99.56	99.23	98.92	98.29
Individual-ship level	Dominant vessel consistency (%)	86.60	84.33	80.60	80.00
Regional level	Mean $\lvert\Delta P_regional\rvert$	0.162	0.418	0.877	1.269
Scene level	Mean $\lvert\Delta P_scene\rvert$	0.196	0.485	1.012	1.447
Scene level	Pressure-level change rate (%)	0.27	1.73	4.67	8.27

3.6. Consistency Analysis Between ST-TPI and Conventional Encounter-Risk Indicators

In this study, the conventional encounter-risk reference was constructed from DCPA and TCPA. Smaller DCPA values and shorter positive TCPA values indicate higher encounter urgency. Vessel pairs with negative TCPA were treated as non-approaching or post-encounter pairs and were assigned a lower encounter-risk contribution. The DCPA/TCPA-based CRI was then used as an external reference to examine whether high ST-TPI ship-pair pressure was consistent with conventional close-encounter risk.

Expert judgments, historical maritime incident records, and operational VTS logs were not available for the selected scenarios. Therefore, this study used conventional encounter-risk indicators, including DCPA, TCPA, and a DCPA/TCPA-based collision-risk index (CRI), as objective external references for practical validity checking. Although these indicators cannot fully replace expert or operational validation, they provide widely accepted quantitative references for spatial proximity and temporal encounter urgency. The consistency analysis between ST-TPI and these conventional indicators was therefore used to examine whether the proposed pressure index is aligned with established encounter-risk interpretation.

To further examine the practical validity of the proposed ST-TPI, a consistency analysis was conducted between ST-TPI and conventional encounter-risk indicators.

For each ship pair in the 186 traffic snapshots, DCPA, TCPA, and the DCPA/TCPA-based CRI were calculated using the same spatial and temporal scale parameters as those adopted in the ST-TPI model. In this way, the comparison was performed under consistent reference scales. The consistency was evaluated from both ship-pair and scene levels. At the ship-pair level, Spearman rank correlation coefficients were calculated between ST-TPI pair pressure and conventional risk scores. In addition, the overlap between the top-5 ship pairs identified by ST-TPI and those identified by CRI was calculated. At the scene level, the ST-TPI scene pressure was compared with the maximum CRI and the mean CRI of the top-5 risky ship pairs in each snapshot.

The overall consistency results are shown in Figure 19 and Table 16. To provide statistical support for the consistency results, two-sided significance tests were conducted for all Spearman rank-correlation results. The corresponding p-values and sample sizes are reported in Table 16. All reported Spearman correlations were statistically significant with $p < 0.001$, indicating that the observed consistency between ST-TPI and conventional encounter-risk indicators was unlikely to be caused by random ranking variation.

At the ship-pair level, ST-TPI pair pressure showed a moderate positive correlation with the DCPA score, with a Spearman coefficient of 0.413. When only encounter-relevant ship pairs with non-zero CRI were considered, the correlation between ST-TPI pair pressure and CRI increased to 0.498, and the correlation with the TCPA score reached 0.616. This indicates that, for ship pairs with actual encounter urgency, higher ST-TPI pressure generally corresponds to higher conventional encounter risk. The mean overlap between the top-5 ST-TPI ship pairs and the top-5 CRI ship pairs was 68.26%, suggesting that the proposed method and the conventional risk indicator identify largely consistent high-attention ship pairs.

At the scene level, the consistency became more evident. The Spearman correlation between ST-TPI scene pressure and the top-5 mean CRI was 0.610, while the correlation between ST-TPI scene pressure and the maximum CRI was 0.633. These results indicate that scenes with higher ST-TPI pressure usually contain more severe conventional encounter-risk relationships.

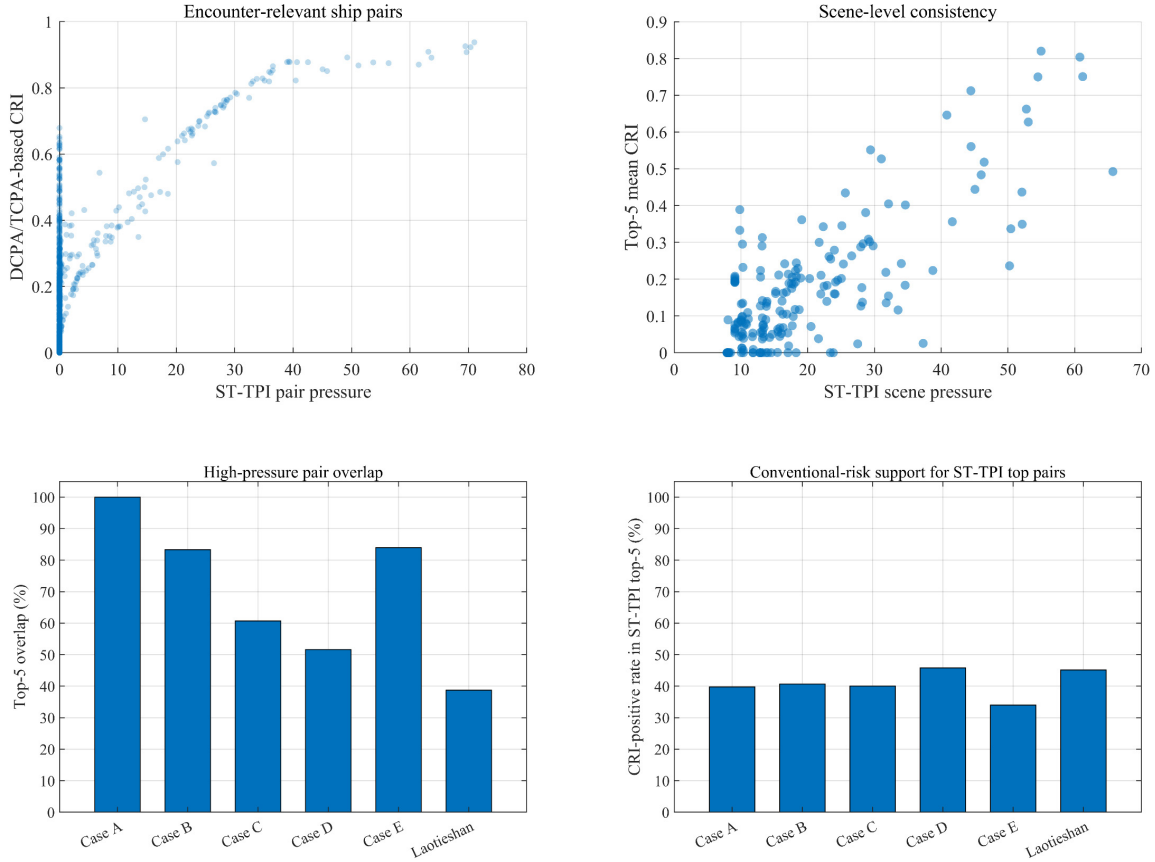


Figure 19. Consistency between ST-TPI and conventional encounter-risk indicators.

Table 16. Consistency metrics between ST-TPI and conventional encounter-risk indicators.

Scale	Reference Indicator	Metric	Value	*p*-Value	N
Ship-pair	DCPA score	Spearman ϱ (P_{pair}, DCPA score)	0.413	<0.001	2233
Ship-pair	CRI	Spearman ϱ (P_{pair}, CRI), CRI > 0	0.498	<0.001	823
Ship-pair	TCPA score	Spearman ϱ (P_{pair}, TCPA score), CRI > 0	0.616	<0.001	823
Ship-pair	Top-5 CRI pairs	Mean Top-5 overlap (%)	68.26	-	167
Scene	Top-5 mean CRI	Spearman ϱ (P_{scene}, Top-5 mean CRI)	0.610	<0.001	186
Scene	Maximum CRI	Spearman ϱ (P_{scene}, maximum CRI)	0.633	<0.001	186

In Table 16, CRI > 0 denotes encounter-relevant ship pairs with non-zero DCPA/TCPA-based collision-risk scores. The top-5 overlap was calculated only for snapshots with a non-zero and non-tied CRI ranking, and N denotes the number of ship pairs or snapshots used for each metric. For the Spearman rank-correlation results, two-sided significance tests were also conducted, and all reported Spearman correlations were statistically significant with $p < 0.001$. This indicates that the observed consistency between ST-TPI and conventional encounter-risk indicators is unlikely to be caused by random ranking variation.

To further illustrate the temporal consistency between ST-TPI and conventional encounter-risk indicators, the complex multi-ship interaction scenario was selected as

a representative case, as shown in Figure 20. The ST-TPI scene pressure and top-5 mean CRI exhibit similar increasing and decreasing trends. In the middle stage of the scenario, both indicators increase rapidly and reach high values, indicating the accumulation of multi-ship traffic pressure and conventional encounter risk. In the later stage, both indicators decrease as the encounter relationships are released. This result suggests that ST-TPI can capture not only static high-pressure states, but also the temporal accumulation and release process of encounter-related traffic pressure.

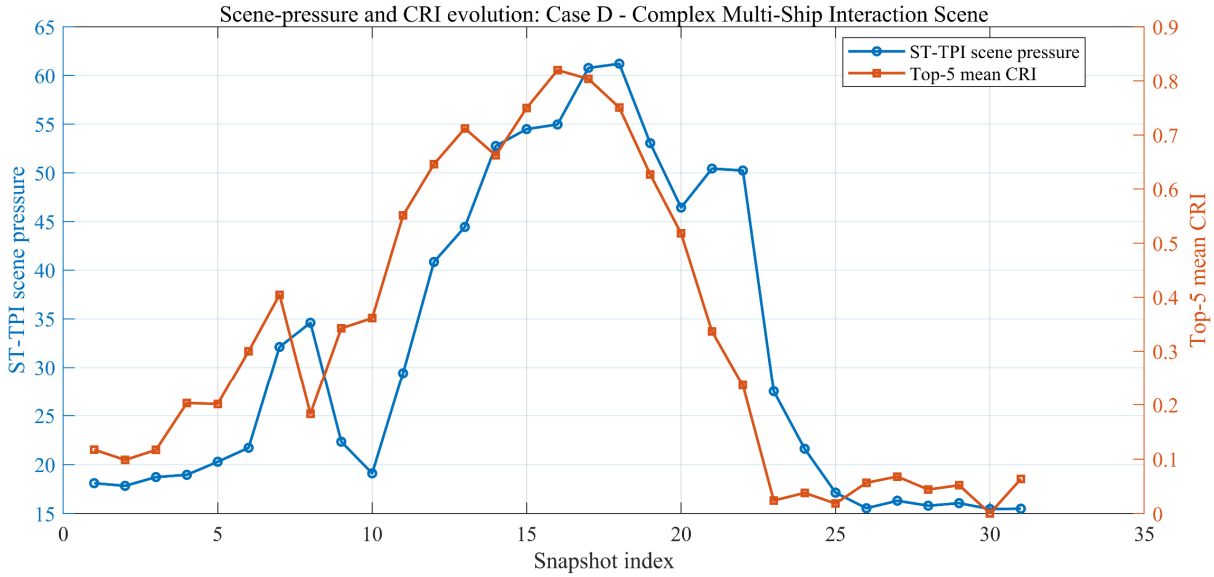


Figure 20. Time-series comparison between ST-TPI scene pressure and top-5 mean CRI in the complex multi-ship interaction scenario.

It should be noted that ST-TPI is not designed to be a direct substitute for conventional collision-risk indices. DCPA, TCPA, and CRI mainly describe local pairwise encounter danger, whereas ST-TPI further incorporates vessel density, spatial compression, multi-ship aggregation, and motion disorder. Therefore, moderate differences between ST-TPI and CRI are expected. The above results suggest that ST-TPI is reasonably consistent with conventional encounter-risk indicators, while providing additional information on multi-ship traffic pressure and supervisory workload.

4. Discussion

The results of this study should be understood in the context of the relation between future motion prediction and traffic-pressure assessment. In the proposed system, the trajectory prediction is not used as a separate final output. Instead, it provides the motion-state basis for reconstructing future multi-ship traffic snapshots. The subsequent ST-TPI calculation translates these predicted snapshots into pressure information relevant to maritime supervision, including pressure levels, pressure variation, peak-pressure moments, and local pressure-contributing vessels or vessel pairs.

Therefore, the LSTM model in this work serves as a support module for future traffic-state reconstruction. The goal is to estimate realistic future vessel states, such as position, speed, and direction, for creating synchronized multi-ship snapshots over the prediction horizon. Local prediction errors may occur when vessels turn, accelerate, decelerate, or maneuver inside a confined area. However, the results in Section 3.1 show that the prediction errors are reasonably consistent within the 30 min horizon. The fundamental requirement for the future ST-TPI assessment is not the exact point-by-point reproduction of every vessel route, but the preservation of the basic relative spatial structure and encounter

relations among vessels. These reconstructed relationships form the basis for computing inter-ship distance, DCPA, TCPA, local compression, and traffic-pressure indicators.

The five typical scenarios further show that traffic pressure cannot be explained by vessel number alone. In the low-density case, the pressure remained low because the vessels were spatially separated and weakly interacting. In the dense but ordered case, local compression raised the pressure temporarily, but the pressure was released when the vessels moved out of the compact formation. In the crossing encounter case, pressure growth appeared later, indicating that crossing-related pressure may become evident only after the relative geometry has developed for a period of time. In the complex multi-ship interaction case, an initially elevated pressure level gradually decreased as the local structure loosened. In the pressure-rising case, the scene evolved from a low-pressure state into the High level within the prediction horizon. These results indicate that the proposed framework is able to distinguish not only different pressure magnitudes but also different pressure-evolution mechanisms, such as persistence, temporary compression, delayed growth, release, and escalation.

The real-waterway case in the western precautionary area of the Laotieshan Channel provides a further check under practical AIS conditions. Unlike the pressure-rising typical scenario, this case did not develop into a High-level pressure state. Its value lies in showing that the framework can still provide meaningful information when the traffic pressure remains within the Low to Low-medium range. The case captured a moderate pressure fluctuation, a peak at the early prediction stage, and a subsequent release process. It also showed that the local pressure source may shift with the change in vessel relative positions. This is important for real supervision, because not every useful warning situation appears as an extreme high-pressure event. In many practical waterways, identifying moderate pressure variation, pressure release, and the migration of local attention targets is also valuable for continuous monitoring.

These findings also clarify the difference between traffic pressure and conventional collision risk. Collision-risk assessment usually focuses on whether a vessel pair may enter a dangerous encounter state. Traffic pressure, as used in this study, describes a broader supervisory load caused by vessel density, spatial compression, encounter urgency, and inconsistency of motion states. A traffic scene may therefore produce noticeable pressure even when no individual-ship pair has reached an extreme collision-risk condition. Conversely, a scene with a seemingly complex initial structure may release quickly if vessel relations become less compact. This distinction is useful for VTS operation, because supervisors need not only to identify dangerous ship pairs, but also to judge whether the whole scene is becoming more difficult to monitor and manage.

Interpretability is another significant property of the proposed system. The ST-TPI model does not provide only a single scene-level pressure value. It also outputs ship-level pressure, ship-pair pressure, regional pressure, pressure-level transitions, dominant vessels, and dominant vessel pairs. These outputs allow pressure changes to be traced from the overall scene back to local contributing objects. For maritime supervision, this means that the scene is not considered uniformly risky, but rather one can focus on those vessels or pairs of vessels that contribute the most to the pressure.

The sensitivity analysis in Section 3.4 further shows that the ST-TPI results are generally robust to moderate perturbations of weights and pressure-level thresholds. The physical scale parameters, especially those determining the neighboring-vessel set, have a relatively larger influence on the pressure magnitude. This suggests that such parameters should be adjusted carefully when the framework is transferred to waterways with substantially different traffic density, navigational width, or supervisory requirements.

The prediction-error perturbation analysis further clarifies how trajectory uncertainty may propagate into pressure assessment. Position perturbations can affect inter-vessel distance, DCPA, TCPA, encounter relations, and local pressure values. However, the tested perturbation results show that the overall scene-pressure change remained limited, the pressure-level change rate stayed below 10%, and the top-5 high-pressure pair overlap ratio remained above 98%. This suggests that the main pressure-evolution trend and dominant high-pressure vessel-pair identification were relatively stable under the tested prediction-position uncertainty. Nevertheless, the present analysis is still a deterministic perturbation test rather than a full probabilistic uncertainty-propagation model. Future work should further incorporate uncertainty-aware trajectory prediction and probabilistic pressure assessment.

The proposed prediction-driven pressure-assessment framework may also be connected with future digital supervisory-support systems. In maritime engineering, co-simulation and digital-twin concepts have been regarded as important technologies for integrating ship models, operational environments, and decision-support functions [39]. From this perspective, the future development of the LSTM–ST-TPI framework could be further linked with digital-twin-oriented VTS platforms, where live AIS streams, short-term traffic prediction, pressure assessment, and warning visualization are updated in a rolling manner. Such integration would help extend the present offline-validated framework toward proactive monitoring and early-warning support in practical supervisory waters.

It is also worth mentioning that there are some limitations. First, the LSTM model adopted in this work mainly depends on the past AIS motion states and does not explicitly take into account the navigation intention, planned routes, hydrometeorological circumstances, traffic laws and ship-handling constraints. Thus, forecast uncertainty can be higher when vessels do significant maneuvers or make decisions that are not represented in their recent motion history. In addition, the current implementation approximates the predicted heading by the predicted COG. This treatment is reasonable for steady underway cargo-vessel motion, but may be less accurate during low-speed navigation, sharp turning, berthing or unberthing, or under strong drift conditions. Such uncertainty may affect heading-related encounter features and should be further improved by incorporating direct heading prediction or maneuvering-aware motion models. LSTM was utilized to construct a robust and reproducible framework for pressure prediction in this study. In future work, we can incorporate more advanced forecasting models, such as attention-based sequence models, Transformer-based models, graph-based interaction-aware models, or probabilistic trajectory prediction approaches into the same framework to enhance the prediction of complex maneuvering and multi-ship interaction behaviors. Second, the ST-TPI weights and pressure-level thresholds offer an interpretable pressure scale for this study, but the transferability to other waterways still requires further calibration. Third, although a prediction-error perturbation analysis was conducted to examine the stability of ST-TPI outputs under position uncertainty, the current approach still does not provide a full probabilistic uncertainty-propagation model from trajectory prediction to pressure evaluation. Future work should therefore include more accurate and interaction-aware motion prediction, uncertainty-aware pressure assessment, and broader real-waterway validation in port approaches, narrow channels, precautionary regions, and crossing waterways.

Overall, the proposed LSTM–ST-TPI framework provides a practical way to convert future multi-ship motion states into interpretable traffic-pressure information. The experimental results show that the framework can describe pressure accumulation, pressure release, delayed pressure growth, and High-level pressure formation in typical scenarios, while also capturing moderate pressure fluctuation in a real supervisory waterway. This

supports a shift from passive risk observation to predictive traffic-pressure monitoring and provides quantitative information for proactive maritime traffic supervision.

5. Conclusions

This study proposed a predictive multi-ship traffic-pressure assessment framework for maritime supervision by integrating LSTM-based short-term vessel motion prediction with the Spatio-Temporal Encounter Traffic Pressure Index (ST-TPI). The framework first reconstructs future multi-ship traffic snapshots from AIS-based motion prediction and then evaluates traffic pressure at ship-pair, individual-ship, regional, and overall scene levels. In this way, the output of trajectory prediction is further converted into interpretable pressure information rather than being limited to future position estimation.

We used the LSTM-based motion prediction model as the foundation for future traffic-state reconstruction. The prediction results demonstrate that the model maintained stable short-term forecasting performance under the observation-updated rolling evaluation setting. Local prediction errors may still occur during turning, speed-changing, or maneuvering processes. However, the predicted trajectories kept the primary motion directions and geometric relations of the multi-ship scenario. This supports their use in future multi-ship snapshot generation and subsequent ST-TPI-based pressure assessment.

The predictive ST-TPI results in five typical scenarios demonstrated that the proposed framework can distinguish different pressure-evolution patterns. The method maintained low pressure in sparse traffic, captured temporary pressure accumulation and release in dense but ordered traffic, identified delayed pressure growth in crossing encounters, reflected pressure release in complex multi-ship interaction, and detected a transition from low pressure to High-level pressure in the pressure-rising case. These results indicate that the framework can describe not only pressure magnitude, but also the way in which traffic pressure forms, persists, transfers, or dissipates.

The real-waterway case in the western precautionary area of the Laotieshan Channel further examined the applicability of the framework under practical AIS conditions. Although this case did not reach a High-level pressure state, it showed a clear Low and Low-medium pressure fluctuation, a local peak, and a subsequent release process. The result indicates that the proposed method is not limited to extreme high-pressure events; it can also support the interpretation of moderate pressure variation and local pressure-source transfer in real supervisory waterways. The sensitivity analysis, prediction-error perturbation analysis, and consistency comparison with conventional encounter-risk indicators further showed that the main pressure-evolution trends, high-pressure vessel-pair identification, and scene-level pressure interpretation were relatively stable under the tested conditions.

In summary, the proposed method provides a quantitative and interpretable tool for proactive supervision of marine traffic. Future work will include uncertainty-aware pressure assessment and validation using more real-world supervisory waterways, including precautionary zones, port approaches, restricted channels, and crossing waterways.

There are still many aspects to be further studied. The existing LSTM model mainly depends on the past AIS motion states and does not explicitly consider the navigation purpose, environmental conditions, and COLREGs-based maneuvering behavior. In this work, it obtains reliable short-term forecasts, but future research could incorporate more advanced trajectory prediction models such as attention-based models, Transformer-based architectures, graph neural networks, or probabilistic forecasting methods for a better representation of complex maneuvers and multi-ship interactions. Furthermore, the weights of ST-TPI and pressure-level thresholds should be further adjusted by using more traffic data from different waterways.

Author Contributions: Conceptualization, R.Z. and Q.L.; methodology, R.Z. and Q.L.; software, R.Z. and Q.L.; validation, R.Z., Q.L. and B.Z.; formal analysis, R.Z., Q.L. and B.Z.; investigation, R.Z., Q.L. and B.Z.; resources, R.Z., Q.L. and B.Z.; data curation, R.Z., Q.L. and B.Z.; writing—original draft preparation, R.Z., Q.L. and B.Z.; writing—review and editing, R.Z., Q.L. and B.Z.; visualization, R.Z. and Q.L.; supervision, Q.L.; project administration, Q.L. All authors have read and agreed to the published version of the manuscript.

Funding: This research received no external funding.

Institutional Review Board Statement: Not applicable.

Informed Consent Statement: Not applicable.

Data Availability Statement: The open-source AIS trajectory data used for LSTM model training, validation, and testing are available from the Maritime-Monitoring repository at https://github.com/eyesofworld/Maritime-Monitoring (accessed on 28 June 2026). The Laotieshan Channel case data and processed datasets generated in this study are available from the corresponding author upon reasonable request.

Conflicts of Interest: The authors declare no conflicts of interest.

Appendix A. ST-TPI Parameter Settings

The main parameter settings of the ST-TPI model are listed in Table A1.

Table A1. Main parameter settings of the ST-TPI model.

Symbol	Meaning	Value	Unit	Basis/Justification
C_{max}	Upper bound of pressure index	100	—	Used to normalize ship-pair pressure, individual-ship pressure, regional pressure, and scene pressure into an interpretable 0–100 scale. This scale is convenient for pressure-level classification and visualization.
R_p	Perception radius	3.0	n mile	Used to define the local neighboring-vessel set considered in ST-TPI calculation. This radius reflects the local traffic-supervision range in which nearby vessels may contribute to spatial compression, encounter urgency, and VTS monitoring workload.
D_s	Spatial safety scale	0.5	n mile	Used as the exponential decay scale for spatial proximity pressure. Smaller inter-vessel distances produce stronger spatial-compression pressure, and this parameter controls how quickly the spatial pressure decreases with distance.
D_0	DCPA decay scale	0.5	n mile	Used as the DCPA decay scale in the encounter-conflict component. A smaller DCPA indicates stronger close-encounter pressure. The value is also consistent with the near-miss and close-encounter interpretation used in conventional DCPA-based risk analysis.
T_0	TCPA decay scale	10	min	Used as the TCPA decay scale to represent short-term encounter urgency. A shorter positive TCPA indicates that a potential closest-approach situation is approaching soon and should therefore contribute more strongly to traffic pressure.

Table A1. *Cont.*

Symbol	Meaning	Value	Unit	Basis/Justification
T_{max}	Maximum time window for approaching encounters	30	min	Used as the maximum short-term look-ahead window for identifying approaching encounter relationships. It is consistent with the 30 min traffic-pressure trend assessment horizon used in this study. Longer-horizon results are interpreted mainly as trend-supporting information rather than deterministic trajectory forecasts.
N_{ref}	Reference effective neighbor number	6	—	Used to normalize the local density-pressure component. It represents a reference level of neighboring-vessel load within the perception radius and allows the density contribution to be mapped into a bounded pressure scale.
C_0	Reference closing speed	5	kn	Used to normalize the closing-speed factor in the encounter-conflict component. A larger closing speed indicates faster spatial compression between vessels and therefore contributes more strongly to encounter pressure.
V_{std}	Speed-disorder normalization scale	3	kn	Used to normalize the speed-disorder component. It represents a reference scale for local SOG variation among neighboring vessels and helps quantify motion inconsistency in the local traffic scene.
T_{high}	High-pressure threshold for ships and pairs	60	—	Used to identify high-pressure vessels and high-pressure vessel pairs. This threshold corresponds to the boundary between Medium-high and High pressure on the 0–100 ST-TPI scale.
$w_{pair,spa}$	Weight of pairwise spatial pressure	0.35	—	Used to represent the contribution of current spatial proximity to ship-pair pressure. It captures the pressure caused by short inter-vessel distance.
$w_{pair,conf}$	Weight of pairwise encounter-conflict pressure	0.65	—	Assigned a larger value because DCPA, TCPA, heading relation, and closing speed more directly reflect encounter urgency and potential conflict between vessel pairs.
w_{den}	Weight of local density pressure	0.25	—	Used to represent the contribution of neighboring-vessel load and local aggregation to individual-ship pressure.
w_{spa}	Weight of spatial proximity pressure	0.20	—	Used to represent the contribution of local spatial compression around an individual vessel.
w_{conf}	Weight of encounter-conflict pressure	0.40	—	Assigned the largest weight among the individual-ship components because encounter urgency, reflected by DCPA/TCPA-related relations, is directly associated with supervision priority and collision-avoidance attention.
w_{mot}	Weight of motion-disorder pressure	0.15	—	Used to represent the contribution of local course and speed inconsistency to individual-ship pressure. It supplements the density, proximity, and encounter-conflict components.

Table A1. *Cont.*

Symbol	Meaning	Value	Unit	Basis/Justification
w_{course}	Weight of course-disorder pressure	0.70	—	Assigned a larger value in the motion-disorder component because course differences are more directly related to crossing, converging, and diverging traffic structures.
w_{speed}	Weight of speed-disorder pressure	0.30	—	Used to supplement the course-disorder component by representing local SOG variation among neighboring vessels.
$w_{R,\text{mean}}$	Weight of mean ship pressure in regional ST-TPI	0.60	—	Used to reflect the overall average pressure level of vessels in the region.
$w_{R,95}$	Weight of P95 ship pressure in regional ST-TPI	0.40	—	Used to retain the influence of high-pressure vessels that may be smoothed by the mean pressure alone.
w_{mean}	Weight of mean ship pressure in scene pressure	0.35	—	Used to represent the general traffic-pressure level of the whole scene.
w_{95}	Weight of P95 ship pressure in scene pressure	0.20	—	Used to retain the influence of high-pressure vessels at the upper tail of the ship-pressure distribution.
w_{reg}	Weight of regional ST-TPI in scene pressure	0.20	—	Used to include the regional-level pressure state in the overall scene-pressure aggregation.
$w_{\text{pair,max}}$	Weight of maximum pair pressure in scene pressure	0.20	—	Used to emphasize the contribution of the most critical ship-pair interaction to the overall scene pressure.
w_{num}	Weight of ship-number pressure in scene pressure	0.10	—	Used to reflect the traffic-load contribution caused by the number of vessels in the scene.
w_{high}	Weight of high-pressure pair ratio in scene pressure	0.05	—	Used to represent the proportion of high-pressure vessel pairs among all candidate pairs. It supplements the maximum-pair-pressure term by considering whether high pair pressure is isolated or widespread.
N_0	Reference vessel number for ship-number pressure	6	—	Used to normalize the ship-number pressure term in scene-pressure aggregation. It provides a reference scale for evaluating the vessel-number load of a multi-ship scene.
$\tau_1, \tau_2, \tau_3, \tau_4$	Scene pressure level thresholds	20, 40, 60, 80	—	Used to classify the continuous scene-pressure value into five interpretable levels: Low, Low-medium, Medium-high, High, and Very high. These thresholds provide an operationally readable pressure scale for traffic monitoring and visualization. Their robustness was further examined through threshold perturbation in the sensitivity analysis.

Note: The scene-pressure aggregation weights are normalized in the implementation before calculating the final scene-pressure value. The above parameters were selected according to the requirements of local-waterway traffic supervision, DCPA/TCPA-based encounter interpretation, AIS-based short-term assessment scale, and the interpretability of the 0–100 pressure scale. Since traffic characteristics may differ across waterways, the robustness of these parameters was further examined through the sensitivity analysis of parameter perturbations, weight changes, and pressure-level thresholds.

References

1. International Maritime Organization. *Resolution A.1158(32): Guidelines for Vessel Traffic Services*; IMO: London, UK, 2021.
2. Zhang, L.; Ge, J.; Goerlandt, F.; Du, L.; Chen, T.; Gu, T.; Gan, L.; Li, X. A Method for Enhancing the Traffic Situation Awareness of Vessel Traffic Service Operators by Identifying High Risk Ships in Complex Navigation Conditions. *J. Mar. Sci. Eng.* **2025**, *13*, 379. [CrossRef]
3. Szlapczynski, R.; Szlapczynska, J. A Ship Domain-Based Model of Collision Risk for Near-Miss Detection and Collision Alert Systems. *Reliab. Eng. Syst. Saf.* **2021**, *214*, 107766. [CrossRef]
4. Ha, J.; Roh, M.-I.; Lee, H.-W. Quantitative Calculation Method of the Collision Risk for Collision Avoidance in Ship Navigation Using the CPA and Ship Domain. *J. Comput. Des. Eng.* **2021**, *8*, 894–909. [CrossRef]
5. Huang, Y.; van Gelder, P.H.A.J.M. Measuring Ship Collision Risk in a Dense Traffic Environment. *TransNav Int. J. Mar. Navig. Saf. Sea Transp.* **2019**, *13*, 737–744. [CrossRef]
6. Liu, Z.; Zhang, B.; Zhang, M.; Wang, H.; Fu, X. A Quantitative Method for the Analysis of Ship Collision Risk Using AIS Data. *Ocean Eng.* **2023**, *272*, 113906. [CrossRef]
7. Sang, L.Z.; Yan, X.P.; Wall, A.; Wang, J.; Mao, Z. CPA Calculation Method Based on AIS Position Prediction. *J. Navig.* **2016**, *69*, 1409–1426. [CrossRef]
8. Zhang, W.; Goerlandt, F.; Montewka, J.; Kujala, P. A Method for Detecting Possible near Miss Ship Collisions from AIS Data. *Ocean Eng.* **2015**, *107*, 60–69. [CrossRef]
9. Yu, H.; Meng, Q.; Fang, Z.; Liu, J.; Xu, L. A Review of Ship Collision Risk Assessment, Hotspot Detection and Path Planning for Maritime Traffic Control in Restricted Waters. *J. Navig.* **2022**, *75*, 1337–1363. [CrossRef]
10. Shi, Z.; Zhen, R.; Liu, J. Fuzzy Logic-Based Modeling Method for Regional Multi-Ship Collision Risk Assessment Considering Impacts of Ship Crossing Angle and Navigational Environment. *Ocean Eng.* **2022**, *259*, 111847. [CrossRef]
11. Liu, Z.; Zhou, D.; Zheng, Z.; Wu, Z.; Guedes Soares, C. A Multi-Dimensional Formulation for Assessing Regional Collision Risk Based on AIS Data. *Appl. Ocean Res.* **2025**, *161*, 104612. [CrossRef]
12. Zhang, W.; Feng, X.; Qi, Y.; Shu, F.; Zhang, Y.; Wang, Y. Towards a Model of Regional Vessel Near-Miss Collision Risk Assessment for Open Waters Based on AIS Data. *J. Navig.* **2019**, *72*, 1449–1468. [CrossRef]
13. Geng, X.; Huang, L.; Wen, Y.; Zhou, C. Modelling of the Marine Traffic Situation Complexity. *MATEC Web Conf.* **2016**, *68*, 15002. [CrossRef]
14. Sui, Z.; Wen, Y.; Huang, Y.; Zhou, C.; Xiao, C.; Chen, H. Empirical Analysis of Complex Network for Marine Traffic Situation. *Ocean Eng.* **2020**, *214*, 107848. [CrossRef]
15. Liu, Z.; Wu, Z.; Zheng, Z.; Yu, X. A Molecular Dynamics Approach to Identify the Marine Traffic Complexity in a Waterway. *J. Mar. Sci. Eng.* **2022**, *10*, 1678. [CrossRef]
16. Ji, Z.; Zhang, Y.; Wang, F.; Yang, J.; Zou, Y. Identification of Multi-Ship Maritime Traffic Situation Based on Ship Traffic Complexity Measurement Model. *Ocean Eng.* **2024**, *301*, 117442. [CrossRef]
17. Zhang, F.; Liu, Y.; Du, L.; Goerlandt, F.; Sui, Z.; Wen, Y. A Rule-Based Maritime Traffic Situation Complex Network Approach for Enhancing Situation Awareness of Vessel Traffic Service Operators. *Ocean Eng.* **2023**, *284*, 115203. [CrossRef]
18. Liu, Z.; Yu, P. A Novel Time-Frame Regional Collision Risk Model Based on Dynamic Time Warping. *J. Mar. Sci. Eng.* **2025**, *13*, 263. [CrossRef]
19. Wang, C.; Li, G.; Han, P.; Osen, O.; Zhang, H. Impacts of COVID-19 on Ship Behaviours in Port Area: An AIS Data-Based Pattern Recognition Approach. *IEEE Trans. Intell. Transp. Syst.* **2022**, *23*, 25127–25138. [CrossRef]
20. Luo, J.; Wang, G.; Li, G.; Pesce, G. Transport Infrastructure Connectivity and Conflict Resolution: A Machine Learning Analysis. *Neural Comput. Appl.* **2022**, *34*, 6585–6601. [CrossRef]
21. Chen, J.; Pan, S.; Peng, W.; Xu, W. Bilinear Spatiotemporal Fusion Network: An Efficient Approach for Traffic Flow Prediction. *Neural Netw.* **2025**, *187*, 107382. [CrossRef] [PubMed]
22. Li, H.; Jiao, H.; Yang, Z. AIS Data-Driven Ship Trajectory Prediction Modelling and Analysis Based on Machine Learning and Deep Learning Methods. *Transp. Res. Part E Logist. Transp. Rev.* **2023**, *175*, 103152. [CrossRef]
23. Yang, C.-H.; Lin, G.-C.; Wu, C.-H.; Liu, Y.-H.; Wang, Y.-C.; Chen, K.-C. Deep Learning for Vessel Trajectory Prediction Using Clustered AIS Data. *Mathematics* **2022**, *10*, 2936. [CrossRef]
24. Yin, J.; Yu, Z.; Wu, H. Ship Trajectory Prediction Based on LSTM Model with Multi-Scale Convolution and Attention Mechanism. *Ocean Eng.* **2025**, *338*, 122055. [CrossRef]
25. Liu, R.W.; Liang, M.; Nie, J.; Lim, W.Y.B.; Zhang, Y.; Guizani, M. Deep Learning-Powered Vessel Trajectory Prediction for Improving Smart Traffic Services in Maritime Internet of Things. *IEEE Trans. Netw. Sci. Eng.* **2022**, *9*, 3080–3094. [CrossRef]
26. Shin, Y.; Kim, N.; Lee, H.; In, S.Y.; Hansen, M.; Yoon, Y. Deep Learning Framework for Vessel Trajectory Prediction Using Auxiliary Tasks and Convolutional Networks. *Eng. Appl. Artif. Intell.* **2024**, *132*, 107936. [CrossRef]
27. Wang, J.; Liu, S.; Zhang, Y. A Graph Learning-Driven Method for Multi-Ship Collision Risk Prediction in Complex Waterways. *J. Mar. Sci. Eng.* **2026**, *14*, 658. [CrossRef]

28. Eyes of World. Maritime-Monitoring: AIS-Based Vessel Trajectory Dataset and Monitoring Repository. GitHub Repository. Available online: https://github.com/eyesofworld/Maritime-Monitoring (accessed on 1 April 2026).
29. Emmens, T.; Amrit, C.; Abdi, A.; Ghosh, M. The Promises and Perils of Automatic Identification System Data. *Expert Syst. Appl.* **2021**, *178*, 114975. [CrossRef]
30. Zhao, L.; Shi, G.; Yang, J. Ship Trajectories Pre-Processing Based on AIS Data. *J. Navig.* **2018**, *71*, 1210–1230. [CrossRef]
31. Iphar, C.; Napoli, A.; Ray, C. An Expert-Based Method for the Risk Assessment of Anomalous Maritime Transportation Data. *Appl. Ocean Res.* **2020**, *104*, 102337. [CrossRef]
32. Guo, S.; Mou, J.; Chen, L.; Chen, P. Improved Kinematic Interpolation for AIS Trajectory Reconstruction. *Ocean Eng.* **2021**, *234*, 109256. [CrossRef]
33. Liang, M.; Su, J.; Liu, R.W.; Lam, J.S.L. AISClean: AIS Data-Driven Vessel Trajectory Reconstruction under Uncertain Conditions. *Ocean Eng.* **2024**, *306*, 117987. [CrossRef]
34. Tang, H.; Yin, Y.; Shen, H. A Model for Vessel Trajectory Prediction Based on Long Short-Term Memory Neural Network. *J. Mar. Eng. Technol.* **2022**, *21*, 136–145. [CrossRef]
35. Sørensen, K.A.; Heiselberg, P.; Heiselberg, H. Probabilistic Maritime Trajectory Prediction in Complex Scenarios Using Deep Learning. *Sensors* **2022**, *22*, 2058. [CrossRef] [PubMed]
36. Zhu, J.; Gao, M.; Zhang, A.; Hu, Y.; Zeng, X. Multi-Ship Encounter Situation Identification and Analysis Based on AIS Data and Graph Complex Network Theory. *J. Mar. Sci. Eng.* **2022**, *10*, 1536. [CrossRef]
37. Gao, D.; Zhu, Y.; Yan, K.; Soares, C.G. Deep Learning–Based Framework for Regional Risk Assessment in a Multi–Ship Encounter Situation Based on the Transformer Network. *Reliab. Eng. Syst. Saf.* **2024**, *241*, 109636. [CrossRef]
38. Lee, E.-J.; Kim, H.-S.; Yu, Y. A Complexity-Aware Course–Speed Model Integrating Traffic Complexity Index for Nonlinear Crossing Waters. *J. Mar. Sci. Eng.* **2025**, *13*, 2086. [CrossRef]
39. Hatledal, L.I.; Skulstad, R.; Li, G.; Styve, A.; Zhang, H. Co-Simulation as a Fundamental Technology for Twin Ships. *Model. Identif. Control* **2020**, *41*, 297–311. [CrossRef]

Disclaimer/Publisher's Note: The statements, opinions and data contained in all publications are solely those of the individual author(s) and contributor(s) and not of MDPI and/or the editor(s). MDPI and/or the editor(s) disclaim responsibility for any injury to people or property resulting from any ideas, methods, instructions or products referred to in the content.